# DEVELOPMENT OF A CLOSELY COUPLED APPROACH FOR SOLUTION OF STATIC AND DYNAMIC AEROELASTIC PROBLEMS

A THESIS SUBMITTED TO
THE GRADUATE SCHOOL OF NATURAL AND APPLIED SCIENCES
OF
MIDDLE EAST TECHNICAL UNIVERSITY

BY
ERKUT BAŞKUT

IN PARTIAL FULFILLMENT OF THE REQUIREMENTS
FOR
THE DEGREE OF MASTER OF SCIENCE
IN
AEROSPACE ENGINEERING

JUNE 2010

Approval of the thesis :

**DEVELOPMENT OF A CLOSELY COUPLED APPROACH FOR SOLUTION OF STATIC AND DYNAMIC AEROELASTIC PROBLEMS**

submitted by **ERKUT BAŞKUT** in partial fulfillment of the requirements for the degree of **Master of Science in Aerospace Engineering Department, Middle East Technical University** by,

Prof. Dr. Canan Özgen _____
Dean, Graduate School of **Natural and Applied Sciences**

Prof. Dr. Ozan Tekinalp _____
Head of Department, **Aerospace Engineering**

Asst. Prof. Dr. Güçlü Seber _____
Supervisor, **Aerospace Engineering Dept., METU**

Assoc. Prof. Dr. Altan Kayran _____
Co-Supervisor, **Aerospace Engineering Dept., METU**

**Examining Committee Members:**

Assoc. Prof. Dr. Sinan Eyi _____
Aerospace Engineering Dept., METU

Asst. Prof. Dr. Güçlü Seber _____
Aerospace Engineering Dept., METU

Assoc. Prof. Dr. Altan Kayran _____
Aerospace Engineering Dept., METU

Asst. Prof. Dr. Demirkan Çöker _____
Aerospace Engineering Dept., METU

Ali Akgül _____
Head of Aerodynamic Dept., ROKETSAN

**Date:** 25.06.2010

**I hereby declare that all information in this document has been obtained and presented in accordance with academic rules and ethical conduct. I also declare that, as required by these rules and conduct, I have fully cited and referenced all material and results that are not original to this work.**

Name, Last name : Erkut Başkut

Signature :

# ABSTRACT

DEVELOPMENT OF A CLOSELY COUPLED APPROACH FOR SOLUTION OF STATIC AND DYNAMIC AEROELASTIC PROBLEMS

Başkut, Erkut

M.S., Department of Aerospace Engineering

Supervisor : Asst. Prof. Dr. Güçlü Seber

Co-Supervisor : Assoc. Prof. Dr. Altan Kayran

June 2010, 136 pages

In this thesis a fluid-structure coupling procedure which consists of a commercial flow solver, FLUENT, a finite element structural solver, MSC/NASTRAN, and the coupling interface between the two disciplines is developed in order to solve static and dynamic aeroelastic problems. The flow solver relies on inviscid Euler equations with finite volume discretization. In order to perform faster computations, multiple processors are parallelized. Closely coupled approach is used to solve the coupled field aeroelastic problems. For static aeroelastic analysis Euler equations and elastic linear structural equations are coupled to predict deformations under aerodynamic loads. Linear interpolation using Alternating Digital Tree data structure is performed in order to exchange the data between structural and aerodynamic grid. Likewise for dynamic aeroelastic analysis, a numerical method is developed to predict the aeroelastic response and flutter boundary. Modal approach is used for structural response and Newmark algorithm is used for time-marching. Infinite spline method is used to exchange displacement and pressure data between structural and aerodynamic grid. In order to adapt the new shape of the aerodynamic surface at each aeroelastic iteration, Computational Fluid Dynamic mesh is moved based on spring based smoothing and local remeshing method provided by FLUENT User Defined Function. AGARD Wing 445.6 and a generic slender missile are modeled and solved with the

developed procedure and obtained results are compared with numerical and experimental data available in literature.

Keywords: Computational Aeroelasticity, Closely Coupled Approach, Computational Fluid Dynamics, Finite Element Analysis, Flutter, AGARD Wing 445.6, Slender Missile

# ÖZ

STATİK VE DİNAMİK AEROELASTİK PROBLEMLERİN ÇÖZÜMÜ İÇİN SIKI BAĞLI YAKLAŞIM METODU GELİŞTİRME

Başkut, Erkut
Yüksek Lisans, Havacılık ve Uzay Mühendisliği Bölümü
Tez Yöneticisi : Asst. Prof. Dr. Güçlü Seber
Ortak Tez Yöneticisi : Assoc. Prof. Dr. Altan Kayran
Haziran 2010, 136 sayfa

Bu tezde, statik ve dinamik aeroelastik problemlerin incelenmesi için, ticari akış çözücüsü FLUENT, sonlu elemanlar yapısal çözücüsü NASTRAN ve bu iki disiplini birbirine bağlayan arayüzü içeren bir yöntem geliştirilmiştir. Akış, viskozitenin ihmal edildiği Euler denklemleri ve sonlu hacim methodu kullanılarak çözülmüştür. Çözüm süresini kısaltmak için paralel işlemciler kullanılmıştır. Eşleştirilmiş alan aeroelastik problemler sıkı bağlı yaklaşım ile çözülmüştür. Statik aeroelastik analizde, aerodinamik yükler altında oluşan yapısal bozulmaların hesaplanmasında, Euler denklemleri ile elastik doğrusal yapısal denklemler eşleştirilerek beraber çözülmüştür. Yapısal ve aerodinamik çözüm ağlarında bilgi alışverişini sağlamak için, doğrusal interpolasyon kullanan Alternating Digital Tree veri yapısı kullanılmıştır. Dinamik aeroelastik analizler için de, aeroelastik tepkileri ve flutter sınırlarını öngörebilmek için bir sayısal yöntem geliştirilmiştir. Yapısal tepki için modal yaklaşımı, zaman ilermesi için Newmark algoritması kullanılmıştır. Aerodinamik ve yapısal çözüm ağları arasındaki deplasman ve basınç veri alışverişi sonsuz eğri cetveli metodu kullanılarak gerçekleştirilmiştir. Hesaplamalı Akışkanlar Dinamiği çözüm ağı, FLUENT Kullanıcı Tanımlı Fonksiyon Modulü kullanılarak yay prensibi ve yerel çözüm ağları oluşturma yöntemi ile her bir aeroelastik hesaplama adımında, aerodinamik yüzeyin yeni şekline uyacak şekilde hareket ettirilmiştir. AGARD 445.6 kanadı ve narinlik oranı

yüksek bir füze geometrisi modellenmiş, geliştirilen yöntem ile çözülerek, sonuçlar deney verileri ve literatürde bulunan sayısal çözümler ile karşılaştırılmıştır.

Anahtar Kelimeler: Hesaplamalı Aeroelastisite, Sıkı Bağlı Yaklaşım, Hesaplamalı Akışkanlar Dinamiği, Sonlu Elemanlar Analizi, AGARD 445.6 Kanadı, Narinlik Oranı Yüksek Füze

*To my father and mother,*

# ACKNOWLEDGMENTS

I would like to express my appreciation and gratitude to my supervisor Asst. Prof. Dr. Güçlü Seber for his guidance and encouragement throughout this study.

I am greatly indebted to my brother, Nejat Başkut, who guided me through my undergraduate and graduate education with valuable advises and inspiring discussions.

I specially would like to thank to Ali Akgül, Head of Aerodynamics Department in ROKETSAN, for his support and sharing his researches about data structures.

Special thanks go to my ROKETSAN colleagues for their helpful comments, criticisms and moral support.

Finally, I would like to thank to Yasemin for her endless support, understanding and love.

# TABLE OF CONTENTS

# LIST OF TABLES

**TABLE**

# LIST OF FIGURES

**FIGURE**

# LIST OF SYMBOLS

| | |
|---|---|
| ADT | Alternating Digital Tree |
| AGARD | Advisory Group for Aerospace Research and Development |
| b | Half Chord Length at Wing Root |
| $C_D$ | Drag Coefficient |
| $C_L$ | Lift Coefficient |
| $C_P$ | Pressure Coefficient |
| cg | Center of Gravity |
| $[C]$ | Damping Matrix |
| CSD | Computational Structural Dynamics |
| CFD | Computational Fluid Dynamics |
| $E_1$ | Elastic Modulus in Longitudinal Direction |
| $E_2$ | Elastic Modulus in Lateral Direction |
| F{} | Vector of Forces Exerted on the Structure Nodes |
| FEM | Finite Element Method |
| FVM | Finite Volume Method |
| FSI | Flutter Speed Index |
| $\vec{f}_e$ | Rate of Work Done by the Body Forces |
| G | Shear Modulus |
| H | Total enthalpy |
| $[K]$ | Stiffness Matrix |
| $[M]$ | Mass Matrix |
| $\vec{n}$ | Unit Normal Vector |
| q{} | Generalized Displacement Vector |
| $Q$ | Generalized Unsteady Aerodynamic Forces |
| $\dot{q}_h$ | Time Rate of Heat Transfer per Unit Mass |
| $[S]$ | Transformation Matrix |

| | |
|---|---|
| $S$ | Element Surface Area |
| UDF | User Defined Function |
| $V_f$ | Flutter Speed |
| $\vec{v}$ | Flow Velocity |
| $w$ | Deformation of Elastic Structure |
| $\delta_e$ | Elevator Deflection |
| $\delta_r$ | Rudder Deflection |
| $[\delta_a]$ | Displacement of the Aerodynamic Node |
| $[\delta_s]$ | Displacement of the Structure Node |
| $\alpha$ | Angle of Attack |
| $\phi$ | Mode Shape |
| $\omega$ | Natural Frequency |
| $\rho$ | Density |
| $\mu$ | Fraction of Wing Semispan |
| $\lambda$ | Eigenvalue |
| $\xi$ | Damping Ratio |
| $\nu$ | Poisson's Ratio |
| $\Omega$ | Element Volume |
| $\vec{\vec{\tau}}$ | Viscous Stress Tensor |
| $\kappa$ | Thermal Diffusivity Coefficient, |
| $\upsilon$ | Mass Ratio |

# CHAPTER 1

# INTRODUCTION

Aeroelasticity is the study which considers the interaction of inertial, structural and aerodynamic forces for elastic structures. Air-vehicle is usually susceptible to serious aeroelastic problems when light weight and low stiffness structures are used. Increasing rigidity does not necessarily avoid catastrophic failure when sudden atmospheric disturbances, gusts, moving shock waves, etc. occur during the flight. Aeroelastic problems should be considered in the early phase of the air-vehicle structural design since any unstable response to aerodynamic loading may rapidly lead to disastrous structural failure, which may only be treated by major and usually expensive modifications. Wind-tunnel or flight tests are two expensive ways which are performed in the late phase of the design. Therefore, computational aeroelasticity methods are used in order to determine aeroelastic characteristics of the air-vehicle during its development stages.

Collar's aeroelastic triangle (Figure 1.1) shows the interaction of the inertial, structural and aerodynamic forces. Static aeroelasticity studies the interaction of aerodynamic and elastic forces, whereas dynamic aeroelasticity requires all of the three forces to interact. The interaction between these forces may cause several undesirable phenomena which can be grouped into two main categories as static and dynamic aeroelasticity.

Static aeroelasticity considers the non-oscillatory effects of aerodynamic forces acting on the elastic structure [41]. Because of the flexible nature of the structure, aerodynamic forces acting on the structure give rise to structural deformation. This

deflection of the structure tends to redistribute the aerodynamic forces acting on the structure and this interaction continues by leading to each other. Calculated load distribution may be significantly different from that is computed for rigid structure. The effectiveness of the control surfaces is also reduced due to the static aeroelastic effects and it eventually leads to the phenomenon of control reversal which is the loss of the response of a control surface because of the structural deformations. Divergence is another disastrous phenomenon where the aerodynamic moments due to elastic deformations overpower the elastic moments of the structure, bringing the structure to the limit loads and eventually structural failure.

Dynamic aeroelasticity is concerned with the oscillatory effects of the aerodynamic forces [41]. Flutter is the main area of interest of the dynamic aeroelasticity. This dynamic instability involves the interaction of aeroelastic modes of the structure leading to unfavorable coupling of inertial, aerodynamic and elastic forces. Flutter can be defined as the unstable self-excited oscillation in which the structure gains energy from the air-stream and leads to catastrophic structural failure. Because of the unsteady aerodynamics when the air-vehicle oscillates particularly in the transonic regime, prediction of flutter is one of the most complicated issues in computational aeroelasticity.

Buffeting, dynamic response and dynamic stability are the other phenomena covered by dynamic aeroelasticity. Buffeting can be defined as the transient vibration of the aircraft components due to aerodynamic impulses produced by the wake behind wings, nacelles, fuselage pods or other components of the airplane [42]. Transient response of the structure due to impulsive loads (gusts, etc.) can be defined as the dynamic response. Dynamic stability of an air-vehicle may also be affected by the change in the shape of the structure due to unsteady aerodynamic forces.

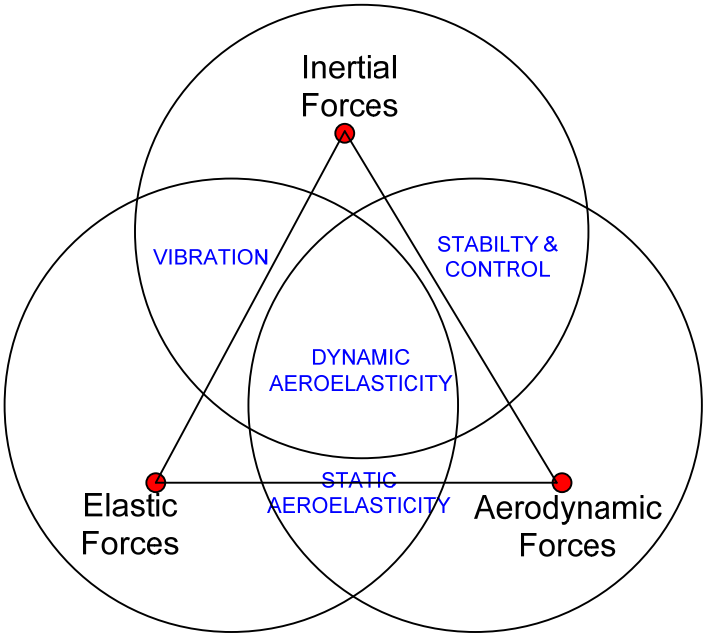


Figure 1.1 Collar's Aeroelastic Triangle

Different levels of complexity may be used in order to model the fluid and structure in computational aeroelasticity as can be seen in Figure 1.2. In general, as the complexity in physics and geometry increases, so does the accuracy of the obtained results and computational time.

Linear analytical methods, which are used in aeroelastic problems, give insufficient results, particularly in the transonic regime where the aerodynamic flow displays highly non-linear behavior. These methods cannot predict the non-linear characteristics and instabilities correctly because of the nonlinear effects arising from oscillating shock waves at this flight regime. Linear theories, which are commonly used in aeroelasticity, are based upon small perturbation theory and thin airfoil theory where the effect of compressibility is introduced in a limited fashion using simple corrections. Transonic small disturbance theory is proved to be an effective method to predict the flutter boundaries accurately at subsonic and supersonic flight regime. However, it cannot predict the dip accurately at transonic flight regime where significantly higher flutter

speed is predicted [36]. Most of the commercial codes such as the aeroelastic module of NASTRAN utilize these linear aerodynamic theories to predict the aeroelastic behavior.

Accuracy of aeroelastic modeling can be improved by using high level aerodynamic models based on the conservation laws and finite element formulation of the structure. These methods fully account for nonlinear effects during aeroelastic analysis, which results in more accurate prediction of aeroelastic response and instabilities. Continuity, momentum and energy conservation laws together with the equation of state are generally utilized by CFD methods in order to solve the flow around air-vehicles. The Navier-Stokes equations may also be solved for viscous flows. Euler equations, which assumes inviscid flow is reduced form of Navier-Stokes equations and gives acceptable results in the transonic regime excluding the region of transonic dip [36]. Transonic dip is important, because it shows the minimum velocity at which flutter may occur across the flight envelope. The flow may be assumed to be inviscid or viscous effects may be included in order to determine the aeroelastic characteristics when these nonlinear models are used. Coupling Euler equations and normal modes of the structure is found to be over-conservative and significantly lower flutter speed is predicted [36]. Including the viscous effects is found to improve the prediction of transonic dip [44].

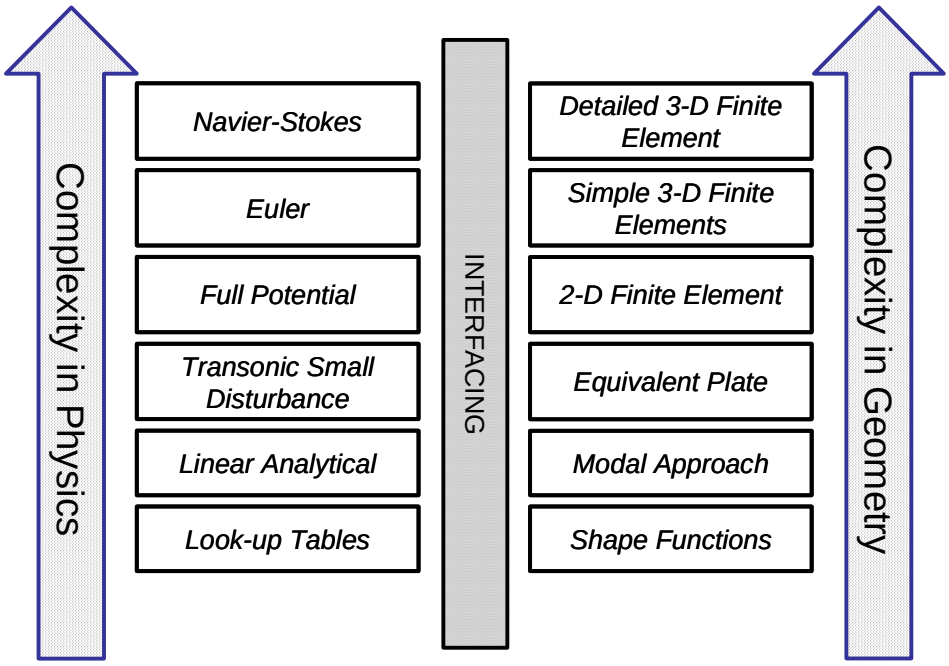


Figure 1.2 Varying Levels of Complexity in Modeling for Fluids and Structures [12]

The main objective of this thesis is to develop an interference between the two disciplines, namely the structural dynamics and aerodynamics, in order to determine static and dynamic aeroelastic properties of air-vehicles.

The most of the structural deformation on the body takes place because of pressure forces on the body rather than friction forces. In order to decrease the computational cost, Euler equations are used for CFD, whereas 3-D finite element method is used for the structural analysis.

## *1.1 LITERATURE REVIEW*

In this part of the dissertation, details and literature review of time advancing schemes, mesh deformation methods, and interference methods which are commonly used in computational aeroelasticity are given.

### *1.1.1 Time Advancing Schemes*

There are three major methods which are used to advance in time for fluid-structure simulation: monolithic approach, closely coupled approach, and loosely coupled approach [28].

In the monolithic approach, fluid and structure governing equations are combined into one single equation set and these equations are solved using a unified solver simultaneously. The main advantage of this approach is that fluid and structure are synchronized while advancing a single time step so that fully consistent coupling is preserved. This leads to robustness and stability and allows large time steps to be chosen.

When loosely and closely coupled approach is used, the structural and fluid equations are solved by using separate solvers.

In the closely coupled approach, fluid and structure systems are also synchronized at each time step. A partitioned scheme is used for synchronization where fluid and structure solvers are separate. Fluid loads and structural displacements are exchanged within a single time step. In this approach, sub-iterations are performed until the fluid and structure systems are fully converged at each time step. The main advantages of the

closely coupled approach are synchronicity property and algorithmic flexibility for physically different systems.

The loosely coupled approach is also a partitioned scheme. But, the fluid-structure system is not sub-iterated to full convergence at each time step. The main disadvantage of this method is that the fluid and structure solution updates are lagged. This method is usually used for the aeroelastic problems with moderate nonlinearity. The two systems are never fully in phase. This introduces a temporal error in addition to the truncation error of the fluid and structure interference schemes. Partitioned approach and small computational expense per time step are the advantages of the loosely coupled approach [28].

Liu et al. [4] presented a fluid-structure code, which is based on Euler/Navier-Stokes equations, in order to determine the flutter characteristics. The flow solver and structural modal equations are strongly coupled with each other. In order to avoid time delay between flow and structural system, a dual time stepping scheme was used.

Schuster [33] coupled the linear structural model with the 3-D flow solver in order to solve the aeroelastic problems of an aircraft. The linear generalized mode shapes for structural model and thin layer approximations to the RANS equations were used.

Melville et al. [39] presented a fully coupled approach, which modal structural equations are coupled with a flow solver using an approximate factorization scheme.

Lee-Rausch and Batina [34] coupled implicit, Euler and Navier-Stokes equations with a modal structure solver.

Guruswamy and Byun coupled Euler equations with finite element structures which is modeled by using plate elements; and Navier Stokes equations with finite element structure which is modeled by using shell elements to solve dynamic aeroelasticity problems [15], [48].

Doi [40] coupled an explicit fluid solver (TFLO) with the finite element structure solver (MSC/NASTRAN) to predict the aeroelastic characteristics of a rotor blade.

Bendiksen [31] used the 'Arbitrary Lagrangian Eulerian formulation' to solve the wing flutter problem of an airfoil in the transonic regime. Interference between two systems is performed by switching from Euler description to Lagrangian description at fluid-structure interface.

Alonso and Jameson [30] coupled Euler code with a modal pitch-plunge structural model of an airfoil. Information between CFD and CSD domains was exchanged at the each pseudo time integration and the entire system was fully converged at each physical time-step.

Luca et al. [32] presented a loosely coupled approach where aerodynamic and structural systems are integrated with an implicit algorithm. An implicit Euler flow solver was used for the aerodynamics and the structure was represented by a modal description. Predictor and corrector steps based on Crank-Nicholson algorithm were used at each time step. Displacement values, which are predicted in the first step, corrected with the new unsteady aerodynamic loads in the second step of the procedure.

### *1.1.2 Mesh Deformation Methods*

Mesh deformation in computational aeroelasticity applications is one of the important aspects and therefore it must be handled carefully. In order to represent the deformation of the structure during the aeroelastic simulation, aerodynamic grid must be deformed consistently and mesh quality must be maintained to avoid any numerical problem. Simply deforming the CFD grid is considerably cheaper and more convenient than

remeshing of the entire CFD domain; therefore it is commonly used in computational aeroelasticity.

In literature, several techniques exist in order to apply mesh deformations consistent with the motion of the structure in the CFD domain.

Batina [7] proposed a method, which is based on the spring analogy, for unstructured grids. In this method, spring stiffness of an element edge is assigned to be inversely proportional to the edge length. Spring analogy is implemented easily but it is not robust since especially under large deformations cells collapse in the computational domain resulting in singularities in the flow solution.

Farhat et al. [8] proposed a modification to the spring analogy for 2-D meshes by including additional torsional springs in order to control mesh skewness. This method offers many advantages in terms increased robustness and performance.

Murayamai Nakahashi and Matsushima [9] expanded the use of torsional springs for 3-D unstructured meshes.

Robinson et al. [10] presented an extension of the spring analogy for structured grids. The deformation algorithm was based on a network of interconnected springs in edges of the hexahedral cell. However, it was concluded that this method was computationally expensive.

Zhang and Belegungu [11] calculated the spring stiffness using the ratio of the cell Jacobian to the cell volume. They concluded that this algorithm can handle large mesh deformation.

Löhner and Yang [19] proposed a method based on Laplacian smoothing with variable diffusivity according to distance from surface.

Tezduyar and Behr [13] proposed a mesh deformation algorithm based on linear elasticity. Cavallo et al. [14] included additional stress terms and use minimal residual algorithm to solve equations of linear elasticity and concluded that their approach can

preserve mesh quality for large boundary deformations. Stein et al. [16] used this method with varying elastic stiffness which is proportional to cell volumes. They concluded that mesh quality in boundary-layers and regions of high resolution is preserved.

For the aerodynamic shape optimization study, Nielsen and Anderson [27] also applied the linear elastic analogy. They defined the mesh material stiffness according to the cell aspect ratio so that mesh is not deformed near the moving boundary as much as cells farther away from the boundary.

### *1.1.3 Interference between CFD and CSD Grids*

Computational aeroelasticity requires a fluid-structure interface to transfer the aerodynamic loads and structural displacements at this common boundary, which is usually the wetted surface on the structure. The aerodynamic and structural grids generally do not coincide and not lie on the same surface since the requirements are different for the corresponding systems. Therefore, interpolation of aerodynamic pressure loads and displacements must be implemented between the two systems by a carefully implemented method. The performance of such a method depends on the accuracy and robustness of the interpolation scheme. Several studies in the literature raised the importance of conservation of momentum and energy in the transfer of loads and displacements [28]. If the transfer of structural grid displacements to the fluid grid is defined as:

$$[\delta_a] = [S][\delta_s] \tag{1.1}$$

The force transformation from the aerodynamic to structural grid uses the virtual work principle [47]. In order to transfer aerodynamic pressure loads from the CFD grid points

to the CSD grid points, transpose of the displacement transformation matrix, which ensures a conservative transfer of energy between the two systems, is used.

$$[F_s] = [S]^T [F_a] \tag{1.2}$$

Prediction of complex dynamic aeroelastic phenomena such as flutter and limit cycle oscillation is sensitive to the conservation properties. An imbalance in energy transfer between the fluid and structure systems causes instability and must be avoided [28].

There are also some studies which does not need any interference algorithm between the two different disciplines. The nodes at the surface of the CFD are also the elements of structural finite element model. Thus, same surface grid may be used for the flow and structural analyses. Data exchange between the two systems is performed at this matching discrete interface without using any interpolation algorithm. Bendiksen and Hwang [29] proposed a finite element algorithm for both CFD and CSD equations and used the same surface grids for the flow and structural analyses.

The infinite plate spline method which is commonly used in aeroelasticity was firstly proposed by Harder and Desmarais [22]. This method is suitable for displacement and force transfer of wing-like components which is modeled by plate or shell elements.

Duchon [17] presented thin plate spline method for interpolation of displacements and forces at 3-D structural grid points. Only difference from the infinite spline method is the addition of the out of plane component.

The beam spline method is used for body-like components or high aspect ratio wing structures which are modeled by beam elements. The beam spline method solves the partial differential equation of equilibrium for an infinite beam with uniform bending and torsion stiffness [20].

Luca et al. [32] proposed an interfacing method based on least square method which ensures the conservation of energy and momentum transfer between the structure and fluid systems.

# CHAPTER 2

# COMPUTATIONAL AEROELASTICITY

Computational Aeroelasticity (CAE) may be defined as the coupling of CFD methods with structural dynamics formulations in order to model an aeroelastic system and perform analysis. Accuracy of the aeroelastic analysis depends on the selection of computational methods, interpolation schemes, and mesh deformation methods. In this part, some details of the interaction between the two disciplines, the flow and the structural finite element solvers, mesh deformation techniques, and interpolation methods that have been investigated as a part of this research are presented.

## *2.1 TIME ADVANCEMENT SCHEME*

In the present study, a closely coupled approach is used for time advancing as illustrated in Figure 2.1. In this approach, at each time step corrective sub-iterations are performed until the fluid and structure are synchronized and the entire aeroelastic system is fully converged. Then, new unsteady aerodynamic loads and corresponding structural displacements are calculated for the next time step. This process is repeated until a specified flow time is reached.

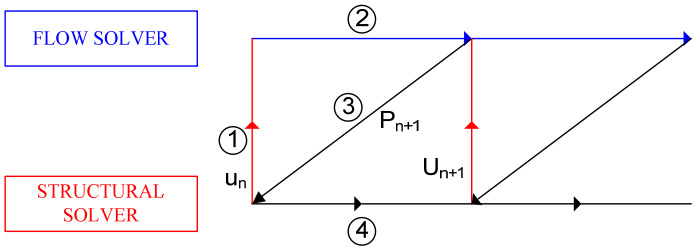


Figure 2.1 Closely Coupled Approach

## *2.2 MESH DEFORMATION METHODS*

In this part, details of mesh deformation methods based on FLUENT mesh deformation algorithm and linear elastic finite element based deformation method which can be implemented by using any structural finite element program are given and some test cases are presented.

### *2.2.1 FLUENT MOVING MESH ALGORITHM*

FLUENT consists of three mesh deformation methods which can be used to update the volume mesh in the deforming regions at the boundaries subject to the motion [6]. These methods are called as spring-based smoothing, dynamic layering and local remeshing.

In the spring-based smoothing method, the edges between any two mesh nodes are idealized as an interconnected springs which form a network. A displacement at a given

boundary node will generate a force proportional to the displacement along all the springs connected to the node [6]. Spring-based method preserves mesh connectivity but needs large amount of CPU time and memory. It is also limited to relatively small deformations when it is used as a standalone mesh deformation scheme. The spring-based smoothing, of which details are given in [6], is shown in Figure 2.2 for a cylindrical cell zone where one end of the cylinder is moving.

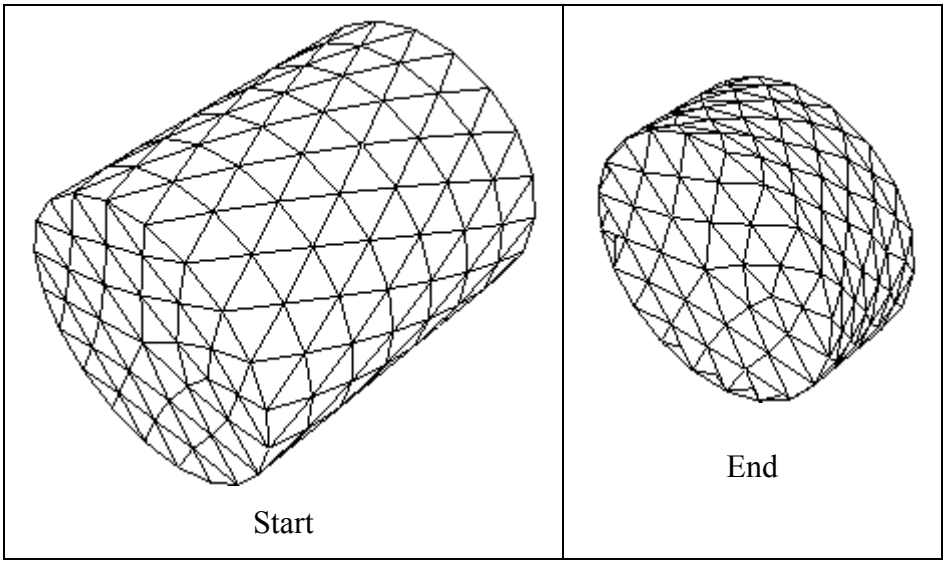


Figure 2.2 Spring Based Smoothing on Interior [6]

The second method, dynamic-layering, can be used in prismatic (hexahedral or wedge) mesh zones in order to add or remove layers of cells adjacent to a moving boundary, based on the height of the layer adjacent to the moving surface [6].

The third method is remeshing. The cell quality may deteriorate and cells may become degenerate if the boundary displacement is large compared to the local cell sizes. This leads to negative cell volumes which results in convergence problems in flow solution [6]. Remeshing can eliminate the collapsed cells, but adds extra computational costs.

FLUENT locally replaces the degenerated cells until the new cells or faces satisfy the size and skewness criterions [6]. FLUENT includes several remeshing methods. These include local remeshing, local face remeshing, face region remeshing and 2.5 D surface remeshing [6]. The available remeshing methods in FLUENT work for triangular or tetrahedral zones. As cells are added or removed, connectivity changes during the deformation process.

The two-dimensional mesh, which is used for a test case, has a total of 7,364 triangular elements and 37,688 nodes. The grid density is high near to the airfoil leading and trailing edges. The baseline mesh with unstructured triangular elements is shown in Figure 2.4. The chord of the airfoil NACA0010 (Figure 2.3) has a length of 40 units. In order to determine proper mesh deformation parameters which allow maintaining mesh quality and representing the structural deformation correctly, 2-D mesh is deformed in two different ways. Firstly, airfoil is translated by chord/2 in the x direction. Secondly, airfoil is rotated 45° about the leading edge.

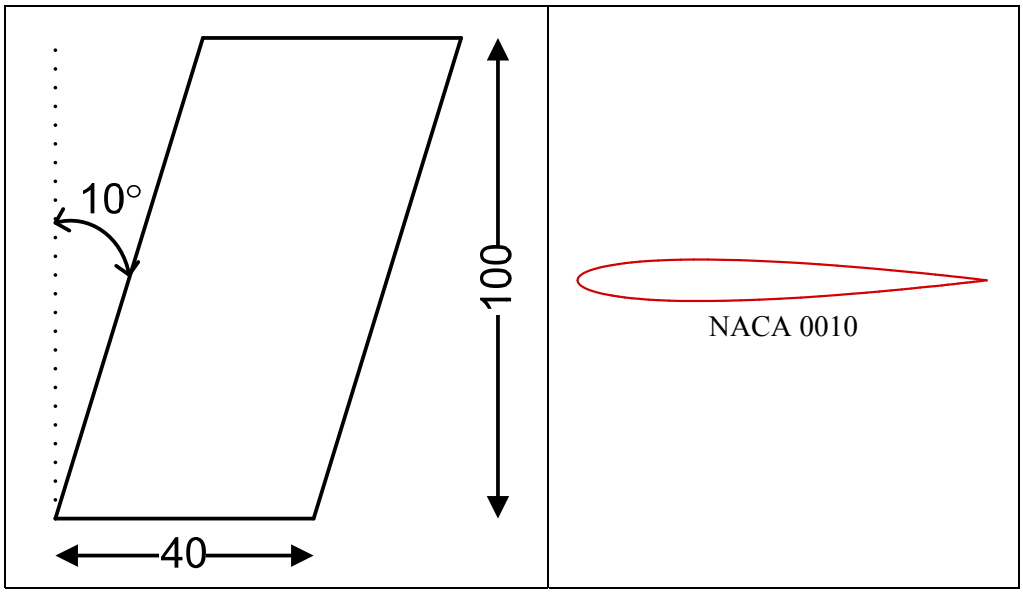


Figure 2.3 3-D Wing Planform and Airfoil Cross-section Used for Mesh Deformation Studies

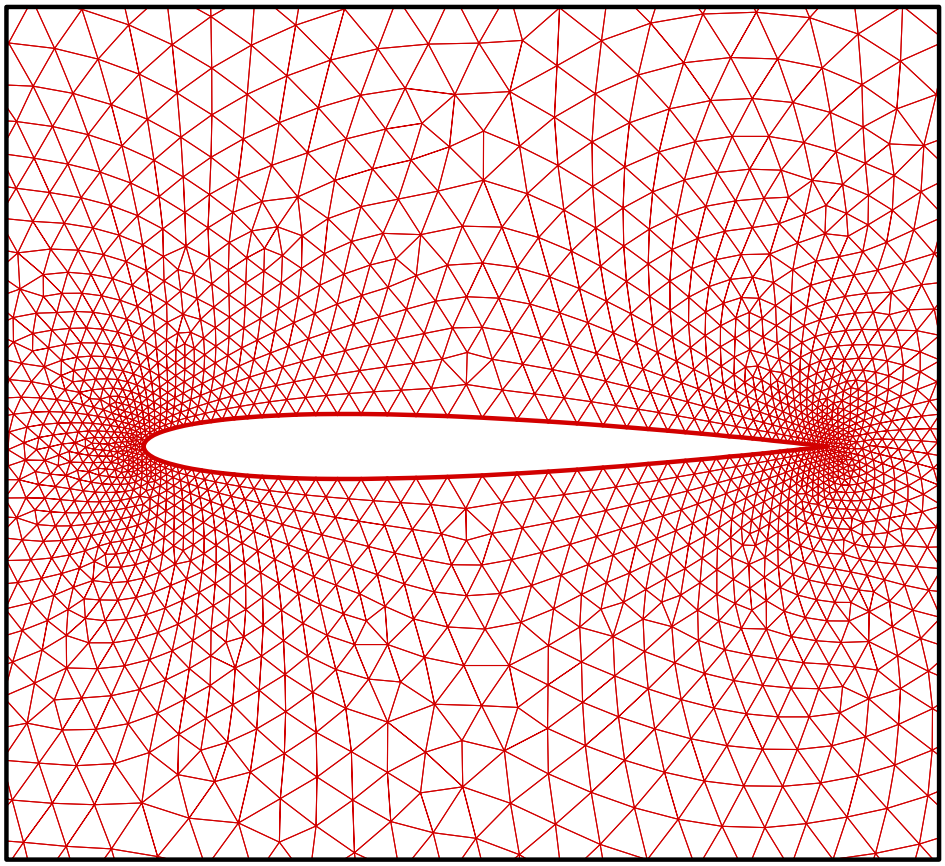

Figure 2.4 Two-Dimensional Triangular Mesh Used as a Test Case for Deformation Studies

Figures 2.5 and 2.6 show the mesh patterns obtained from the FLUENT mesh deforming process for the two deformation cases, respectively. Since FLUENT deforms the mesh according to the pre-defined parameters, skewness and cell size of the grids are kept under control during the deforming process. As can be seen in Table 2.1, mesh quality is preserved almost completely after the deformation process.

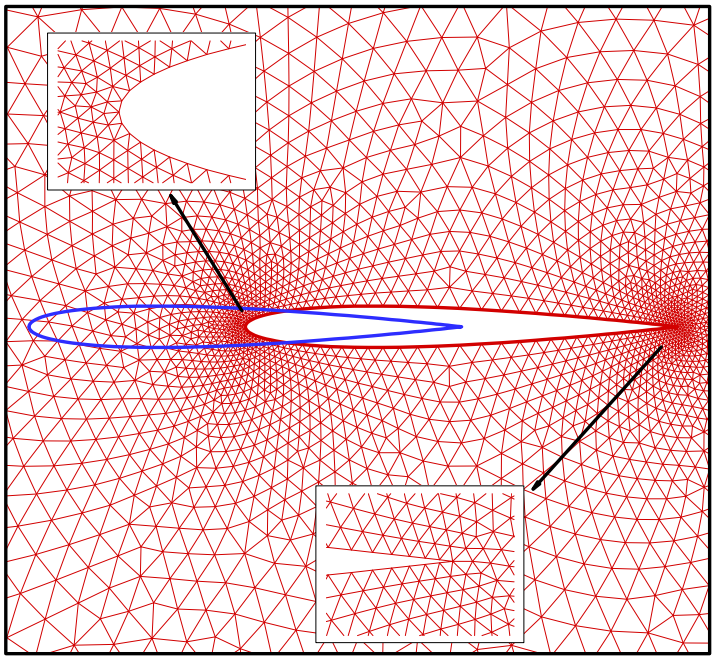

Figure 2.5 Translation of airfoil by chord/2 unit in the x-direction (blue: initial position of the airfoil)

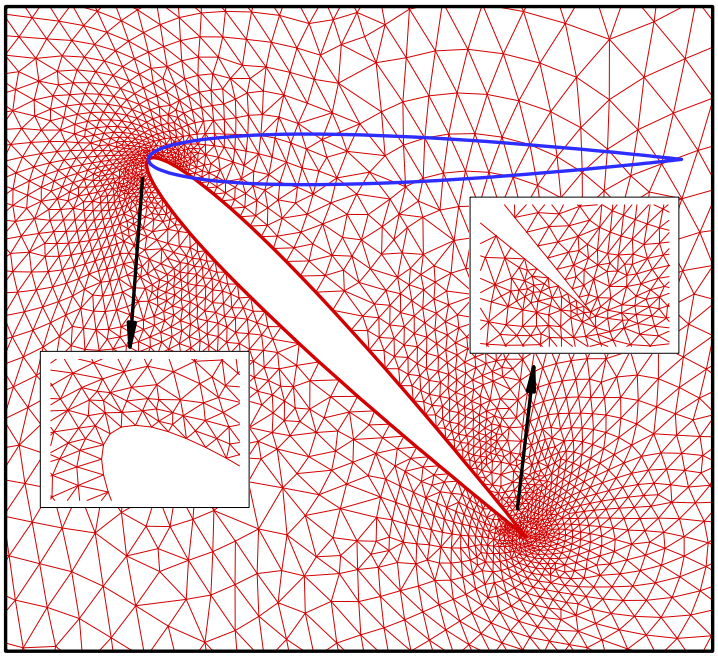

Figure 2.6 Rotation of airfoil by 45° about leading edge (blue: initial position of the airfoil)

Table 2.1 FLUENT 2-D Mesh Deformation Test Case Results

| | Number of Triangular Cells | Maximum Cell Equiangle Skew | Maximum Cell Equisize Skew | Maximum Cell Aspect Ratio |
|---|---|---|---|---|
| Base Grid | 7364 | 0.434 | 0.467 | 1.562 |
| 0.5*chord Translation | 7364 | 0.434 | 0.465 | 1.558 |
| 45° Rotation About Leading Edge | 7758 | 0.584 | 0.450 | 1.540 |

The three-dimensional mesh, which is used for a test case, has a total of 833,772 tetrahedral elements. The baseline mesh with unstructured tetrahedral elements and created planes which help to observe the grid quality during deformation process are shown in Figure 2.7 and 2.8, respectively. Mid-plane is located at the middle of the root chord location of the swept wing. Geometrical properties of the wing are shown in Figure 2.3.

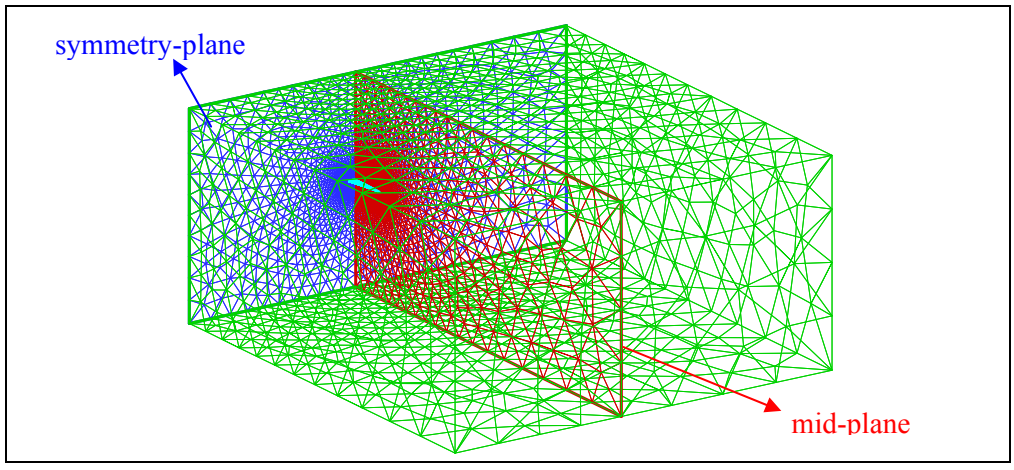


Figure 2.7 Three-Dimensional Triangular Mesh Used as 3-D Test Case for Deformation Studies

In order to determine proper mesh deformation parameters, which allow maintaining mesh quality and representing the structural deformation correctly, wing is deformed in-z-direction with varying magnitudes. The magnitude of the deflection at the wing tip is 3% of the wingspan. It linearly decreases towards to the wing root, up to zero value.

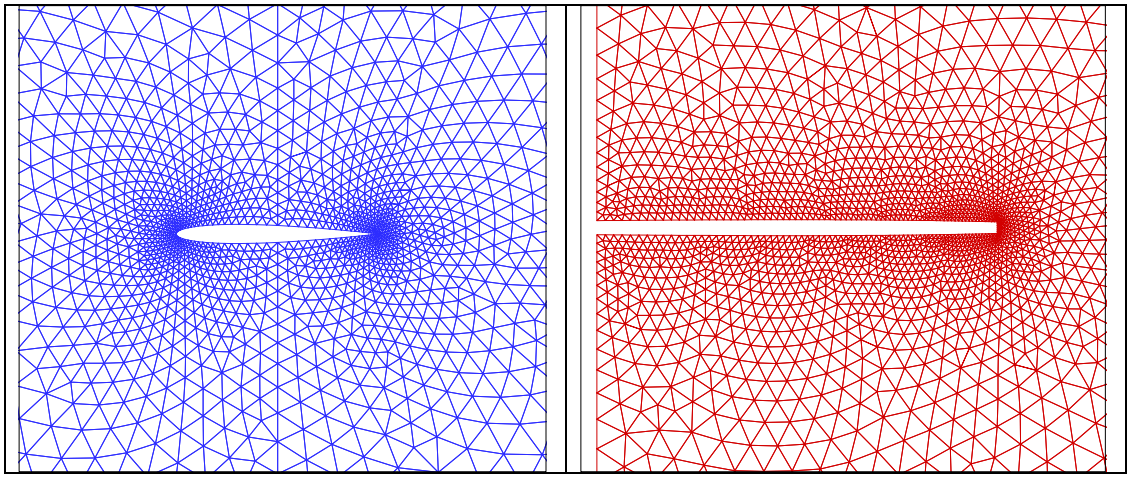

Figure 2.8 Initial Mesh Patterns at Symmetry and Mid Planes of the 3-D Test Case for Deformation Studies

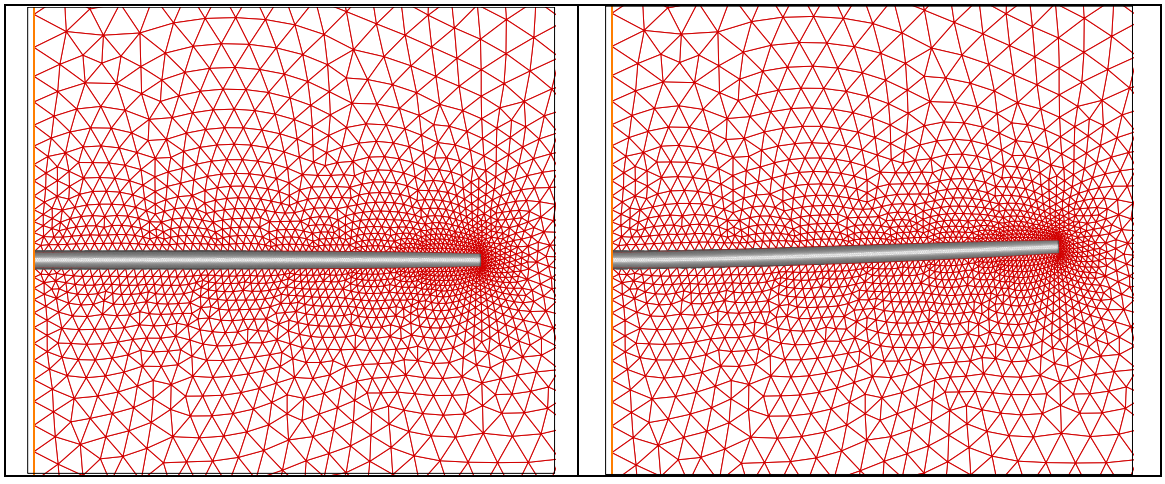

Figure 2.9 Initial and Final Position of the 3-D Test Case Wing and Mesh Patterns at the Mid-Plane

As can be seen from Figures 2.9 and results shown in Table 2.2, deformed grid has good quality that may avoid any numerical problems during the CFD simulation. Cell skewness and aspect ratio values are almost preserved during the deforming process. Number of element increases, since FLUENT replaces the collapsed or deteriorated cells with new cells in order to maintain the quality of the mesh.

Table 2.2 FLUENT 3-D Mesh Deformation Test Case Results

| | Number of Tetrahedral Cells | Maximum Cell Equiangle Skew | Maximum Cell Equisize Skew | Maximum Cell Aspect Ratio |
|---|---|---|---|---|
| Base Grid | 833772 | 0.814 | 0.785 | 3.452 |
| Maximum tip deflection (3 % of the Wingspan) | 855625 | 0.813 | 0.765 | 3.440 |

### *2.2.2 LINEAR ELASTIC FINITE ELEMENT BASED MESH DEFORMATION METHOD*

In this method, an analogy is used and the CFD computational domain is defined as a finite element mesh for a domain of an isotropic linear elastic continuum with a local Young modulus inversely proportional to the cell volume of each element. In order to obtain the deformed CFD mesh, the outer boundaries of the CFD domain are held fixed. And structural displacements at each boundary node are used as the boundary condition for the finite element analysis. The resulting equations are then solved using MSC/NASTRAN finite element program. Main objective of this method is to use of the available finite element based structural solver. This method preserves mesh connectivity and allows fixed outer boundary of the computational domain which can be easily implemented for deforming-boundary CFD calculations. In this method, cell

skewness and size parameters cannot be controlled during the deformation in order to preserve or improve mesh quality. This is the main disadvantage of linear elastic finite element based mesh deformation method.

The mesh deformation is obtained by a single linear elastic finite element analysis with fictitious non-uniform elastic properties. In order to control the mesh movement, the Young's modulus E is defined as Eqn 2.1. Poisson's ratio ν, is assumed to be zero for convenience. Large cells far from moving boundary are intentionally softened.

$$E = c.f(K) \tag{2.1}$$

Where; K is a function which decreases with the cell volume in CFD domain and c is a constant parameter which controls the stiffness level of the cells. In this study, choosing c value as $10^4$ gives satisfactory results.

In order to examine deformed mesh quality after deformation process, a 2-D mesh (Figure 2.4) is deformed in two different ways. Firstly, airfoil is translated by chord/2 unit in the x direction. Secondly, airfoil is rotated 45° about the mid-chord. Figures 2.10 and 2.11 show the mesh patterns obtained from the finite element based mesh deforming process for the two deformation cases.

It can be concluded that, artificial material stiffness property created in finite element based deformation method with varying elastic properties according to the cell volume can be implemented for mesh deformation problems. As can be seen, no overspill is observed in the results. But, since cell skewness and cell size parameters cannot be controlled, mesh quality decreases especially for large boundary deformations during the deformation process (Table 2.3). On the other hand, number of triangular elements and cell connectivity does not change during the deformation process since no mesh is removed or added to the domain.

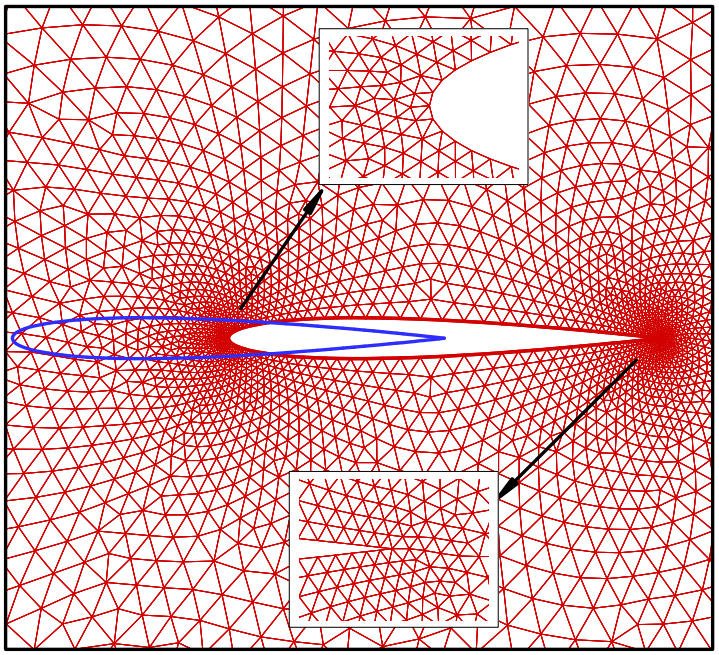

Figure 2.10 Translation of airfoil by chord//2 unit in the x direction

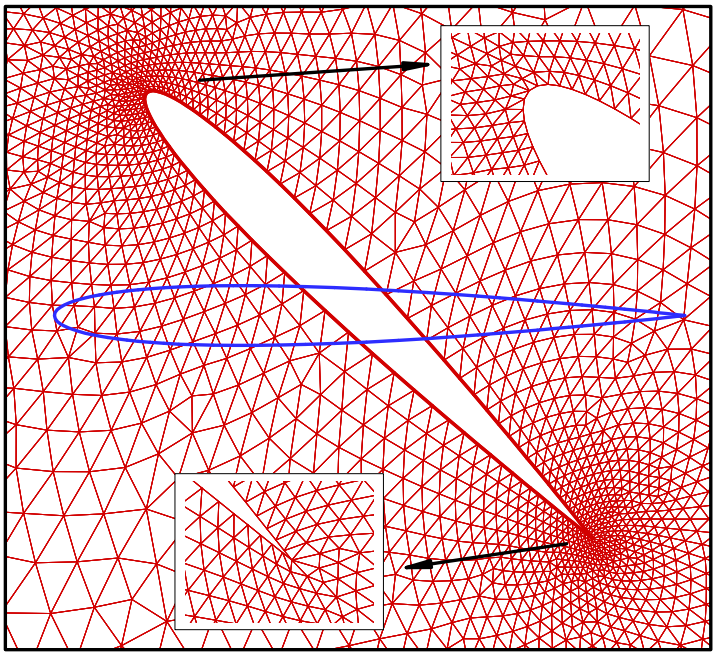

Figure 2.11 Rotation of airfoil by 45° about the mid-chord (blue: initial position of the airfoil)

Table 2.3 Linear Elastic Finite Element Based Method 2-D Mesh Deformation Test Case Results

| | Number of Triangular Cells | Maximum Cell Equiangle Skew | Maximum Cell Equisize Skew | Maximum Cell Aspect Ratio |
|---|---|---|---|---|
| Base Grid | 7364 | 0.434 | 0.467 | 1.562 |
| 0.5*chord Translation | 7364 | 0.462 | 0.486 | 1.600 |
| 45° Rotation About Mid-chord | 7364 | 0.531 | 0.700 | 2.310 |

Since quality of the mesh can be easily controlled and preserved according to the pre-defined parameters, FLUENT moving mesh algorithm will be used for the further static and dynamic aeroelastic analyses.

## *2.3 INTERFERENCE BETWEEN CFD and CSD GRIDS*

In this part, three interpolation techniques are described: Linear Interpolation Method using Alternating Digital Tree (ADT) geometric search algorithm, which is used in static aeroelastic analysis, thin plate spline method and infinite spline method, which is used in the dynamic aeroelastic analysis.

### *2.3.1 Linear Interpolation using Alternating Digital Tree Data Structure*

Data structures such as binary tree, quad tree, oc tree, etc., convert the unstructured form of data into structured form in order to speed up the search process. These algorithms impressively decrease the searching and sorting time when they are used for mapping applications in computational aeroelasticity.

Alternating Digital Tree (ADT) is a spatial binary tree data structure used for searching and sorting data operations. In order to construct ADT, firstly a root domain is defined. An element is assigned to one of two branches based upon the geometric conditions which are satisfied by the bounding box of that element. This procedure is repeated for all the elements in the domain and finally an Alternating Digital Tree is built up.

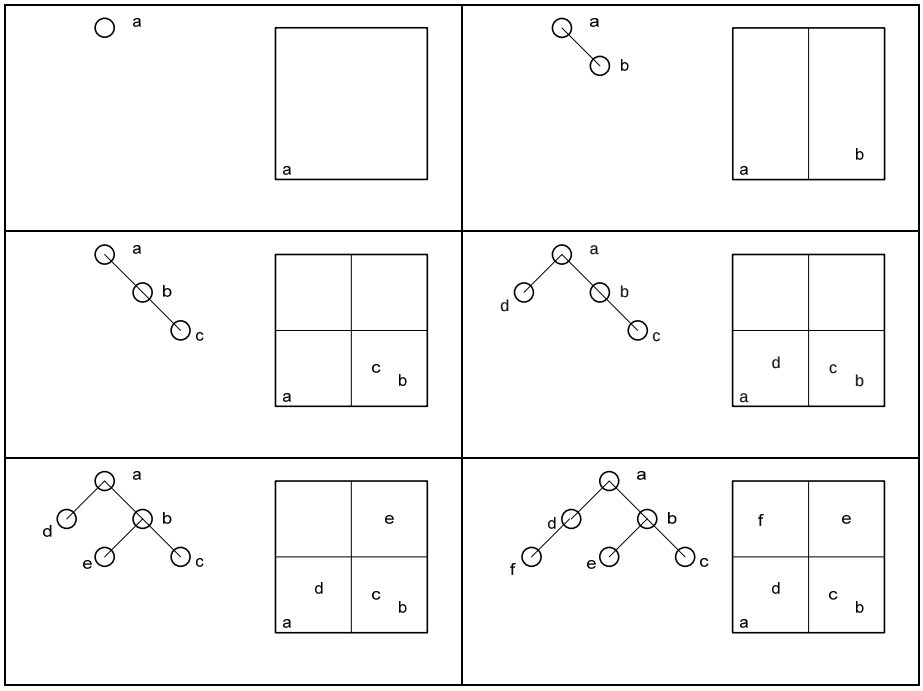


Figure 2.12 Alternating Digital Tree Construction

Mesh data is stored in a form of Alternating Digital Tree and used for interpolation procedure. In Figure 2.12, the first point “a” is the root of the binary tree and the whole domain. Point “b” is the in the region that is on the right half of “a”’s domain. Therefore, “b” is placed as the right child of “a” that is it is on the right side of the bisector of the region. Point “c” is on the right side of the domain. But point “b” is already been assigned to this region, thus point “c” is tested for whether it is on the left or right of the new bisector of “b”’s region. These steps are repeated for the all points in the domain.

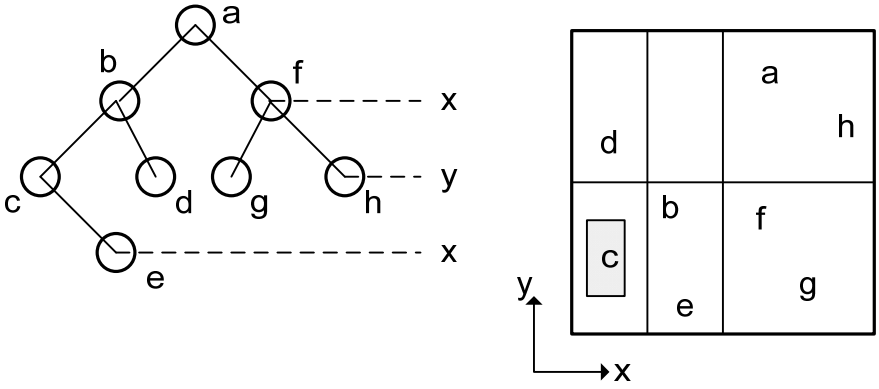


Figure 2.13 Alternating Digital Tree Search

In Figure 2.13, a sample ADT search steps are shown. In order to search the points lying within the rectangular shaded region, firstly, the whole domain (a) is tested whether it lies within the rectangular region. The regions corresponding to its left and right son (b and f) are tested whether they overlap with rectangular region. The region which overlaps the rectangular region is tested if associated point lies within the rectangular region. Then, its own left and right sub-regions are tested for intersection. These steps are repeated until all nodes have been tested.

The sub-regions of the right son of "a" does not overlap with the rectangular region. Therefore, it is unnecessary to search the test points "g" and "h" since their sub-regions lie within their parent's region. By this method, each search step impressively reduces the number of points to be checked by a factor of two, resulting in reduced search time by amount of the logarithm of the number of points.

In the present static aeroelastic analyses, Alternating Digital Tree (ADT) geometric search algorithm (ADTSearchIn) and linear interpolation method developed in [25] is used to transfer displacement and pressure data between the two grid systems. This study [25] creates ADT for a given region described by its points (source), searches for surface elements which enclose the specified points (target), and evaluates values of variable by linear interpolation.

In Figures 2.14 and 2.15, examples of building up ADT for AGARD Wing 445.6 and Basic Finner Rocket are shown, respectively. As can be seen, generated digital trees are concentrated near to the grid boundaries of the structure.

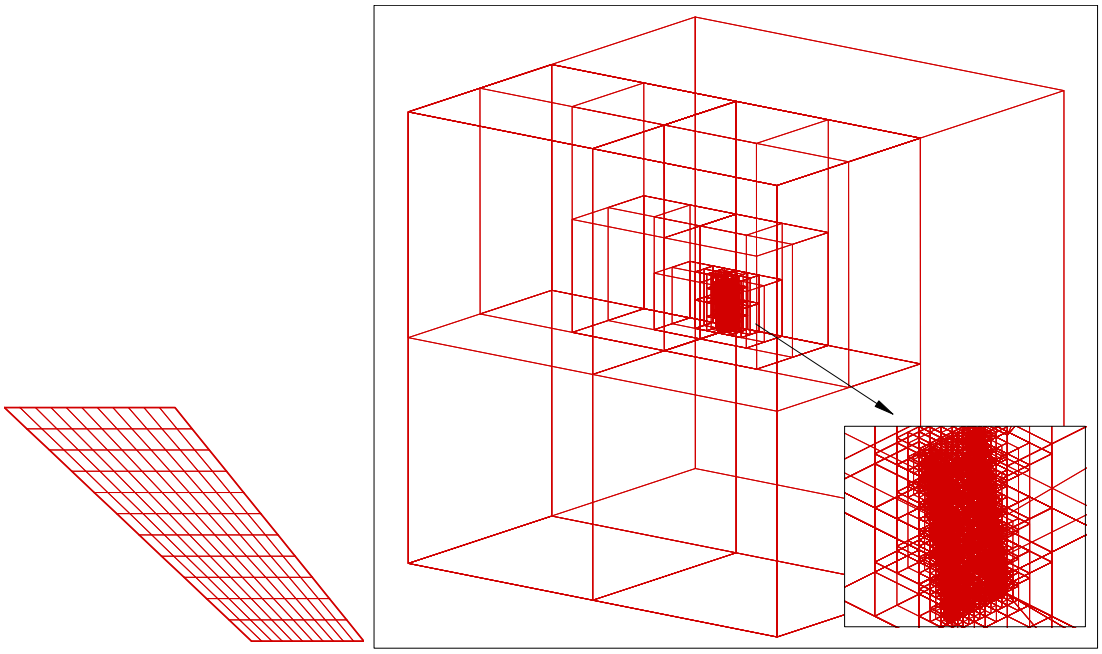

Figure 2.14 Building up Alternating Digital Tree Search for AGARD Wing 445.6 Structural Model (left: CSD grid, right: overall ADT brick)

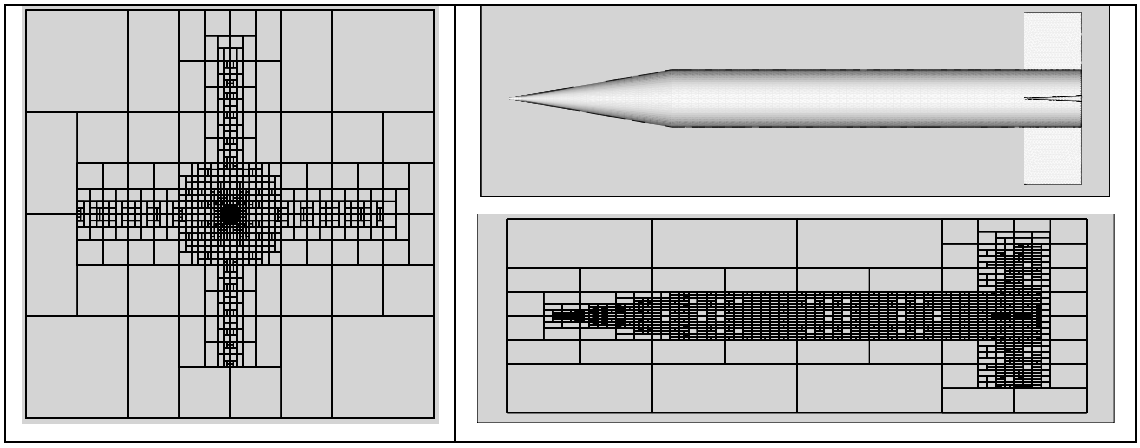

Figure 2.15 Example of ADT Built with the Points of the Grid Boundaries for 3-Dimensional Basic Finner Rocket [25]

Linear interpolation is conducted using the Inverse Distance Weighting (IDW) method. Aerodynamic grid points are projected on the structure surface as shown in Figure 2.16. Then, structural element which aerodynamic grid point lies within is defined for each aerodynamic node. The degree of influence of the each structural grid of the corresponding element is calculated by Eqn 2.2, which is based upon the weighted distance of the aerodynamic grid node from the grid points of the structural element. In other words, points that are closer to the node will have greater degree of influence on the calculated value than those that are farther away.

$$\delta_n = \left( \delta_1 \frac{1}{r_1} + \delta_2 \frac{1}{r_2} + \delta_3 \frac{1}{r_3} + \delta_4 \frac{1}{r_4} \right) \left( \frac{r_1.r_2.r_3.r_4}{r_2.r_3.r_4 + r_1.r_3.r_4 + r_1.r_2.r_3} \right) \tag{2.2}$$

where $n$ represents the aerodynamic grid point and $\delta$ is the variable that is interpolated from CSD grid nodes to CFD grid nodes.

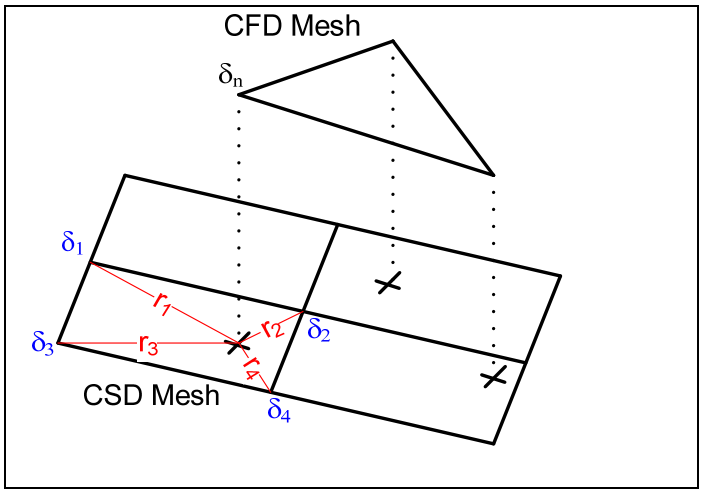


Figure 2.16 Illustration of Projections of CFD Grid Points on the CSD Surface and Linear Interpolation

Similarly, linear interpolation from CSD grid to CFD grid is used by Eqn 2.3 and illustrated in Figure 2.17.

$$P_n = \left( P_1 \frac{1}{r_1} + P_2 \frac{1}{r_2} + P_3 \frac{1}{r_3} \right) \cdot \left( \frac{r_1 . r_2 . r_3}{r_2 . r_3 + r_1 . r_3 + r_1 . r_2} \right) \tag{2.3}$$

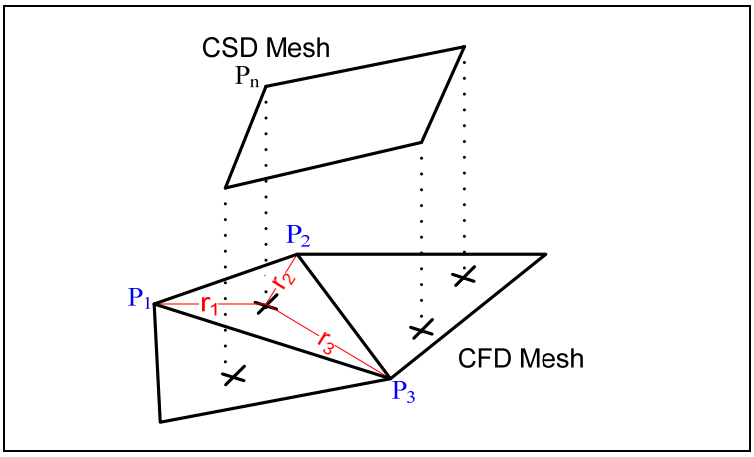


Figure 2.17 Illustration of Projections of CSD Grid Points on the CFD Surface and Linear Interpolation

Results of linear interpolation using ADT data structure are shown in Figures 2.18-2.20. It can be concluded that, using linear interpolation gives admissible results and ADT search algorithm dramatically reduces the interpolation time.

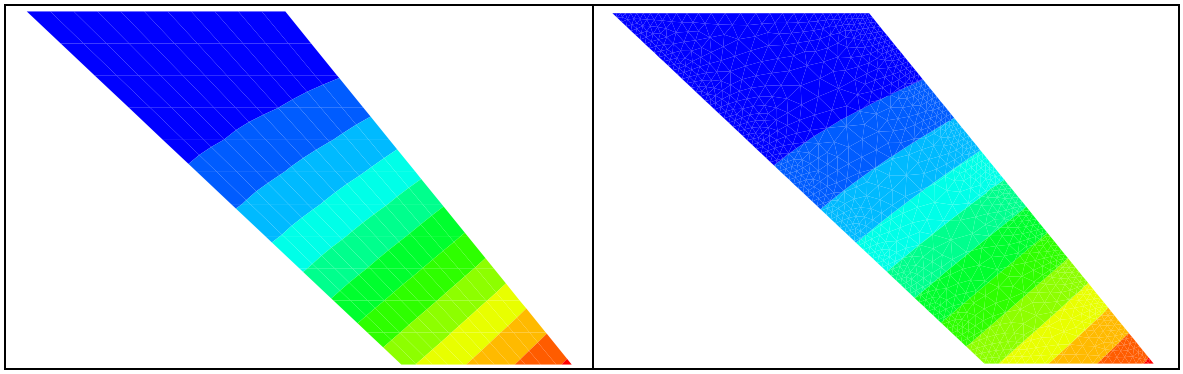

Figure 2.18 Out-of-Plane Deformation Interpolated from CSD (left) Grid to CFD (right) Grid (Linear Interpolation Method using ADT Algorithm)

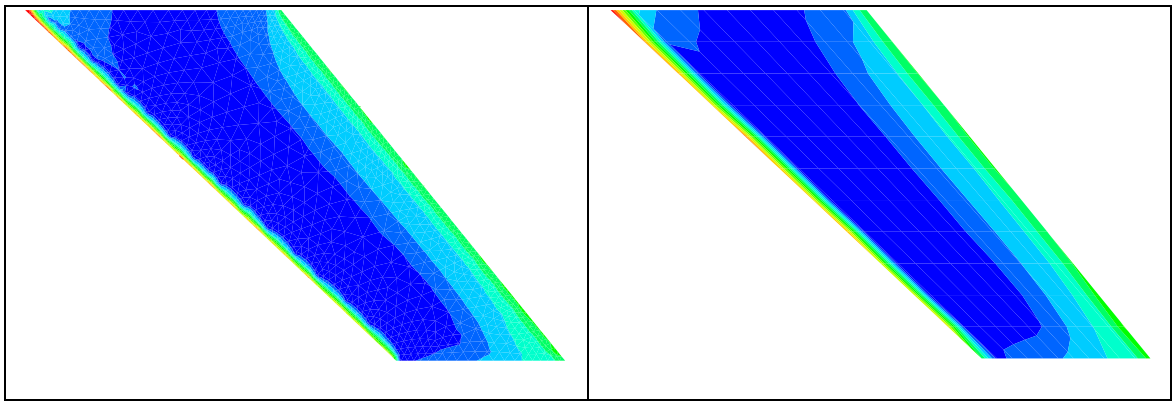

Figure 2.19 Pressure Interpolation from CFD (left) Grid to CSD (right) Grid (Linear Interpolation Method using ADT Algorithm)

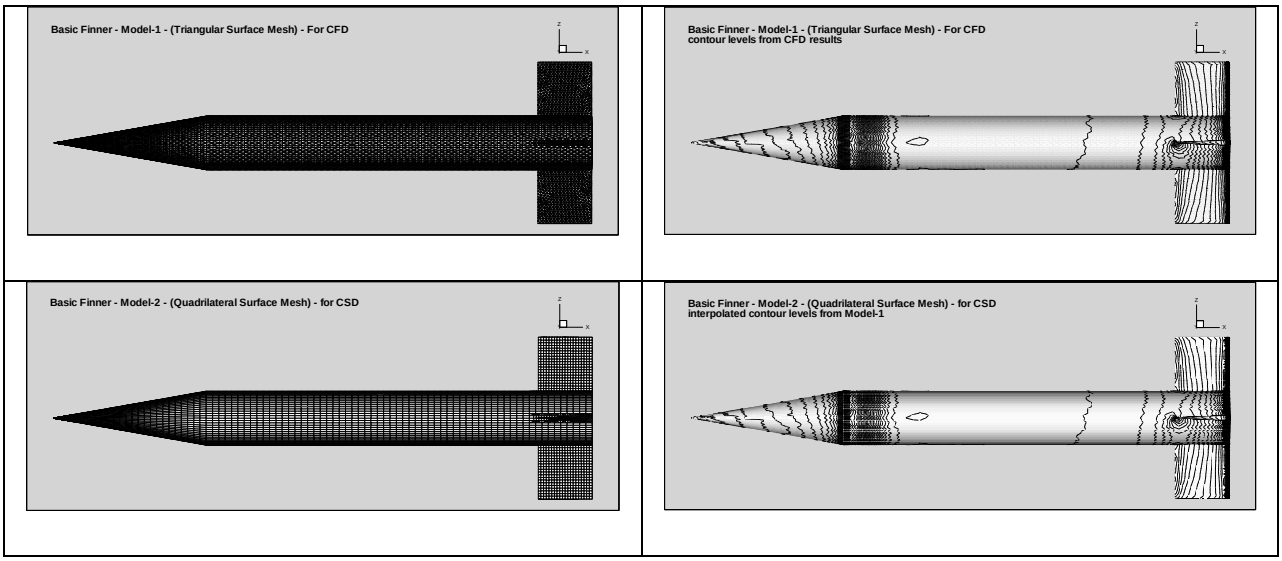


Figure 2.20 Application of AdtSearchIn to Non-matching Discrete Interfaces between Fluid and Structure Mesh of Basic Finner Rocket [25]

### *2.3.2 Spline Methods*

Computational aeroelasticty needs coupling of the aerodynamic force and structural response. Spline methods provide a spline matrix which relates the displacements of the structural grids to the aerodynamic grids. Once the spline matrix is generated, the force can be transferred from aerodynamic grids to the structural finite element grids by the transpose of the same spline matrix.

#### *2.3.2.1 Infinite Spline Method*

The Infinite spline method was firstly proposed by Harder and Desmarais [22], [20], which is based upon the small deflection equation of an infinite plate. Consider N discrete structural grid points $(x_i,y_i)$, for i=1,2,…,N lying within a 2-D domain. Vertical position of the deformed surface is defined at each grid points. Infinite plane spline method solves the partial differential equation of equilibrium for an infinite plate with uniform thickness. The deformation of the infinite plate satisfies the given deflection $w_i(x_i,y_i)$ at the N structural grid points. Once the partial differential equation is solved, the deflection at other points, for instance the aerodynamic points, on the plate can be determined [20].

The governing equation of an infinite plate with bending stiffness is:

$$D\nabla^4 W = q \tag{2.4}$$

where W is the plate deflection, D is the plate bending rigidity, and q is the distributed load on the plate. Introducing polar coordinates, $x = r\cos\theta, y = r\sin\theta$ so that $\nabla^4$ in polar coordinates is given by [20]:

$$\nabla^4 = \frac{1}{r}\frac{d}{dr}\left\{ r\frac{d}{dr}\left[ \frac{1}{r}\frac{d}{dr}\left( r\frac{dw}{dr} \right) \right] \right\} \tag{2.5}$$

Considering the deflection due to a point load P at the origin of the coordinate system, a solution of Eqn 2.4 can be written as [20]:

$$W(r) = A + Br^2 + \left( \frac{P}{16\pi D} \right) r^2 \ln r^2 \tag{2.6}$$

where A and B are the undetermined coefficients.

For N point loads at the given location $(x_i,y_i)$, for i=1,2,,…,N in the 2-D space, the total deflection can be obtained by superimposing the fundamental solution of Eqn 2.4 such that [20]:

$$W(x,y) = \sum_{i=1}^{N} \left( A_i + B_i r_i^2 + \lambda_i r_i^2 \ln r_i^2 \right) \tag{2.7}$$

where:

$$A_i,\ B_i,\ and\ \lambda_i = \frac{P_i}{16\pi D} \tag{2.8}$$

are undetermined coefficients,

and

$$r_i^2 = (x - x_i)^2 + (y - y_i)^2 \tag{2.9}$$

For the purpose of determining these undetermined coefficients one needs to use certain information about the solution. For large values of r, one obtains terms of order $r^2$, *r, 1, 1/r,* etc., along with terms of order $r^2 \ln r^2$, *r lnr, ln* $r^2$, etc. [20]:

$$W(r,\theta) = r^2 \ln r^2 \sum_{i=1}^{N} \lambda_i + r^2 \sum_{i=1}^{N} B_i - 2r \ln r^2 \sum_{i=1}^{N} \left(x_i \cos\theta + y_i \sin\theta\right)\lambda_i$$
$$- 2r \sum \left(x_i \cos\theta + y_i \sin\theta\right)\left(\lambda_i + B_i\right) + \ln r^2 \sum_{i=1}^{N} \left(x_i^2 - y_i^2\right)\lambda_i + \ldots \tag{2.10}$$

For removing the singularity at r=∞, coefficients of the terms of order $r^2$, $r^2 \ln r^2$, and *r ln* $r^2$ must vanish. This gives [20]:

$$\sum_{i=1}^{N} \lambda_i = 0 \tag{2.11}$$

$$\sum_{i=1}^{N} x_i \lambda_i = 0 \tag{2.12}$$

$$\sum_{i=1}^{N} y_i \lambda_i = 0 \tag{2.13}$$

$$\sum_{i=1}^{N} B_i = 0 \tag{2.14}$$

Here equation 2.11 can be recognized as the discrete force equilibrium equation that eliminates terms of order $r^2 \ln r^2$. Eqns 2.12 and 2.13 are discrete moment equilibrium equations and eliminate terms of order *r ln r*. Finally, Eqn 2.14 serves to eliminate terms of order $r^2$.

Linear deflection of the aerodynamic points occurs only if they are located far from the domain of the structural grid points. A solution to the general spline problem, formed by superimposing solutions of Eq 2.4, is given by [20]:

$$w(x,y) = a_0 + a_1 x + a_2 y + \sum_{i=1}^{N} K_i(x,y)\lambda_i \tag{2.15}$$

where :

$$K_i(x,y) = r_i^2 \ln r_i^2 \tag{2.16}$$

$$r_i^2 = (x - x_i)^2 + (y - y_i)^2 \tag{2.17}$$

where :

$$a_0 = \sum_{i=1}^{N} \left[ A_i + B_i (x_i^2 + y_i^2) \right] \tag{2.18}$$

$$a_1 = -2 \sum_{i=1}^{N} B_i x_i \tag{2.19}$$

$$a_2 = -2 \sum_{i=1}^{N} B_i y_i \tag{2.20}$$

N+3 unknowns in Eqn 2.15 can be determined from application of side conditions found in Eqns 2.11-2.14 along with setting the deflection at the i$^{th}$ point to its known value *W* [20].

$$W_i = a_0 + a_1 x_i + a_2 y_i + \sum_{i=1}^{N} K_{ij} \lambda_j \quad for\, i = 1,2,...,N \tag{2.21}$$

where :

$$K_{ij} = r_{ji}^2 \ln r_{ij}^2 \tag{2.22}$$

$$r_{ij}^2 = (x_i - x_j)^2 + (y_i - y_j)^2 \tag{2.23}$$

Equation 2.21 and the side conditions found in Eqn 2.11-2.14 can now be expressed in matrix form as [20]:

$$\{W\} = [R]\{a\} + [K_{ij}]\{\lambda\} \tag{2.24}$$

$$[R]^T \{\lambda\} = 0 \tag{2.25}$$

where:

$$\{W\} = \begin{Bmatrix} W_1 \\ W_2 \\ \cdot \\ \cdot \\ W_N \end{Bmatrix}, \quad \{\lambda\} = \begin{Bmatrix} \lambda_1 \\ \lambda_2 \\ \cdot \\ \cdot \\ \lambda_N \end{Bmatrix} \tag{2.26}$$

$$\{a\} = \begin{Bmatrix} a_0 \\ a_1 \\ a_2 \end{Bmatrix}, \quad \{R\} = \left[ \begin{Bmatrix} 1 \\ 1 \\ \cdot \\ \cdot \\ 1 \end{Bmatrix} \begin{Bmatrix} x_1 \\ x_2 \\ \cdot \\ \cdot \\ x_3 \end{Bmatrix} \begin{Bmatrix} y_1 \\ y_2 \\ \cdot \\ \cdot \\ y_3 \end{Bmatrix} \right] \tag{2.27}$$

Solving equations 2.24 and 2.25 for $\{\lambda\}$ and $\{a\}$ gives [21]:

$$\{\lambda\} = \left[ [K]^{-1} - [K]^{-1}[R]\left[[R]^T[K]^{-1}[R]\right]^{-1}[R]^T[K]^{-1} \right]\{W\} \tag{2.28}$$

$$\{a\} = \left[[R]^T[K]^{-1}[R]\right]^{-1}[R]^T[K]^{-1}\{W\} \tag{2.29}$$

Letting subscript ‘s’ represents the structural grid and subscript ‘a’ represents the aerodynamic grid, equation 2.29 can be written as:

$$\{W_a\} = [K_{as}]\{\lambda_s\} + [R_a]\{a_s\} \tag{2.30}$$

The transformation spline matrix $[S]$ is needed in the form:

$$\{W_a\} = [S]\{W_s\} \tag{2.31}$$

Therefore, $\{W_s\}$ can be factored out of equation 2.29 and the equations can be solved for $[S]$[21],

$$[S]=\begin{bmatrix}[K_{as}]\left[[K_s]^{-1}-[K_s]^{-1}[R_s]\left[[R_s]^T[K_s]^{-1}[R_s]\right]^{-1}[R_s]^T[K_s]^{-1}\right]+ \\ [R_a]\left[[R_s]^T[K_s]^{-1}[R_s]\right]^{-1}[R_s]^T[K_s]^{-1}\end{bmatrix} \tag{2.32}$$

The elements of $[K_{as}]$ and $[K_s]$are defined as:

$$K_{as\,ij}=r_{as_{ij}}^2\ln(r_{as_{ij}}^2) \tag{2.33}$$

$$K_{s\,ij}=r_{s_{ij}}^2\ln(r_{s_{ij}}^2) \tag{2.34}$$

where:

$$r_{as_{ij}}^2=(x_{a_i}-x_{s_j})^2+(y_{a_i}-y_{s_j})^2 \tag{2.35}$$

$$r_{s_{ij}}^2=(x_{s_i}-x_{s_j})^2+(y_{s_i}-y_{s_j})^2 \tag{2.36}$$

$[R_a]$ and $[R_s]$ are defined by equation 2.27. Displacements and coordinates of the aerodynamic grid points can be computed from displacements of the structural grid points with the following:

$$[\delta_a]=[S][\delta_s] \tag{2.37}$$

$$[q]=[q]_0+[\delta] \tag{2.38}$$

where $[q]_0$ is the original undeformed grid. The grid coordinate matrices are defined as:

$$[q]=\begin{bmatrix} q_{x1} & q_{y1} \\ q_{x2} & q_{y2} \\ \vdots & \vdots \\ q_{xN} & q_{yN} \end{bmatrix} \tag{2.39}$$

Transformation of the forces from the aerodynamic grid to the structural grid can be performed by the transpose of $[S]$. Eqn 2.39 ensures the conservative transfer of energy between the flow and the structural systems [28].

$$[F_s]=[S]^T[F_a] \tag{2.40}$$

where the force matrix is defined as:

$$[F]=\begin{bmatrix} F_{x1} & F_{y1} \\ F_{x2} & F_{y2} \\ \vdots & \vdots \\ F_{xN} & F_{yN} \end{bmatrix} \tag{2.41}$$

Aerodynamic grid, which is used in CFD calculations, is three-dimensional. In order to perform the infinite spline method, it is required that all structural grid points and aerodynamic grid points are located on the same plane. Therefore, aerodynamic grid points are projected to the spline plane on which the structural grid points lie, in order to create the $[R_a]$ matrix. For the infinite spline method, two or more than two structural grid points can not be located at the same *x* and *y* location. Another important is that for a given set of normal displacements at the structural grid points, the infinite spline method gives the displacements at the aerodynamic points only in the normal direction of the spline plane [20].

In Figure 2.21, splined out-of-plane deflection of the first mode from CSD grid to CFD grid using the spline matrix [S] is showed. The calculated force on the aerodynamic grid is similarly splined to the structural grid using the transverse of the same spline

matrix. Total force is calculated for both grids by summing up the forces on the aerodynamic grid and on the structural grid, respectively. Resulting total forces are the same for both grids. Also, moments about a point are same for both grids. It can be concluded that spline conserves the total force and moments on each system [21].

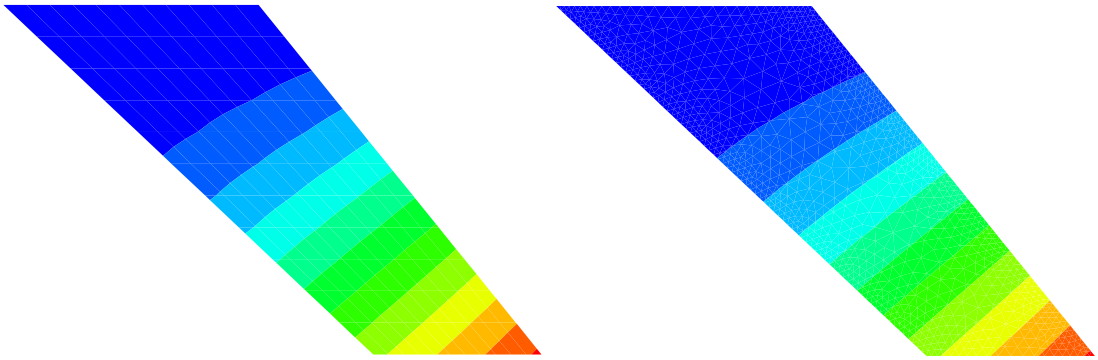

Figure 2.21 Out-of-Plane Deformation of the AGARD Wing 445.6 Splined from CSD (left) Grid to CFD (right) Grid (Infinite Spline Method)

#### *2.3.2.2 Thin Plate Spline Method*

Thin plate spline method is a three-dimensional implementation of the infinite-spline method. The derivation is entirely analogous with the infinite spline method with the addition of the third coordinate [20]. Equation 2.7 becomes:

$$W(x,y,z) = \sum_{i=1}^{N} \left( A_i + B_i r_i^2 + \lambda_i r_i^2 \ln r_i^2 \right) \tag{2.42}$$

where:

$$r_i^2 = (x - x_i)^2 + (y - y_i)^2 + (z - z_i)^2 \tag{2.43}$$

Boundary conditions at infinity are the same with those of infinite spline method except the additional moment in the third axis that is presented in the equations.

$$\sum_{i=1}^{N} \lambda_i = 0 \tag{2.44}$$

$$\sum_{i=1}^{N} x_i \lambda_i = 0 \tag{2.45}$$

$$\sum_{i=1}^{N} y_i \lambda_i = 0 \tag{2.46}$$

$$\sum_{i=1}^{N} z_i \lambda_i = 0 \tag{2.47}$$

$$\sum_{i=1}^{N} B_i = 0 \tag{2.48}$$

Applying boundary conditions to eliminate the terms of order $r^2$, $r^2 \ln r^2$, and $r \ln r^2$, gives [20]:

$$w(x, y, z) = a_0 + a_1 x + a_2 y + a_3 z + \sum_{i=1}^{N} K_i(x, y, z) \lambda_i \tag{2.49}$$

where:

$$K_i(x, y, z) = r_i^2 \ln r_i^2 \tag{2.50}$$

Eqns 2.49 and 2.44-48 can be expressed in matrix form:

$$\{W\} = [R]\{a\} + [K_{ij}]\{\lambda\} \tag{2.51}$$

$$\left[R\right]^T\left\{\lambda\right\}=0 \tag{2.52}$$

where:

$$\left\{W\right\}=\begin{Bmatrix} W_1 \\ W_2 \\ \vdots \\ W_N \end{Bmatrix},\ \left\{\lambda\right\}=\begin{Bmatrix} \lambda_1 \\ \lambda_2 \\ \vdots \\ \lambda_N \end{Bmatrix} \tag{2.53}$$

$$\left\{a\right\}=\begin{Bmatrix} a_0 \\ a_1 \\ a_2 \\ a_3 \end{Bmatrix},\quad \left\{R\right\}=\begin{bmatrix} \begin{Bmatrix} 1 \\ 1 \\ \vdots \\ 1 \end{Bmatrix} & \begin{Bmatrix} x_1 \\ x_2 \\ \vdots \\ x_3 \end{Bmatrix} & \begin{Bmatrix} y_1 \\ y_2 \\ \vdots \\ y_3 \end{Bmatrix} & \begin{Bmatrix} z_1 \\ z_2 \\ \vdots \\ z_3 \end{Bmatrix} \end{bmatrix} \tag{2.54}$$

The remaining equations are exactly the same as formulated in infinite spline method. Once the spline transformation matrix $\left[S\right]$ is generated, displacements and coordinates of the displaced aerodynamic grid can be computed from displacements of the structural grid with the Eqns 2.37 and 2.38. Transformation of the forces from the aerodynamic grid to the structural grid can be performed by using Eqn 2.40.

In order to perform interpolation of displacements at 3-D structural grid points, there is no requirement of spline plane. It is not required that all structural grid points and aerodynamic grid points are located on the same plane. For the thin spline method, two or more than two structural grid points can not be located at the location and structural grid points can not be on the same plane. [20]. In Figure 2.22, an example of splined z-direction displacement values of a generic missile body from CSD grid to CFD grid using the spline matrix [S] is showed.

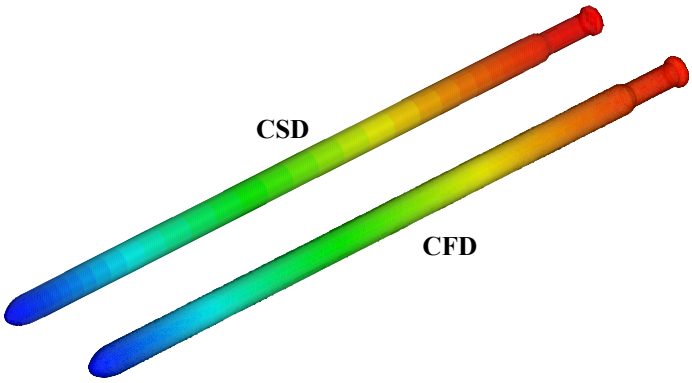


Figure 2.22 z-direction Displacement Values of the Slender Missile Body Splined from CSD Grid to CFD Grid (Thin Plate Spline Method)

## *2.4 FLOW SOLVER - FLUENT*

FLUENT being a commercial computer program for modeling fluid flow and heat transfer for complex geometries, offers general-purpose CFD software for a wide range of industrial applications including highly automated, specific packages [6].

FLUENT offers complete flexibility in analyses owing to its capability, in solution of flow problems, to integrate unstructured meshes which can be created easily in complex geometries. It is a useful tool both in 2-D and 3-D analyses in which various types of meshes are utilized such as 2-D triangular / quadrilateral, 3-D tetrahedral / hexahedral / pyramidal / wedge-shaped or a combination of various polyhedral meshes at the same time in hybrid form.

FLUENT also allows refining or coarsening the grid which is based on the gradient of the flow variables. FLUENT is written in C language providing the programmer and the user with the full flexibility and the control of true dynamic memory allocation, efficient data structure and a rich library of routines.

Furthermore, FLUENT may be run on powerful computer workstations as a separate simultaneous process. The client/server architecture offers interactive control, efficient execution and complete flexibility between various types of machines or operating systems. In this part, the fundamental transport equations and numerical methods which are used to solve the governing equations in FLUENT are introduced.

FLUENT uses finite volume method in which the transport equations are written in integral form and the integral form of the governing equations are solved for each finite volume cell within the domain. The flux values at the cell surfaces are calculated using surface integrals by applying the discretization. The discretized system of equations are linearized and solved by using Gauss-Seidel method which requires less CPU memory and is faster than that used in direct solution method [6].

User has an option to select between the numerical methods: pressure-based and density based. Formerly, the pressure based method was used for low speed flows, while the density based method was mainly developed for high speed flows. Recently, both methods have been extended and reformulated to solve for a wide range of flow regimes. In both methods, the momentum equations are used to obtain the velocity field.

In the density based method, the density field is obtained from continuity equation while pressure field is obtained from the equation of state. In the case of the pressure based method, the pressure field is obtained by solving a pressure or pressure correction equation which is obtained by using continuity and momentum equations in such a way that the velocity field is corrected by the pressure and continuity is preserved [6].

FLUENT solves the governing integral equations for the conservation of mass, momentum, energy and other scalars such as turbulence. The pressure based method linearizes the governing equations and solves the flow variables implicitly. In the density based method, system of equations (continuity, momentum and energy) can be solved simultaneously using either implicit or explicit formulation. Iteration steps are illustrated in Figure 2.23. Several iterations are performed before the solution is convergent as the governing equations are nonlinear and coupled together.

Continuity:
$$\frac{\partial}{\partial t}\int_{\Omega}\rho\, d\Omega + \oint_{\partial\Omega}\rho\left(\vec{v}.\vec{n}\right)dS = 0 \tag{2.55}$$

Momentum:
$$\frac{\partial}{\partial t}\int_{\Omega}\rho\vec{v}\, d\Omega + \oint_{\partial\Omega}\rho\vec{v}\left(\vec{v}.\vec{n}\right)dS = \int_{\Omega}\rho\vec{f}_e\, d\Omega - \oint_{\partial\Omega}\rho\vec{n}\, dS + \oint_{\partial\Omega}\left(\bar{\bar{\tau}}.\vec{n}\right)dS \tag{2.56}$$

Energy:
$$\frac{\partial}{\partial t}\int_{\Omega}\rho E\, d\Omega + \oint_{\partial\Omega}\rho H\left(\vec{v}.\vec{n}\right)dS = \int_{\Omega}\left(\rho\vec{f}_e.\vec{v} + \dot{q}_h\right)d\Omega + \oint_{\partial\Omega}\kappa\left(\nabla T.\vec{n}\right)dS + \oint_{\partial\Omega}\left(\bar{\bar{\tau}}.\vec{v}\right).\vec{n}dS \tag{2.57}$$

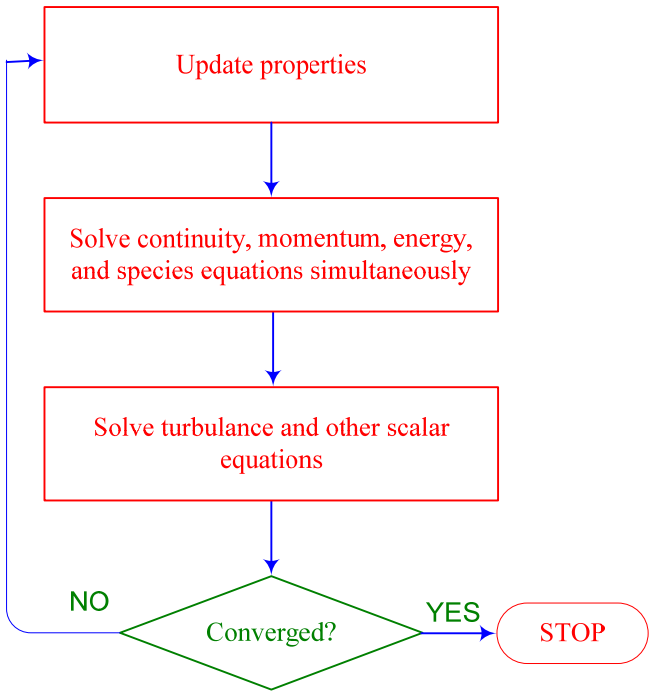


Figure 2.23 Overview of the Density Based Solution Method [6]

Two pressure based solver algorithms are available in FLUENT: a segregated algorithm, and a coupled algorithm.

### *The Pressure-Based Segregated Algorithm*

The pressure based algorithm uses a solution algorithm where the governing equations are solved sequentially. Because the governing equations are coupled and nonlinear, the solution must be carried out iteratively to obtain a converged numerical solution.

The governing equations are solved in a decoupled manner in pressure based segregated algorithm. Since equations are stored in the memory one at a time, the segregated algorithm uses the memory efficiently, but solution convergence is relatively slow [6]. Iteration steps which are used in segregated algorithm are illustrated in Figure 2.24.

### *The Pressure-Based Coupled Algorithm*

The pressure based coupled algorithm comprise the momentum equations and the pressure based continuity equations in order to solve the coupled system of equations. The rate of solution convergence significantly improves as compared to the segregated algorithm because of the closely coupled manner which is used to solve the momentum and continuity equations. The system of all equations is stored in the memory during the solution of velocity and pressure fields rather than just a single equation, as in the case with the pressure based segregated algorithm. Thus, the memory requirement increases by 1.5 or 2 times that of the segregated algorithm [6].

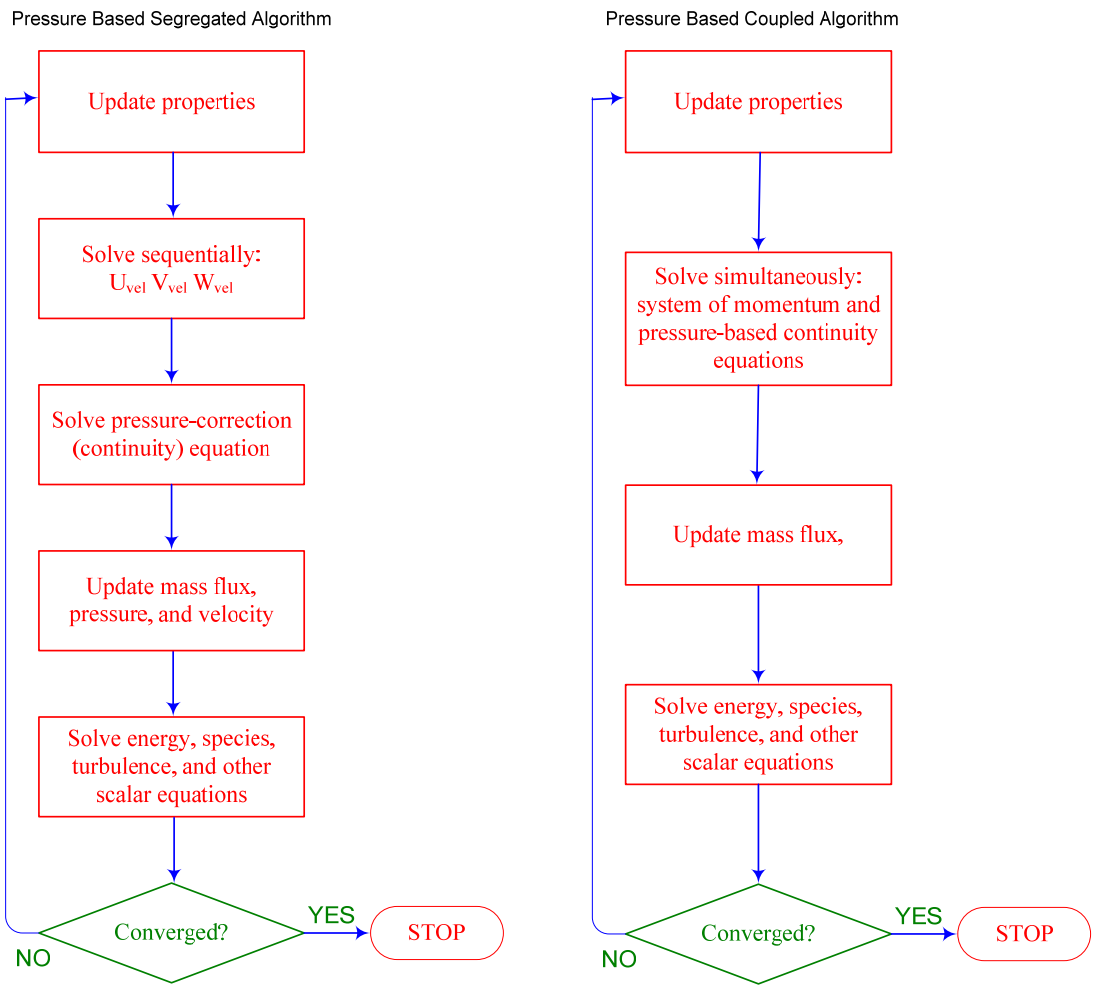


Figure 2.24 Overview of the Pressure-Based Solution Method [6]

### *Pressure-Velocity Coupling*

The Pressure-Implicit with Splitting of Operators (PISO), pressure velocity coupling scheme is based on the higher degree of the approximate relation between the corrections for velocity and pressure. The PISO algorithm requires high CPU time per iteration, but it impressively decreases the number of iterations which is required for convergence. Thus, PISO algorithm is commonly used for transient problems [6].

PISO divides the pressure correction scheme into predictor and corrector steps. In the first step, velocity field is predicted by using the momentum equation which does not necessarily satisfy the continuity equation. Thus, a corrector step is used to calculate pressure field which is used to recalculate velocity field that satisfies the continuity equation. For a given time step, equations are solved iteratively until the convergence criteria is met. Therefore, advancing the solutions by one time step needs outer iterations as shown in Figure 2.25. PISO algorithm is used to obtain time accurate solutions without changing physical time step which is used for advancing the solution.

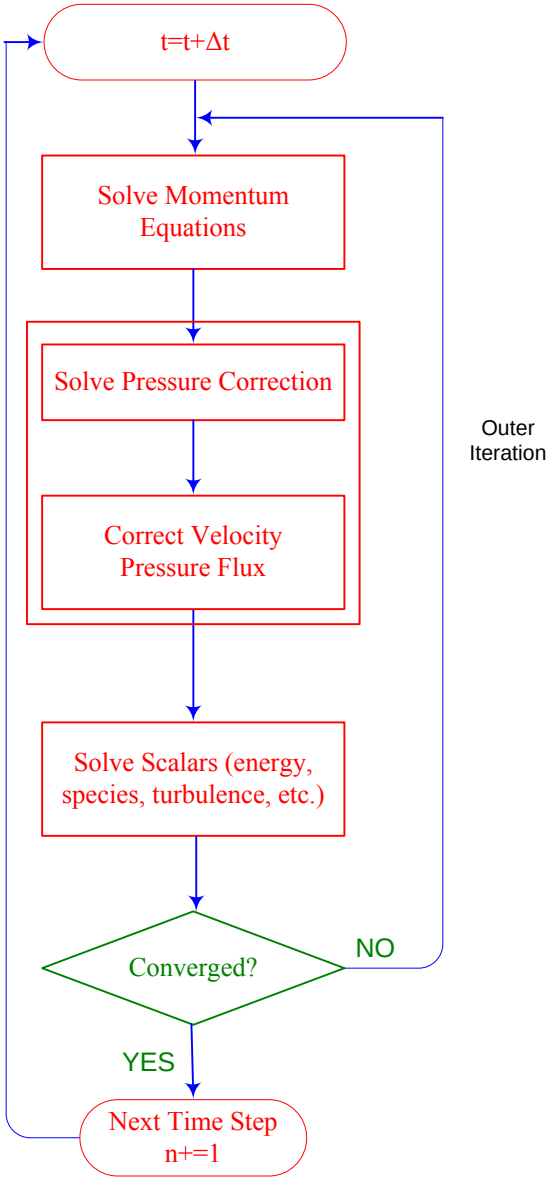


Figure 2.25 Overview of the Iterative Time Advancement Solution Method for the Pressure Based Solver [6]

## *2.5 STRUCTURAL SOLVER - MSC/NASTRAN*

MSC/NASTRAN is a commercial finite element analysis program which consists of several modules designed for specific tasks such as processing model geometry, assembling matrices, applying constraints, solving matrix problems, calculating output quantities, conversing with the database, and printing the solution. It is commonly used in the industry for the analysis of stress, structural failure, vibration, structural durability, heat transfer, flutter and aeroelasticity.

In this study, linear static analysis (101) is used for static aeroelastic analysis and Modal analysis (103) is performed to determine mode shapes and corresponding natural frequencies which are used as input for dynamic aeroelastic analyses.

Figure 2.26 shows the basic steps that MSC/NASTRAN follows when solving a linear statics analysis.

In static analysis, adequate boundary conditions must be applied to the model in order to prevent any rigid body motion of the structure. If the specified boundary conditions do not adequately constrain the model in all directions, the structure's stiffness matrix remains singular and the run terminates with an error message. Once the boundary conditions are applied to the model appropriately, the global stiffness matrix is reduced to a nonsingular stiffness matrix representing the constrained structure. All of the loads that are applied to the model are combined to form the load vector. These applied loads can be in the form of point forces and moments applied directly to the grid points, line loads applied along the length of one-dimensional elements, surface loads applied to two- and three-dimensional elements, or body loads such as gravity. These different load types may be combined to form a single load vector, which is the same as saying that the loads are applied simultaneously. There is also the option of applying multiple load vectors within a single run. After the constrained stiffness matrix and the load vector are

generated, the static equilibrium matrix equation given by Eqn 2.58 is solved as follows [45]:

$$[K]\{u\} = \{p\} \tag{2.58}$$

where;

$[K]$ = system stiffness

$\{u\}$ = grid point displacements

$\{p\}$ = applied load vector

The unknowns in Eqn 2.58 are the displacements at the grid points in the model. Determining the displacements involves the equivalent of inverting the stiffness matrix and multiplying it by the force vector. Actually, the process of inverting a matrix is too time consuming; therefore, a process based on the Gauss elimination method is used. Once the displacements at the grid points are known, any desired outputs, such as element forces, strains, and stresses, are computed using those displacements on an element-by-element basis. It can be controlled what type of output is generated and whether the output is printed, punched to a file, or plotted [45].

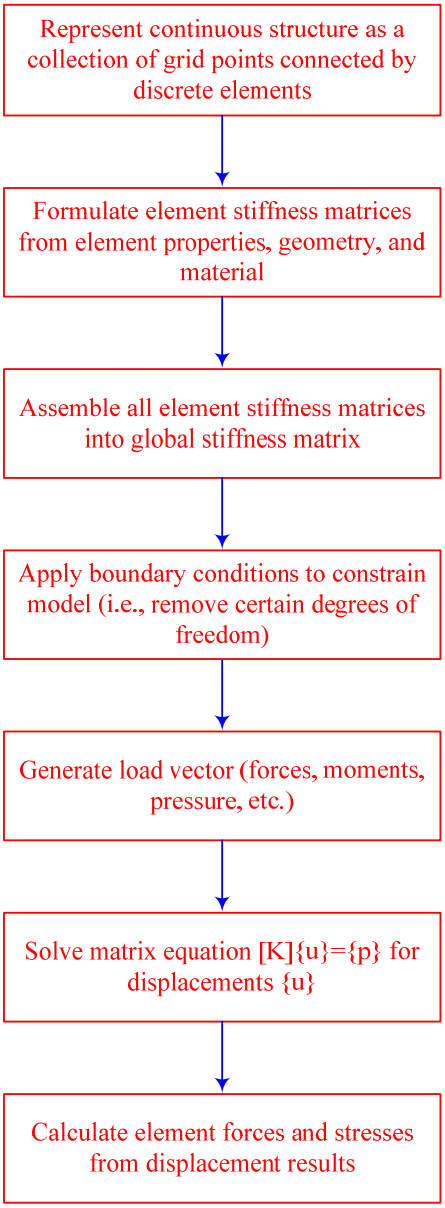


Figure 2.26 Linear Static Analysis in MSC. NASTRAN [45]

The usual first step in performing the dynamic analysis is determining the mode shapes and the natural frequencies without damping. These results show the dynamic behavior of the structure and indicate how the structure will respond to dynamic loading [46]. The natural frequencies represent the neutral tendency of the structure to vibrate when it is

subjected to a disturbance. Computation of the natural frequencies and mode shapes is performed by solving an eigenvalue problem. Each mode shape is associated with a specific natural frequency.

The equation of motion for normal modes and natural frequencies are solved by using a special reduced form of the equation, assuming no applied loading and damping. The reduced form of the equation of motion can be shown in matrix form as follows:

$$[M]\{\ddot{u}\} + [K]\{u\} = 0 \tag{2.59}$$

This is the equation of motion for undamped free vibration. To solve Eqn 2.59, it is assumed a harmonic solution of the form:

$$\{u\} = \{\phi\}\sin \omega t \tag{2.60}$$

where:

$\phi$ :eigenvector or mode shape

$\omega$ : natural frequency

If differentiation of the assumed harmonic solution is performed and substituted into the equation of motion, the following is obtained:

$$\left([K] - \omega^2 [M]\right)\{\phi\} = 0 \tag{2.61}$$

This equation is called the eigen equation, which is a set of homogeneous algebraic equations for the components of the eigenvector and forms the basis for the eigenvalue problem.

The determinant is zero only at a set of discrete eigenvalues $\lambda_i$ or $\omega_i^2$. There is an eigenvector which satisfies Eqn 2.61 and corresponds to each eigenvalue. Therefore, Eqn 2.61 can be rewritten as:

$$\left([K]-\omega_i^2[M]\right)\{\phi_i\}=0 \ , \quad i = 1,2,3... \tag{2.62}$$

Each eigenvalue and eigenvector define a free vibration mode of the structure. The $i^{th}$ eigenvalue $\lambda_i$ is related to the $i^{th}$ natural frequency as:

$f_i = \dfrac{\omega_i}{2\pi}$ , $i^{th}$ natural frequency

$\omega_i = \sqrt{\lambda_i}$

The number of eigenvectors and eigenvectors is equal to the number of degrees-of-freedom. In addition, a natural mode of the structure can be represented by using its generalized mass and generalized stiffness. An important characteristic of normal modes is that the scaling or magnitude of the eigenvectors is arbitrary. Mode shapes are fundamental characteristic shapes of the structure and are therefore relative quantities. In the solution of the equation of motion, the form of the solution is represented as a shape with time-varying amplitude. Therefore, the basic mode shape of the structure does not change while it is vibrating; only its amplitude changes [46].

***Mode Shape Normalization***

Although the scaling of normal modes is arbitrary, for practical considerations mode shapes should be scaled (i.e., normalized) by a chosen convention. In MSC/NASTRAN, there are three normalization choices, MASS, MAX, and POINT normalization [46].

MASS normalization scales each eigenvector to result in a unit value of generalized mass.

$$\{\phi_j\}^T [M]\{\phi_j\} = 1.0 \tag{2.63}$$

By using this method, a modal mass matrix becomes an identity matrix and since it decreases the requirements of the computational data storage, mass normalization approach is appropriate for modal dynamic response analyses.

In MAX normalization, each eigenvector is normalized with respect to the largest a-set component. This normalization results in the largest a-set displacement value being set to a unit value. This normalization approach can be very useful in the determination of the relative participation of an individual mode.

POINT normalization of eigenvectors allows choosing a specific displacement component at which the modal displacement is set to 1 or -1.

***Inertia Relief***

MSC/NASTRAN provides an advanced option, inertia relief, which allows simulating unconstrained structures in a static analysis. In static analysis by finite element method, model is assumed to have no mechanism and not to move as a rigid body. The stiffness matrix becomes singular if any of these conditions exists in a conventional finite element analysis. Decomposition of a singular matrix in MSC/NASTRAN leads to unreasonable answers or a fatal message. As a result, conventional finite element static analysis cannot be performed on unconstrained structures. However, MSC/NASTRAN provides a method, inertia relief, in order to analyze these conditions [45]. By using inertia relief method, the inertia of the structure is used to resist the applied loadings assuming that the structure is in state of static equilibrium even though it is not constrained. A spacecraft in orbit or an aircraft in flight are two examples of these

conditions. In these cases, although the structure is capable of unconstrained motion, it is in state of static equilibrium.

### *2.6 STRUCTURAL MODAL APPROACH*

Aeroelastic simulation consisting of non-linear CFD analysis coupled to a dynamic structural model is performed in order to investigate the structural deformation under an unsteady aerodynamic loading. This method allows time-accurate non-linear analysis of dynamic behavior, leading to much more accurate investigation of flutter [24]. The majority of such methods rely on the prediction of structural response by a summation of limited number of modes derived from modal analysis using a commercial finite element solver.

The governing equation of motion of a structure can be written as:

$$[M]\frac{d^2w}{dt^2} + [C]\frac{dw}{dt} + [K]w = \{F(t)\} \tag{2.64}$$

where

w: Displacement vector,

$[C]$: Damping matrix,

$[K]$: Stiffness matrix,

$[M]$: Mass matrix,

F(t): Vector of forces exerted on the nodes of the structure

$$w = \begin{pmatrix} w_1 \\ w_i \\ \cdot \\ \cdot \\ w_N \end{pmatrix} \qquad F = \begin{pmatrix} F_1 \\ F_i \\ \cdot \\ \cdot \\ F_N \end{pmatrix} \tag{2.65}$$

where $N$ is the total number of the structural node. $w_i$ and $F_i$ are expressed as:

$$w_i = \begin{pmatrix} w_{ix} & w_{iy} & w_{iz} \end{pmatrix} \tag{2.66}$$

$$F_i = \begin{pmatrix} F_{ix} & F_{iy} & F_{iz} \end{pmatrix} \tag{2.67}$$

The displacement and force vectors at node point $i$, have three components in 3-D space. Using modal analysis, the dependent variables are expanded in terms of the natural free vibration modes as:

$$\{w(x,y,z,t)\} = \sum_{i=1}^{N} q_i(t)\{\phi_i(x,y,z)\} \tag{2.68}$$

where $q_i(t)$ and $\{\phi_i(x,y,z)\}$ are the generalized displacement vector and mode shape matrix, respectively. The mode shape matrices are obtained by solving for the eigenvalues of the free vibration problem. The modal decomposition of the structure motion is expressed as:

$$K\phi = M\phi\Lambda \tag{2.69}$$

or

$$K\phi_j = \lambda_j M\phi_j \tag{2.70}$$

A finite element structural solver may be used to solve Eqn 2.69 and obtain the mode shapes. Modal matrix and eigenvalue matrix $\Lambda$ is expressed as:

$$\phi = [\phi_1, ..., \phi_i, ..., \phi_{3N}] \tag{2.71}$$

$$\Lambda = diag[\lambda_1, ..., \lambda_i, ..., \lambda_{3N}] \tag{2.72}$$

j[th] eigenvalue can be defined by the natural frequency ($\omega$) as:

$$\lambda_j = \omega_j^2 \tag{2.73}$$

Mode shape matrix is normalized with respect to the mass matrix and substituting Eqn 2.73 into Eqn 2.70 and then multiplying by $\phi^T$ yields:

$$\ddot{q} + [\xi]\dot{q} + [\omega]q = Q \tag{2.74}$$

where

$$[\xi] = \phi^T [C] \phi \tag{2.75}$$

$$[\omega] = \phi^T [K] \phi \tag{2.76}$$

$$Q = \phi^T [F] \tag{2.77}$$

$[\omega]$ and $[\xi]$ matrices are diagonal and their terms are $\omega_i$ and $2\xi_i\omega_i$, respectively. $Q$ is the generalized unsteady aerodynamic forces. The coupled system of equation can be rewritten as:

$$\ddot{q}_i + 2\xi_i\omega_i\dot{q}_i + \omega_i q_i = Q_i, \quad i=1,2,...,N \tag{2.78}$$

where $\xi_i$ and $\omega_i$ are the modal damping and the natural frequency for the i[th] mode, respectively. In this initial value problem, Newmark algorithm [21] is used to solve Eqn 2.78 for $q_{i,n+1}$ with the following set of equations:

$$\left(1+\beta\Delta t^2\omega_i^2\right)\{\ddot{q}\}_{n+1}=\{Q\}_{n+1}-\omega_i^2\left(\{q\}_n+\Delta t\{\dot{q}\}_n+\frac{\Delta t^2}{2}(1-2\beta)\{\ddot{q}\}_n\right) \tag{2.79}$$

$$\{\dot{q}\}_{n+1}=\{\dot{q}\}_n+\Delta t\left((1-\gamma)\{\ddot{q}\}_n+\gamma\{\ddot{q}\}_{n+1}\right) \tag{2.80}$$

$$\{q\}_{n+1}=\{q\}_n+\Delta t\{\dot{q}\}_n\frac{\Delta t^2}{2}\left((1-2\beta)\{\ddot{q}\}_n-2\beta\{\ddot{q}\}_{n+1}\right) \tag{2.81}$$

If $\gamma=\frac{1}{2}$, this implicit method is second order accurate. This method is stable if $\Delta t=\frac{\Omega}{\omega}$, where $\omega$ is the maximum natural frequency. If a linear acceleration is assumed, $\beta=\frac{1}{6}$ and $\Omega=3.464$ [21]. Assuming a linear acceleration and no structural damping, Eqns 2.79-2.81 simplify to:

$$\left(1+\frac{\Delta t^2}{6}\omega_i^2\right)\{\ddot{q}\}_{n+1}=\{Q\}_{n+1}-\omega_i^2\left(\{q\}_n+\Delta t\{\dot{q}\}_n+\frac{\Delta t}{3}\{\ddot{q}\}_n\right) \tag{2.82}$$

$$\{\dot{q}\}_{n+1}=\{\dot{q}\}_n+\frac{\Delta t}{2}\left(\{\ddot{q}\}_n+\{\ddot{q}\}_{n+1}\right) \tag{2.83}$$

$$\{q\}_{n+1}=\{q\}_n+\Delta t\{\dot{q}\}_n\frac{\Delta t^2}{6}\left(2\{\ddot{q}\}_n+\{\ddot{q}\}_{n+1}\right) \tag{2.84}$$

where $n$ is the time step.

## *2.7 STATIC AEROELASTICITY*

To conduct static aeroelastic analysis, CFD solver, FLUENT is coupled with finite element structural solver MSC/NASTRAN. To achieve this, a code is developed in FORTRAN language to automate the entire procedure. The overall computational aeroeastic procedure developed for static aeroelastic analysis may be divided into the following steps.

### *Static Aeroelastic Analysis Computational Procedure*

1. Geometry construction, mesh generation, application of appropriate boundary conditions, initializing the solution.

2. Steady state CFD analysis to calculate aerodynamic forces on the structure.

3. Interpolation of forces onto the structural mesh.

4. Structural finite element analysis to calculate displacements of the structure.

5. Interpolation of the displacements onto the aerodynamic surface mesh.

6. Mesh deformation according to the displacements obtained from the CSD calculations.

7. Repeat steps 2-6 until difference of structural displacements between two consecutive iterations is less than prescribed tolerance

The flow chart of the iterative procedure is given in Figure 2.27.

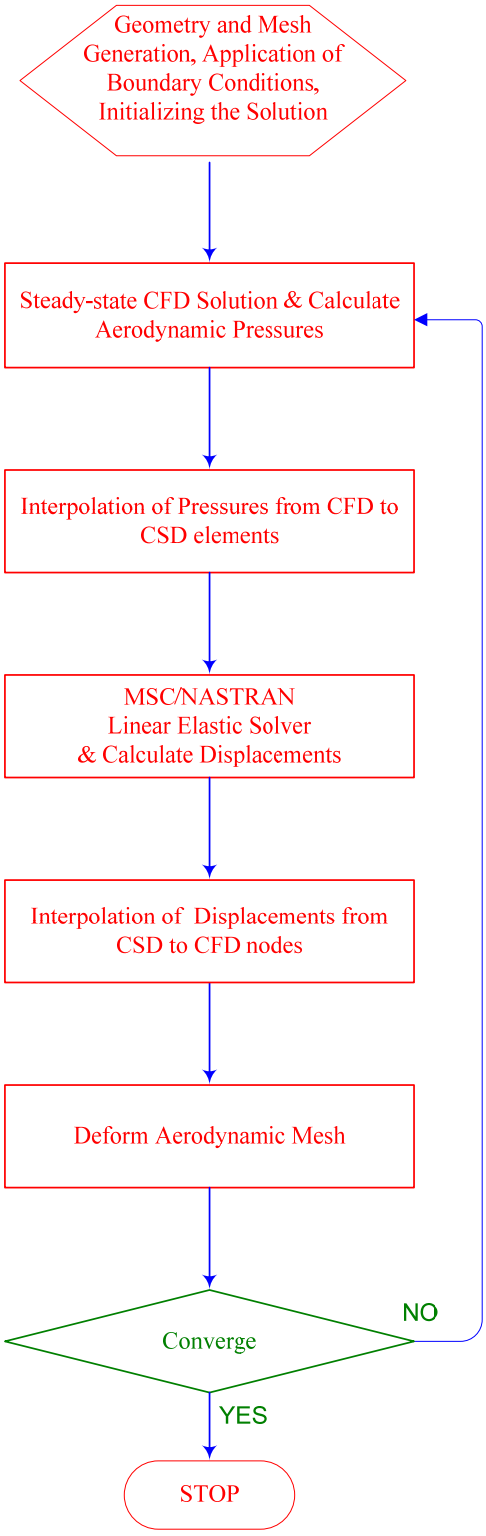


Figure 2.27 Flow Chart of the Static Aeroelastic Procedure

## *2.8 DYNAMIC AEROELASTICITY*

For the dynamic aeroelastic analysis, CFD solver, FLUENT is coupled to governing equations of motion of the structure that are presented in modal coordinates. Mode shapes and corresponding natural frequencies are obtained by using MSC/NASTRAN and used as input for this approach. A FORTRAN code is developed in order to perform the entire computational procedure which is developed for dynamic analysis and divided into the following major steps.

1. Geometry construction, mesh generation, application of appropriate boundary conditions, initializing the solution.

2. Steady state CFD analysis for the undeformed structure which is used as the starting point of the dynamic aeroelastic computations.

3. Unsteady CFD computations to calculate aerodynamic loads on the structure.

4. Spline pressure forces from aerodynamic cell centered points to the structural grid nodes.

5. Solve linear modal structural model in order to calculate the displacements of the structure by using mode shapes and natural frequencies as input.

6. Structural displacements are splined to the aerodynamic grid nodes.

7. Mesh deformation according to the obtained displacements.

8. Repeat steps 3-7 using current solution for the following steps until a specified flow time is reached.

The flow chart of the iterative procedure is given in Figure 2.28.

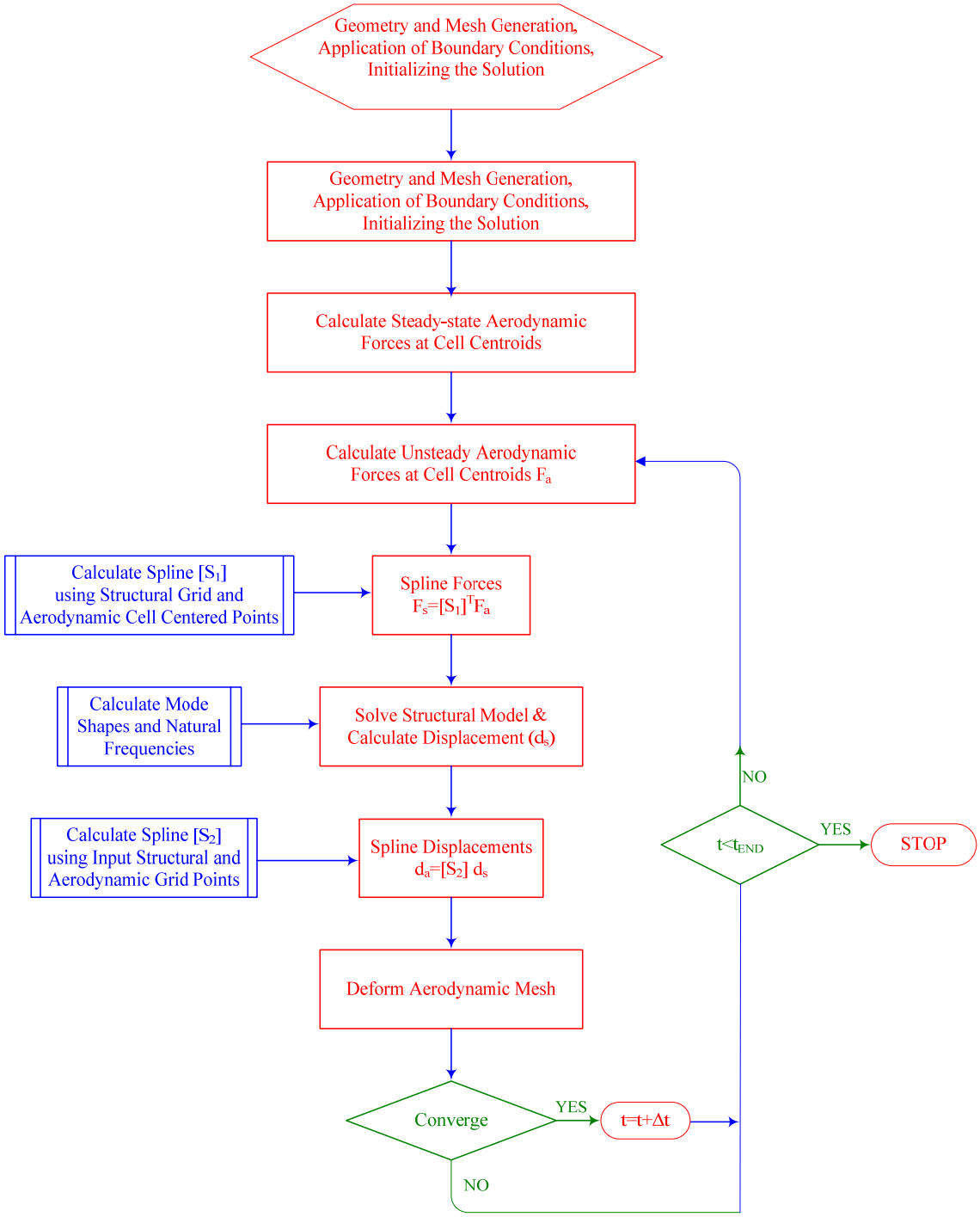


Figure 2.28 Flow Chart of the Dynamic Aeroelastic Procedure

# CHAPTER 3

# TEST CASES

## *3.1 TEST CASE 1 - AGARD WING 445.6*

### *3.1.1 INTRODUCTION*

In this chapter, present method is applied to solve static and dynamic aeroelastic characteristics of AGARD Wing 445.6, which is a well known test case for aeroelastic problems. Wind tunnel experiments have been conducted on AGARD Wing 445.6 in order to predict the dynamic response characteristics and the flutter boundary in the Langley Transonic Dynamics Tunnel [1].

The AGARD 445.6 Wing has taper ratio of 0.66, aspect ratio of 1.65 and wing swept of 45° at the quarter chord. It has root and tip chords of 0.558m and 0.368m, and a semi span of 0.762m. The airfoil section in the stream-wise direction is a NACA 65A004 airfoil, which is a symmetric airfoil with a maximum thickness of 4 % of the local chord. The wing planform is shown in Figure 3.1.

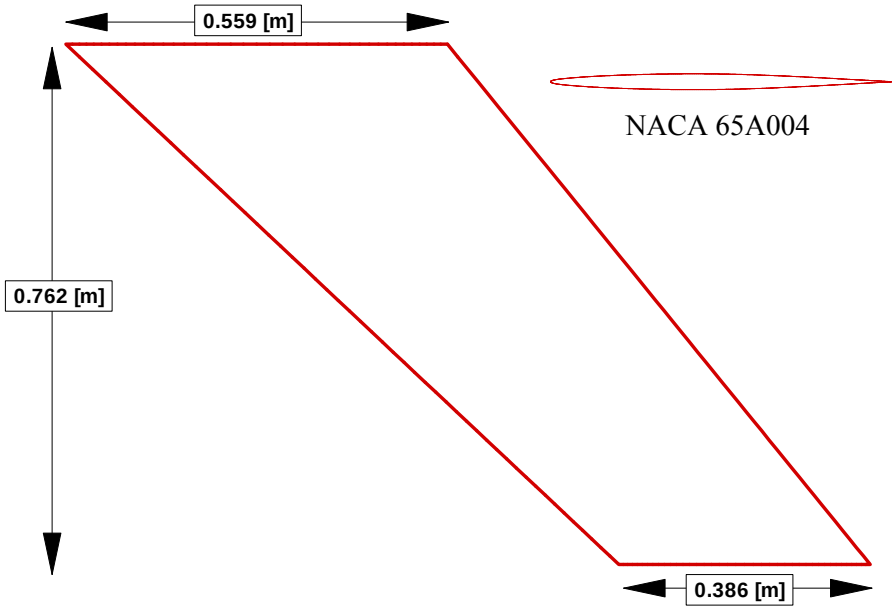


Figure 3.1 AGARD Wing 445.6 Planform

AGARD Wing 445.6 which was used in an experimental study [1] was constructed by laminated mahogany, which can be assumed as an orthotropic material of which material properties are unique and independent in three dimensional. The solid model of the wing which is tested in wind tunnel is shown in Figure 3.2.

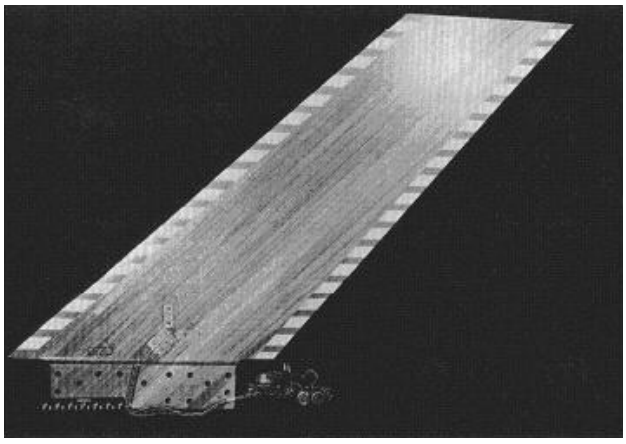

Figure 3.2 Solid Model of AGARD Wing 445.6 Used in Wind Tunnel Test [1]

The AGARD Wing 445.6 had holes drilled on it to make it weaker and to reduce the structural stiffness to obtain flutter at the test mach numbers in the wind tunnel experiments. In order to maintain the correct aerodynamic shape, holes were filled with rigid foam plastic. This weakened model is shown in Figure 3.3. The material properties for weakened AGARD wing was taken from model parameters in the aeroelastic optimization study by Kolonay [2] and shown in Table 3.1. In the present study, weakened model will be used to validate developed procedure for static and dynamic aeroelastic problems.

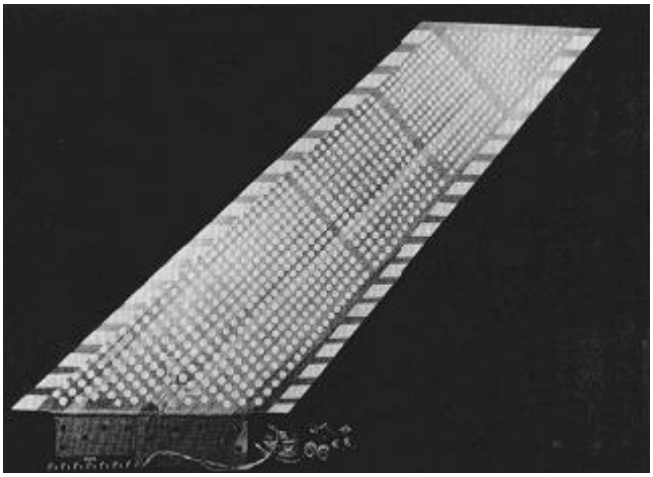

Figure 3.3 Weakened model of AGARD Wing 445.6 used in wind tunnel test [1]

Table 3.1 Mechanical Properties for the Weakened AGARD Wing 445.6

| **Material Property** | **Value [Gpa]** |
|---|---|
| $E_1$ | 3.1511 |
| $E_2$ | 0.4162 |
| G | 0.4392 |
| **Material Property** | **Value [kg/m$^3$]** |
| $\rho$ | 381.98 |
| **Material Property** | **Value** |
| $\nu$ | 0.31 |

$E_1$ and $E_2$ are the modulus of elasticity in the longitudinal and lateral directions, ν is Poisson's ratio, G is the shear modulus in each plane and ρ is the wing density.

### *3.1.2 AGARD WING 445.6 CFD ANALYSIS*

#### *3.1.2.1 Grid Sensitivity Study*

In this part, the details of the Computational Fluid Dynamics grids and the results of the rigid wing analyses are given. For grid sensitivity analysis, four unstructured grids with varying surface and volume densities are examined. These four different grids are tested in different flow conditions in order to determine minimum grid size which captures the physics of the flow. Coarse and medium grids have the minimum number of surface triangular elements. Medium grid has more tetrahedral cells than coarse grid. Fine and very fine grids have finest surface resolution and very fine grid has maximum number of tetrahedral cells. In this study, CFD analyses are performed for the flow conditions shown in Table 3.2.

Table 3.2 Free stream Flow Conditions for the Grid Sensitivity Study

| **Mach** | **α [°]** |
|---|---|
| 0.499 | 0 |
| 0.85 | 5 |
| 0.960 | 0 |
| 1.141 | 0 |

The dimensions of computational domain are given in Figure 3.4. The isometric view of the half cylinder computational domain and defined boundary conditions are shown in Figure 3.5. Aerodynamic surface is defined as wall boundary conditions. Flow conditions such as Mach number, operating pressure, temperature and angle of attack are defined in far-field boundary condition.

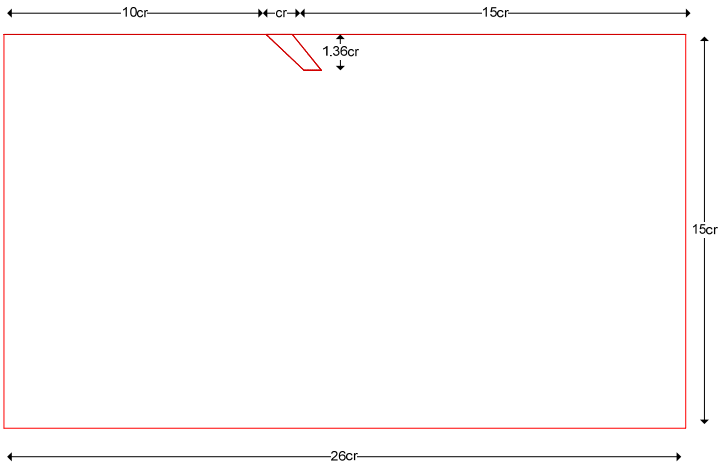


Figure 3.4 Dimensions of the Computational Fluid Dynamics Domain

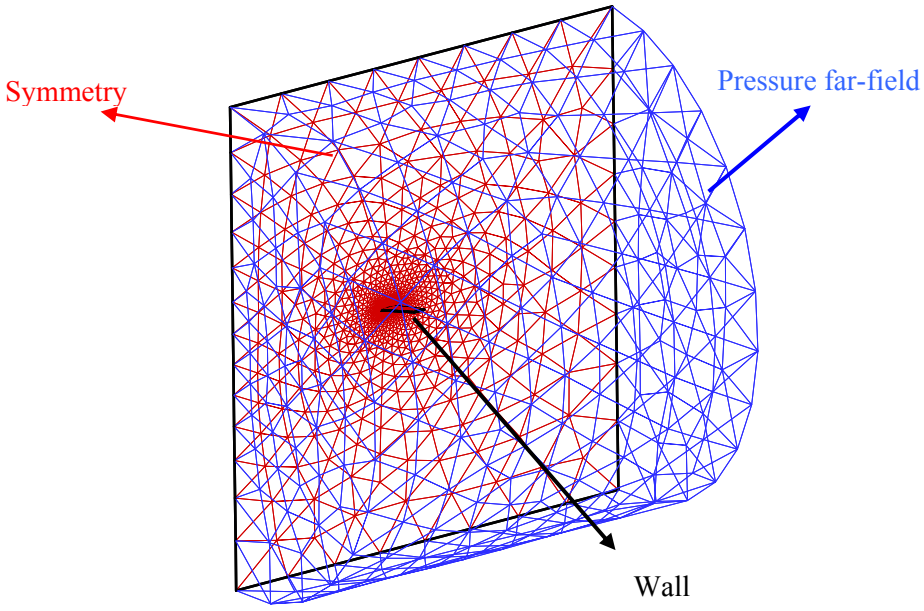


Figure 3.5 Half Cylinder Computational Fluid Dynamics Domain

The surface grid for coarse and fine CFD grids are given in Figure 3.6, and the number of surface triangular elements and volume tetrahedral elements are shown in Table 3.3

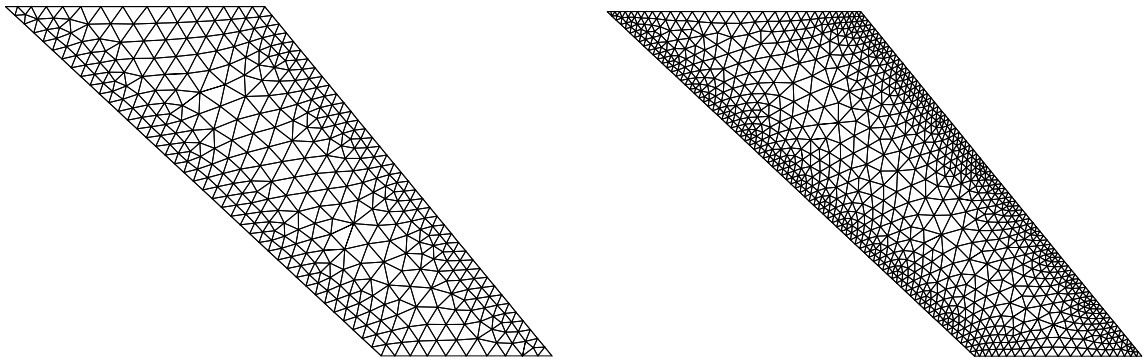

a b

Figure 3.6 Wing Surface Triangular Elements a) Coarse b) Fine

Table 3.3 Number of Surface Triangular and Volume Tetrahedral Elements

| **Mesh** | **Number of Surface Triangular Elements** | **Number of Tetrahedral Elements** |
|---|---|---|
| Coarse Mesh | 1,468 | 79,503 |
| Medium Mesh | 1,468 | 110,229 |
| Fine Mesh | 3,798 | 158,161 |
| Very Fine Mesh | 3,798 | 211,360 |

Calculated pressure coefficient distributions over the bottom and top surface wing for M= 0.499 and $\alpha=0^{o}$ for two different spanwise locations are shown in Figures 3.7-3.8.

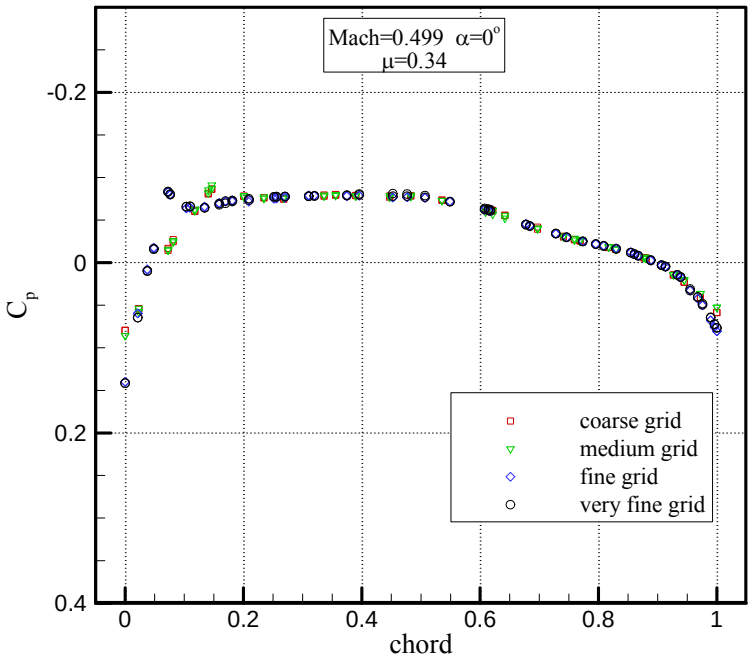


Figure 3.7 Wing $C_p$ Distribution at 34 % Semispan (M=0.499 α=0°)

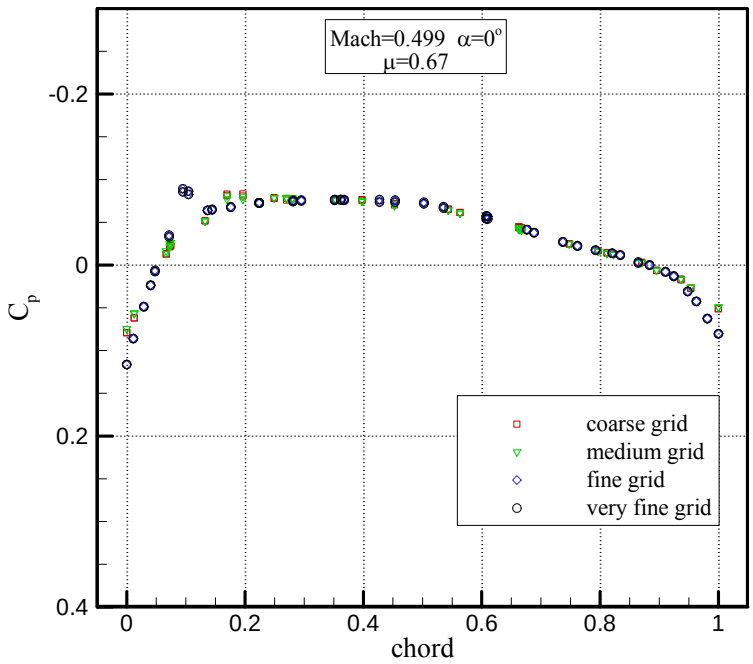


Figure 3.8 Wing $C_p$ Distribution at 67 % Semispan (M=0.499 α=0°)

At 34 % semispan of the wing, coarse, medium, fine and very fine grids predict the maximum Cp value ($Cp_{max}$) of 0.0796, 0.0857, 0.140, and 0.141, respectively. Flow solution with coarse grid predicts 44 % lower $Cp_{max}$ value as compared to very fine grid. Fine grid predicts $Cp_{max}$ value almost same as very fine grid.

At 67 % semispan of the wing, coarse grid predicts 32 % lower $Cp_{max}$ value whereas medium grid predicts 36 % lower $Cp_{max}$ value as compared to fine and very fine grids.

Contours of pressure coefficient over the top and bottom surfaces of the wing are shown in Figure 3.9.

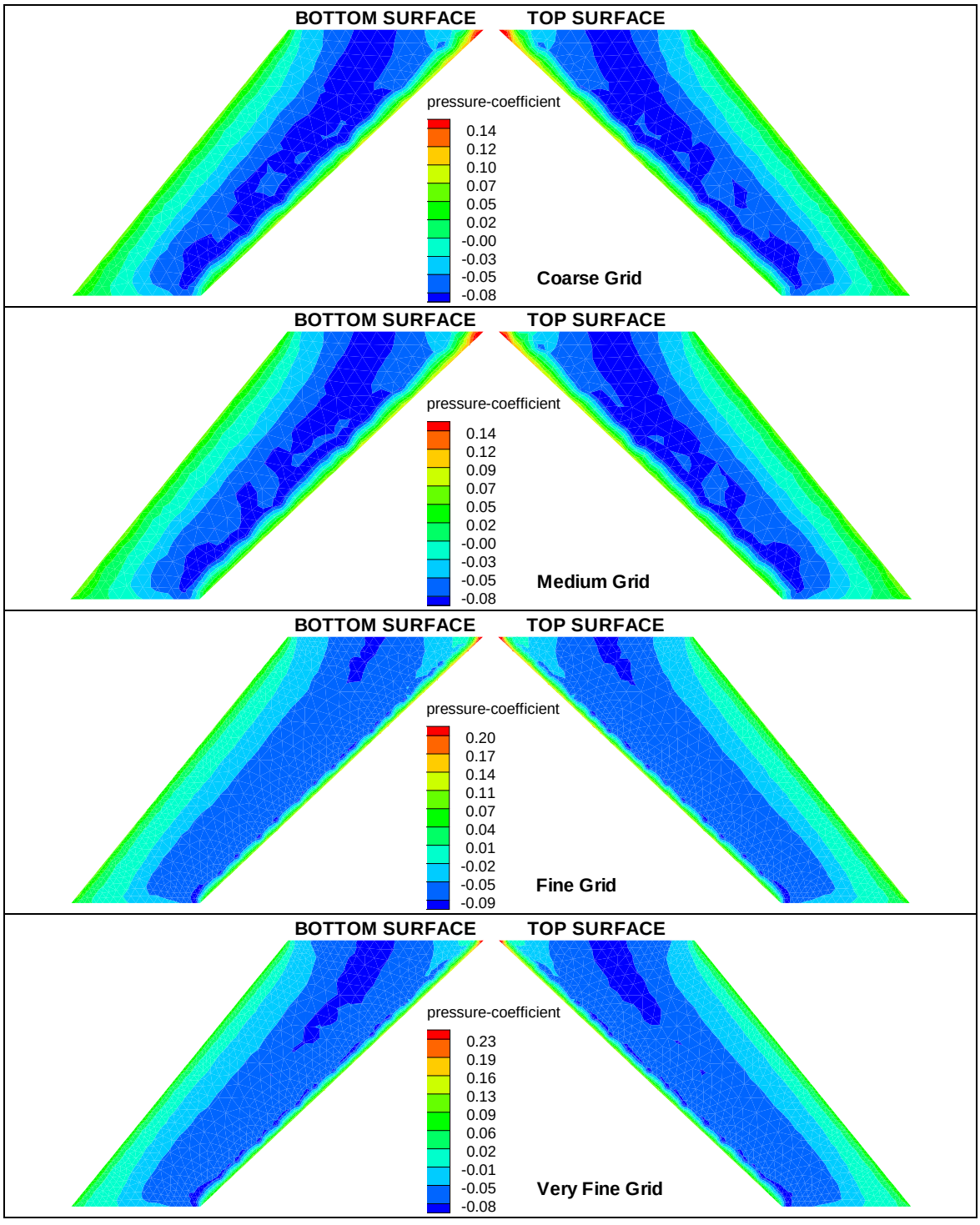


Figure 3.9 Pressure Coefficient Contours over Top and Bottom Surfaces of AGARD Wing 445.6 (M=0.499 $\alpha=0^{o}$)

The pressure coefficient distributions over the wing for M= 0.85 and α=5$^o$ are similarly shown in Figures 3.10-3.11 at two different spanwise locations.

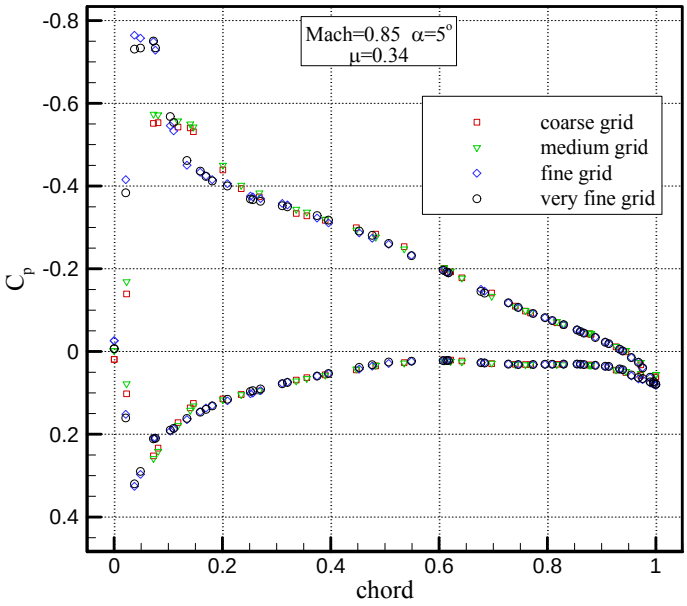


Figure 3.10 Wing $C_p$ Distribution at 34 % Semispan (M=0.85 α=5$^o$)

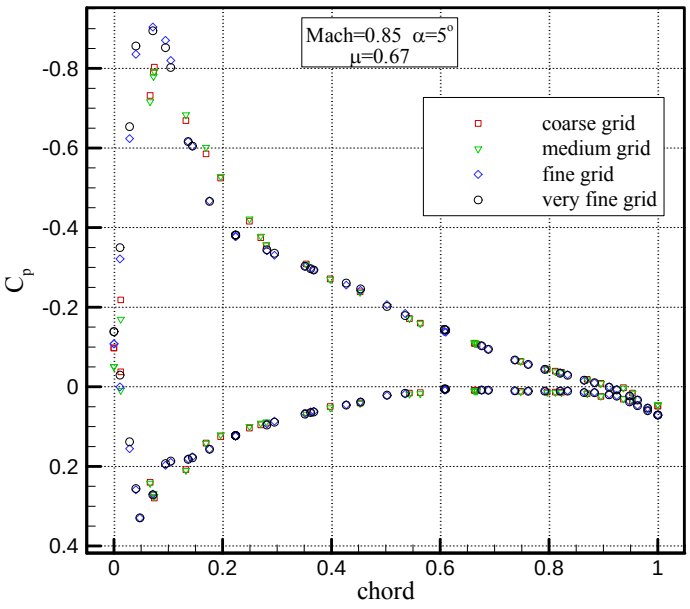


Figure 3.11 Wing $C_p$ Distribution at 67 % Semispan (M=0.85 α=5$^o$)

As can be seen from Figure 3.10 and 3.11, pressure coefficient distributions over the leading edge are different for coarse, mesh and fine grids. At 34 % semispan of the wing, coarse grid predicts the minimum Cp value ($Cp_{min}$) of -0.553, medium grid predicts $Cp_{min}$ of -0.574, fine grid predicts $Cp_{min}$ of -0.733 and very fine predicts $Cp_{min}$ of -0764. Flow solution with coarse grids predicts 28 % higher $Cp_{min}$ value and medium grid predicts 25 % higher $Cp_{min}$ value and fine grid predicts 4 % higher $Cp_{min}$ value as compared to very fine grid. These minimum values occur at 3.8% chord location for fine and very fine grids whereas for medium and coarse grid it occurs at 5.7 % chord location.

At 67 % semispan of the wing, coarse and medium grids predict 19.4 % and 20.5 % higher $Cp_{min}$ value as compared to very fine grids, respectively. For fine grids these values occur at 4.8 % chord location and for medium and coarse grids, it occurs at 8 % chord locations.

Contours of pressure coefficient over the top and bottom surfaces of the wing are shown in Figure 3.12.

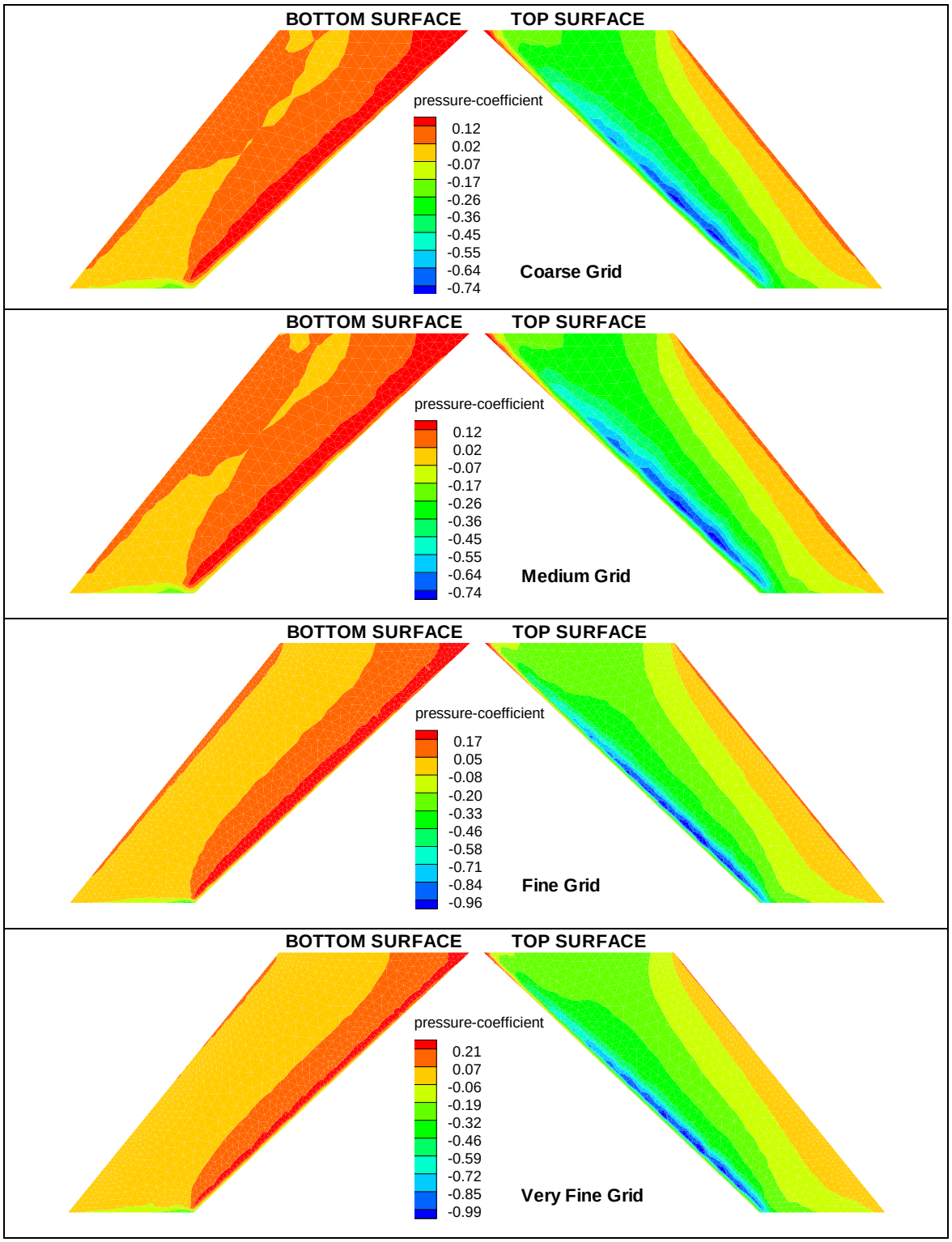


Figure 3.12 Pressure Coefficient Contours over Top and Bottom Surfaces of AGARD Wing 445.6 (M=0.85 $\alpha=5^{o}$)

The pressure coefficient distributions over the wing for M= 0.96 and α=0° are similarly shown in Figures 3.13-3.14 at two different spanwise locations.

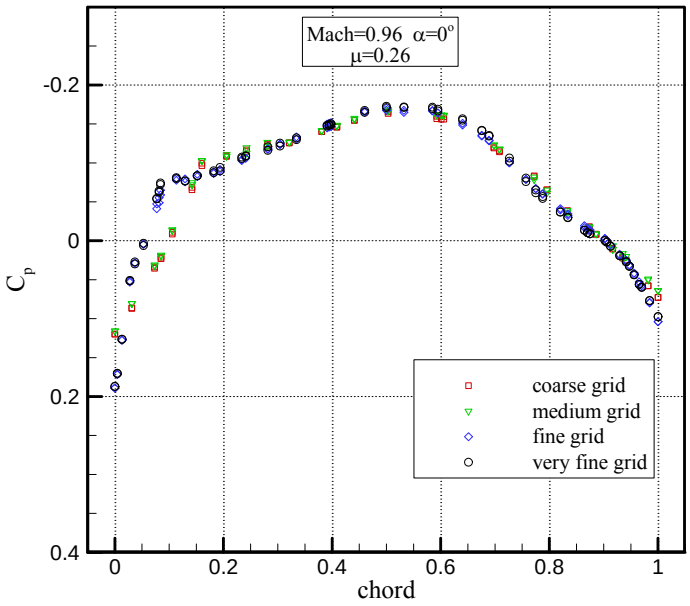


Figure 3.13 Wing $C_p$ Distribution at 26 % Semispan (M=0.96 α=0°)

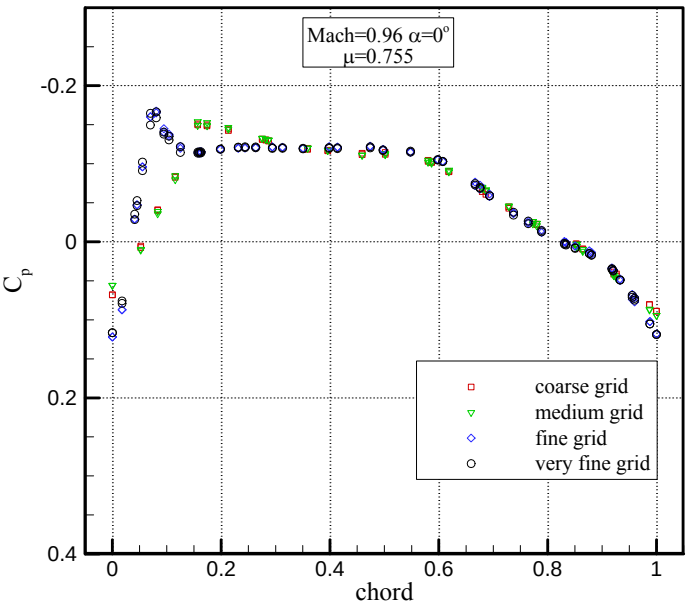


Figure 3.14 Wing $C_p$ Distribution at 75.5 % Semispan (M=0.96 α=0°)

At 26 % semispan of the wing, coarse and medium grids predict the maximum Cp value of 0.120 and 116, fine and very fine grids predict $Cp_{max}$ of 0.188. Flow solution with coarse and medium grids predicts 36.2 % and 38.3 % lower $Cp_{max}$ value as compared to fine grids.

At 75.5 % semispan of the wing, coarse, medium, fine and very fine grids predict $Cp_{max}$ of 0.068, 0.056, 0.121 and 0.116, respectively.

Contours of pressure coefficient over the top and bottom surfaces of the wing are shown in Figure 3.15.

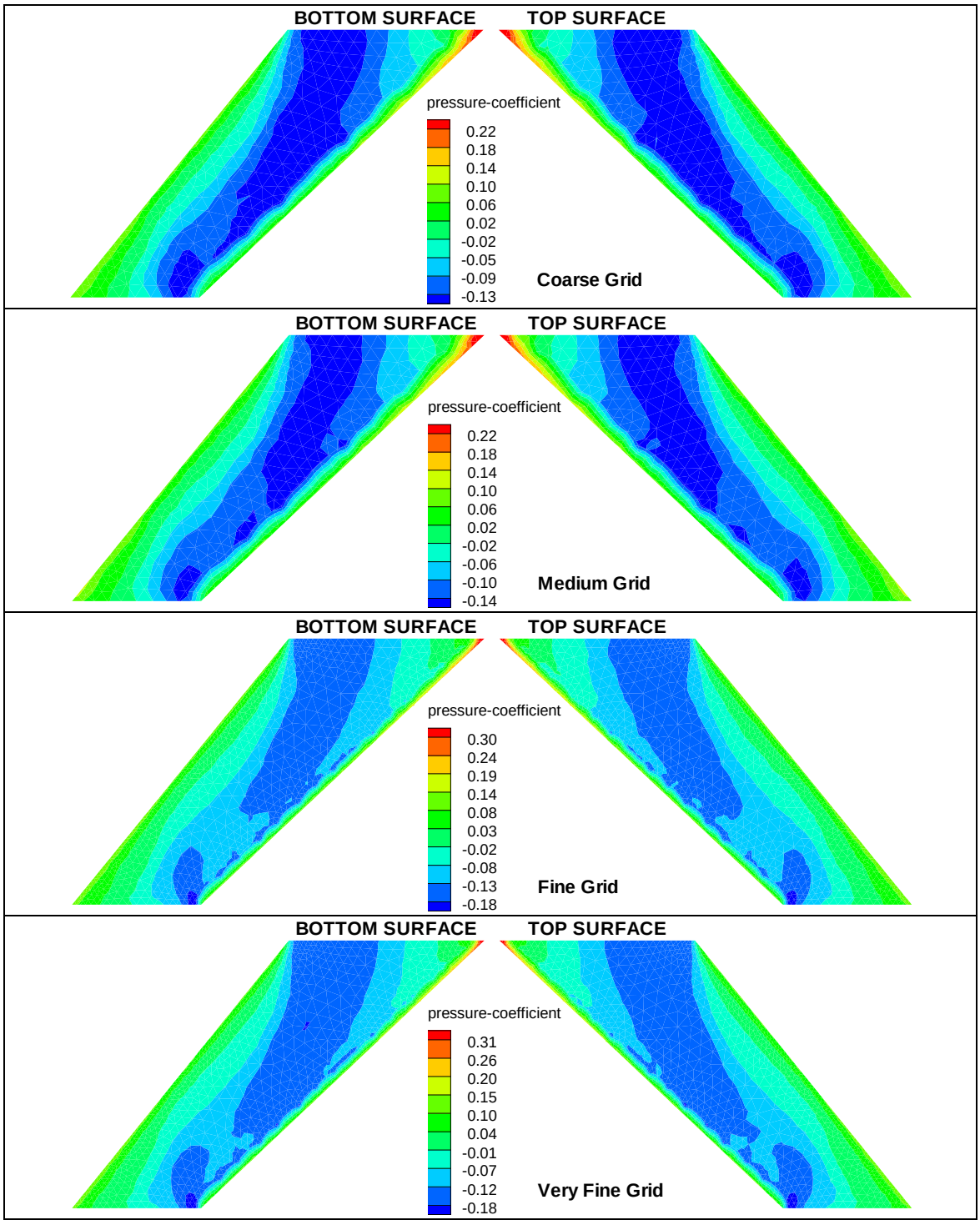


Figure 3.15 Pressure Coefficient Contours over Top and Bottom Surfaces of AGARD Wing 445.6 (M=0.96 $\alpha=0^{o}$)

The pressure coefficient distributions over the wing for M= 1.141 and α=0° are similarly shown in Figures 3.16-3.17 at two different spanwise locations.

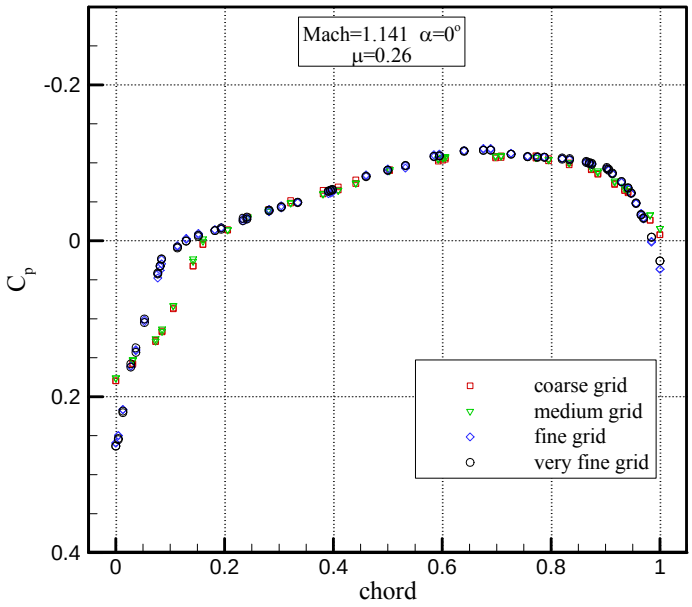


Figure 3.16 Wing $C_p$ Distribution at 26 % Semispan (M=1.141 α=0°)

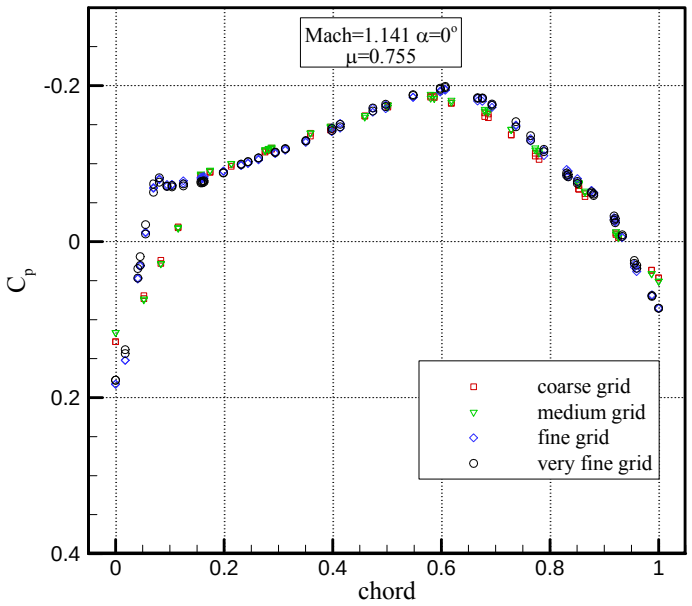


Figure 3.17 Wing $C_p$ Distribution at 75.5 % Semispan (M=1.141 α=0°)

At 26 % semispan of the wing, coarse grid predicts the maximum Cp value of 0.179, medium grid predicts $Cp_{max}$ of 0.177, fine grid predicts $Cp_{max}$ of 0.259 and very fine grid predicts $Cp_{max}$ of 0.263. Flow solution with coarse and medium grids predicts 32 % lower $Cp_{max}$ value as compared to fine grids.

At 75.5 % semispan of the wing, coarse, medium, fine and very fine grids predict $Cp_{max}$ of 0.128, 0.117, 0.183 and 0.178, respectively.

Contours of pressure coefficient over the top and bottom surfaces of the wing are shown in Figure 3.18.

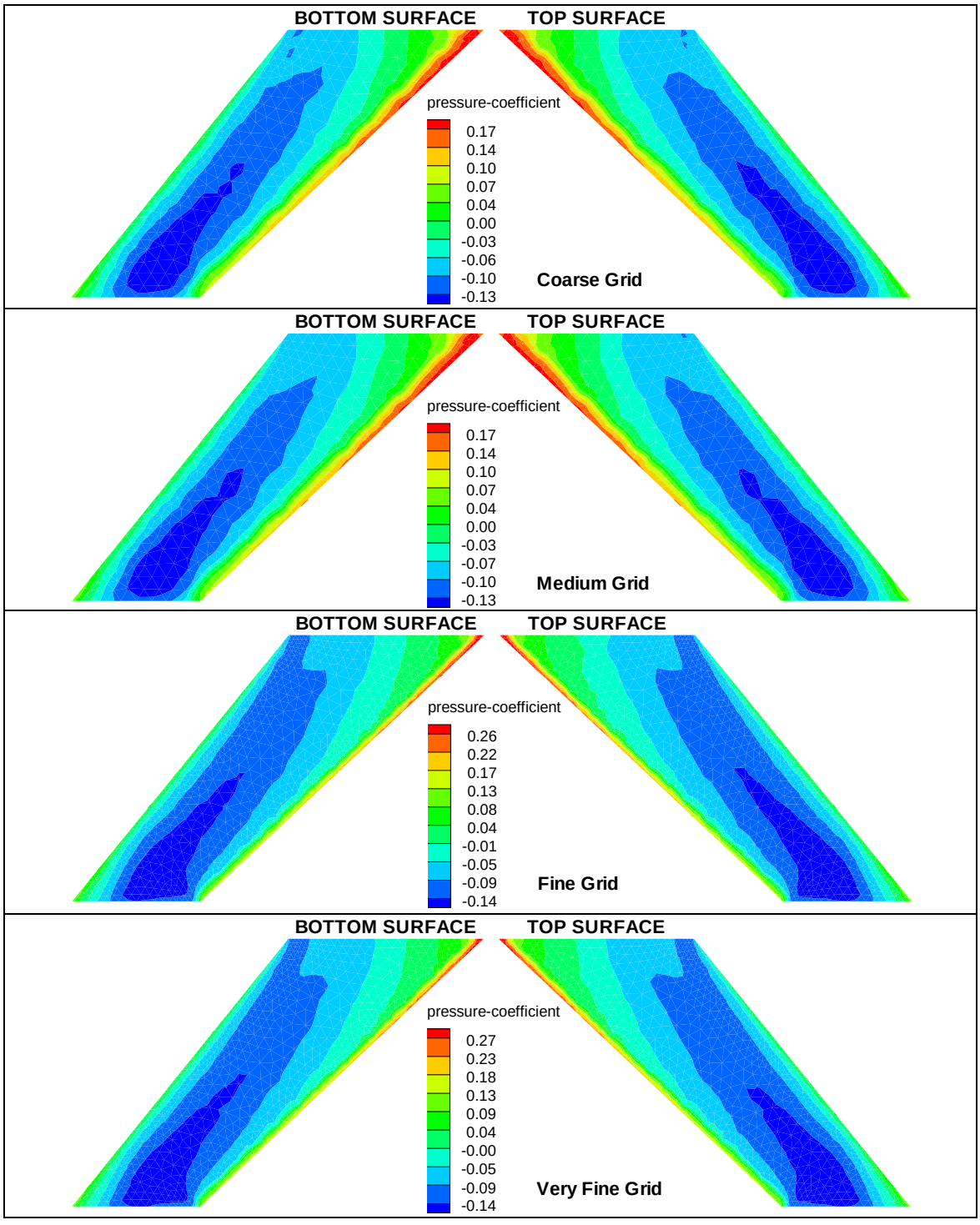


Figure 3.18 Pressure Coefficient Contours over Top and Bottom Surfaces of AGARD Wing 445.6 (M=1.141 $\alpha=0^{o}$)

For the flow conditions at which grid sensitivity analysis conducted, it can be concluded that flow solution with coarse and medium grid, which have coarsest surface grid density give grid dependent results. Flow solution with fine and very fine grids give similar results. Since fine grid has less number of tetrahedral elements, for the further studies fine grid will be used. In the next section, flow solution calculated with fine grid is compared with numerical results conducted by Cai [4], Lee and Batina [3].

#### *3.1.2.2 Comparison with Numerical Results*

In this part, pressure coefficient distribution over the AGARD Wing 445.6 is compared with the study of Cai [4]. Cai conducted static aeroelastic analysis of AGARD Wing 445.6 at flow condition M=0.85 $\alpha$=5°. Pressure coefficient distributions over the wing at % 34 spanwise locations for this flow condition are shown in Figure 3.19. Results appear to agree well except for leading edge. This difference may be attributed to the meshing technique. Cai [4] uses O-Type structured grid which captures leading edge radius accurately and gives better resolution of the leading edge radius. In the present work unstructured grid and limited number of triangular mesh is used, and hence leading edge radius of the wing cannot be modeled correctly.

At 67 % semispan of the wing, Cai [4] predicts higher Cp values between 10% and 50% local chord locations (Figure 3.20). This may be attributed to difference between the flow solvers.

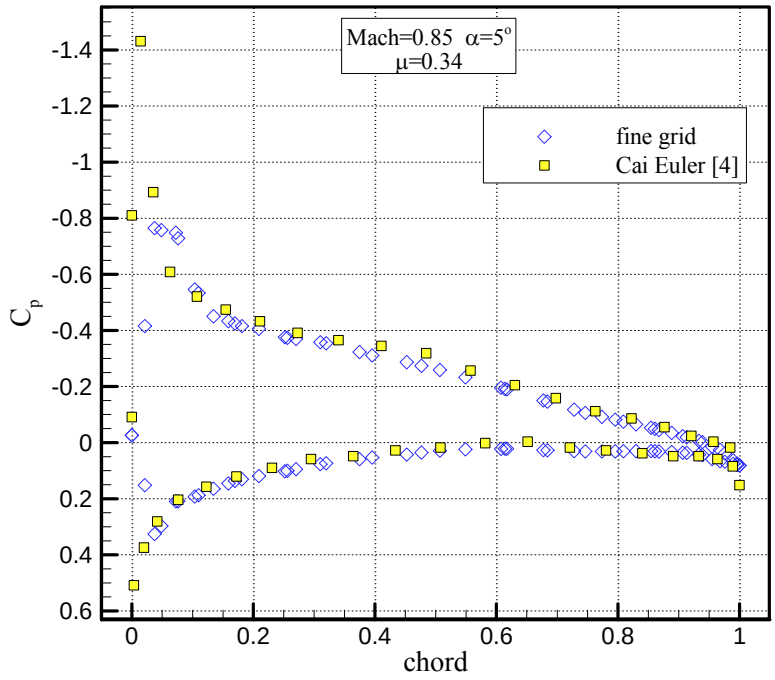


Figure 3.19 Comparison of $C_p$ Distribution at 34% Semispan (M=0.85 α=5°)

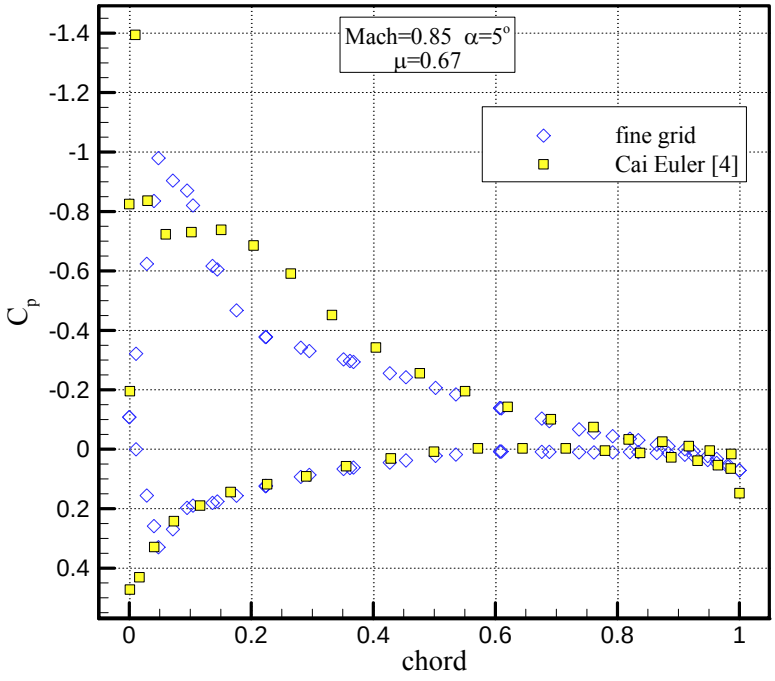


Figure 3.20 Comparison of $C_p$ Distribution at 67% Semispan (M=0.85 α=5°)

The pressure coefficient distribution over the AGARD Wing 445.6 is compared with the study of Lee and Batina [3]. Lee and Batina conducted dynamic aeroelastic analysis of AGARD Wing 445.6 at flow conditions M=1.141 and α=0°. Pressure coefficient distributions over the wing at 26% and 75.5 % spanwise locations are shown in Figure 3.21 and 3.22, respectively.

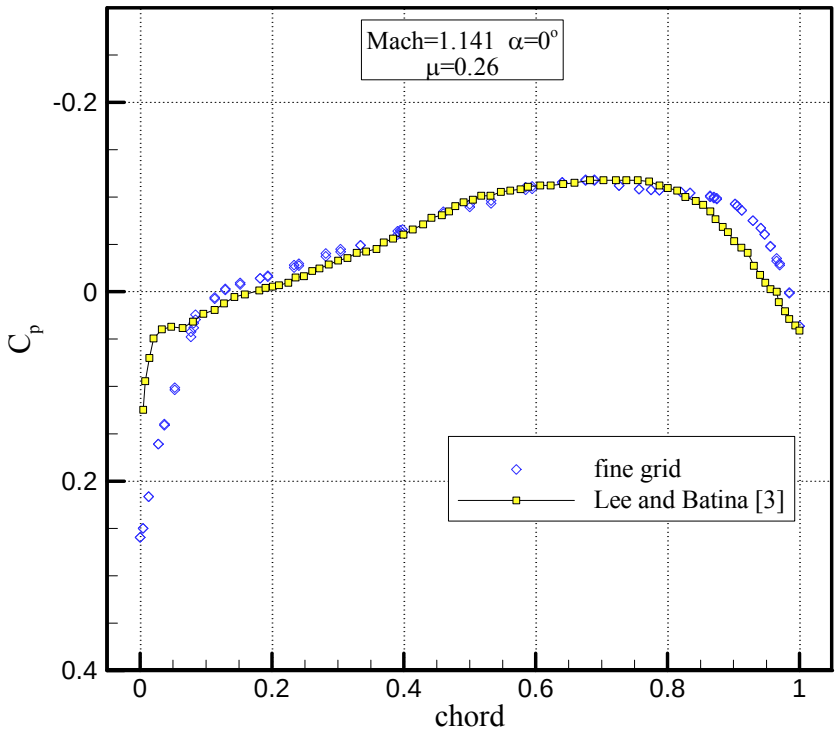


Figure 3.21 Comparison of $C_p$ Distribution at 26% Semispan (M=1.141 α=0°)

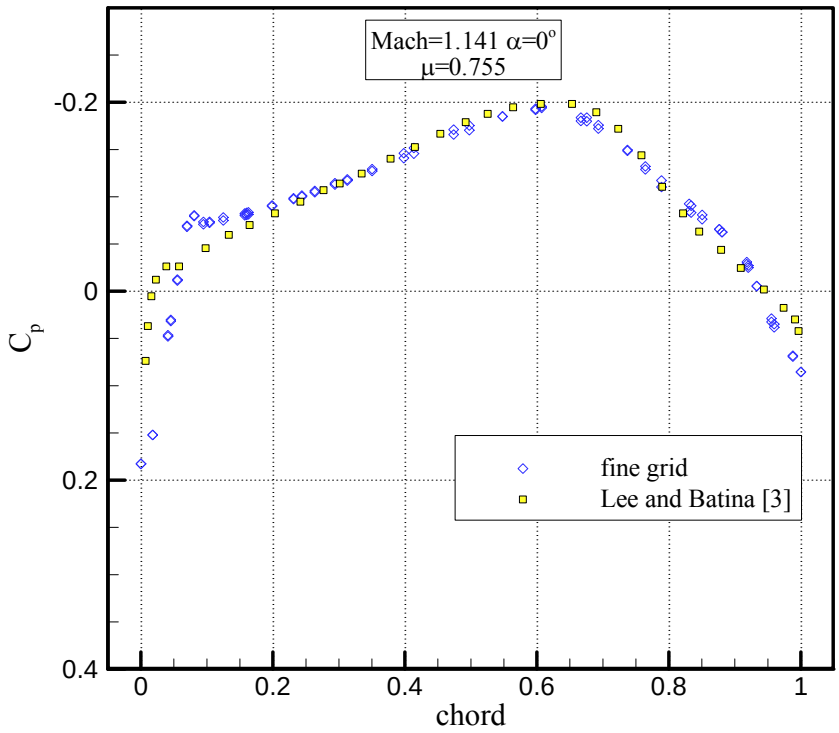


Figure 3.22 Comparison of $C_p$ Distribution at 75.5% Semispan (M=1.141 $\alpha=0^o$)

Pressure coefficient distributions over the wing at two spanwise locations for this flow condition appear to agree well except for leading and trailing edges. This difference may be attributed to the meshing technique. Lee and Batina [3] use C-H type of grid which provides better resolution at the leading and trailing edge as compared to the present study.

### *3.1.3 AGARD WING 445.6 STRUCTURAL ANALYSIS*

#### *3.1.3.1 Grid Sensitivity Study and Validation of Structural Model*

In this part, the details of the finite element analyses and the results of the modal analyses are given. Modal frequencies of the AGARD Wing 445.6 are compared with experimental data [1] in order to validate structural finite element model, which is used in static and dynamic calculations in the following sections. In addition to the calculated modal frequencies, mode shapes of the structure are also compared with the experimental study [1].

Weakened AGARD Wing 445.6 is modeled with plate elements as a single layer orthotropic material of which property is given in Table 3.1. The rotations and translations of the nodes at the root section of the finite element model are fixed. Other nodes are allowed to translate in out-of-plane direction. In order to perform grid sensitivity analysis for the structural grids, results of the modal analysis which are conducted with three different structured grids with varying density, are compared with experimental and numerical data. CQUAD4 type of element is used for the finite element discretization. The numbers of nodes for the spanwise and chordwise directions for each finite element model are shown in Table 3.4. Finite element models and corresponding thickness distribution which are used for finite element modal analysis are shown in Figure 3.23.

Table 3.4 Number of Elements Used in Finite Element Model

| Mesh | Number of Nodes for the Spanwise Direction | Number of Nodes for the Chordwise Direction | Total number of Structured Element |
|---|---|---|---|
| Coarse Mesh | 6 | 5 | 20 |
| Medium Mesh | 12 | 12 | 121 |
| Fine Mesh | 51 | 41 | 2000 |

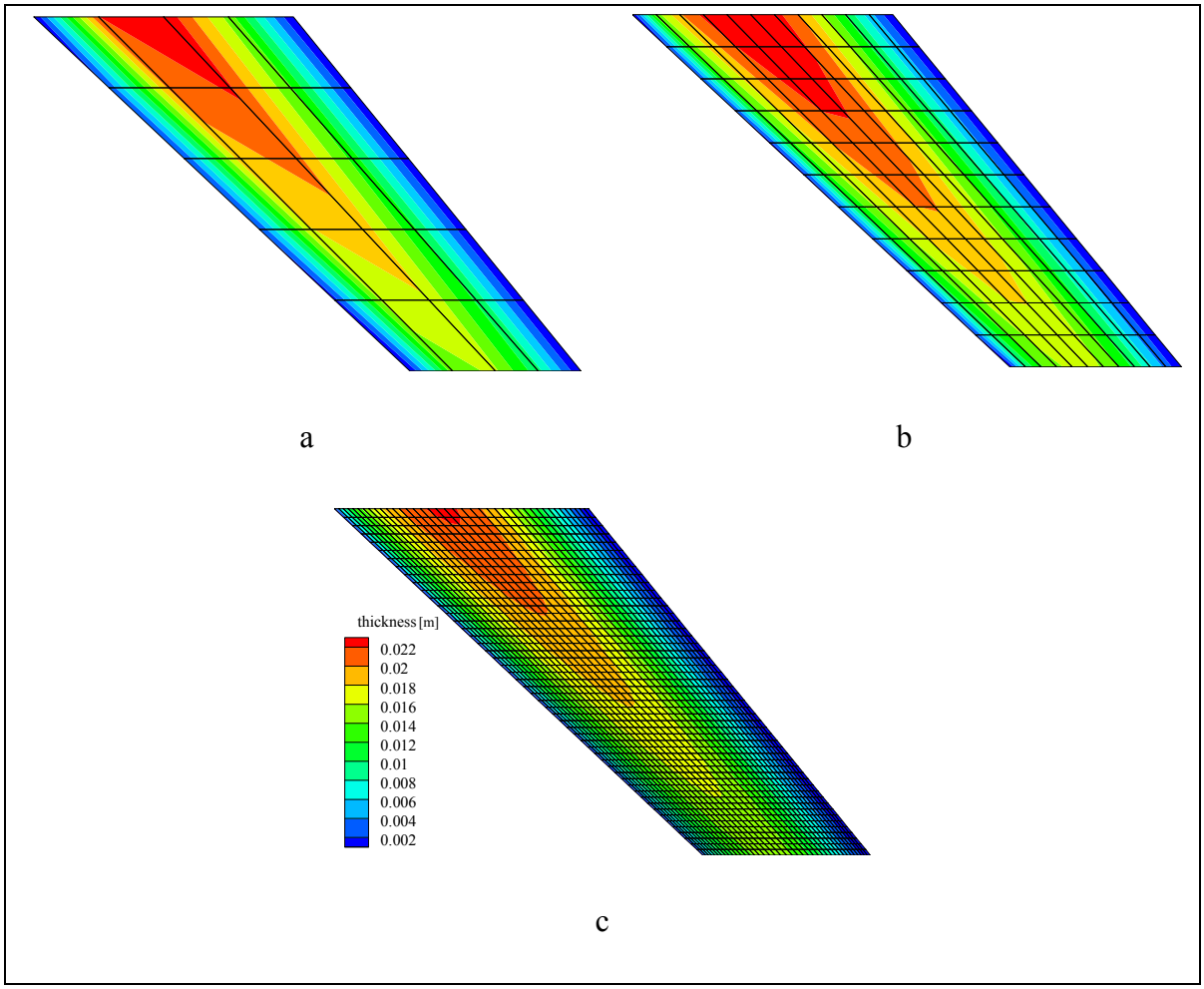


Figure 3.23 Structural Finite Element Models and Thickness Distribution

a) Coarse Mesh b) Medium Mesh c) Fine Mesh

For each finite element models, modal analysis of weakened AGARD Wing 445.6 is performed using MSC/NASTRAN. The first four natural frequencies are given in Table 3.5 for the three different finite element models along with the experimental results [1] and those computed by Kolonay [2], Lee and Batina [3].

Table 3.5 Calculated Natural Frequencies for Weakened AGARD Wing 445.6

| | Mode 1 [Hz] | Mode 2[Hz] | Mode 3 [Hz] | Mode 4 [Hz] |
|---|---|---|---|---|
| Coarse Mesh | 8.72 | 34.85 | 41.43 | 70.65 |
| Medium Mesh | 9.41 | 39.46 | 48.96 | 94.35 |
| Fine Mesh | 9.62 | 39.75 | 50.85 | 95.38 |
| Exp. (Yates) [1] | 9.60 | 38.10 | 50.70 | 98.50 |
| *Kolonay [2]* | *9.63* | *37.12* | *50.50* | *89.94* |
| *Lee and Batina [3]* | *9.60* | *38.17* | *48.35* | *91.54* |

Percent error values in natural frequencies increase with decreasing element number. Percent errors in first natural frequency for coarse, medium and fine grids are 9.17, 1.98 and 0.21, respectively. Error values for four natural frequencies are summarized in Table 3.6

Table 3.6 Percent Error Values in Natural Frequencies

| Natural Frequency [Hz] | | | | |
|---|---|---|---|---|
| Grid | Mode 1 | Mode 2 | Mode 3 | Mode 4 |
| Coarse (% Error) | 9.17 | 8.53 | 18.28 | 28.27 |
| Medium (% Error) | 1.98 | 4.22 | 3.43 | 4.21 |
| Fine (% Error) | 0.21 | 4.33 | 0.3 | 3.17 |

The percent error values of coarse grid are very high as compared to medium and fine grids. Medium grid predicts natural frequency values very close to the values that fine grid predict. Considering the number of elements, medium grid is selected for the following studies in order to decrease computational effort. The mode shapes are mainly based on wing out-of-plane deflection values. Calculated natural frequencies and mode shapes of the structure using medium grid are shown in Figure 3.24.

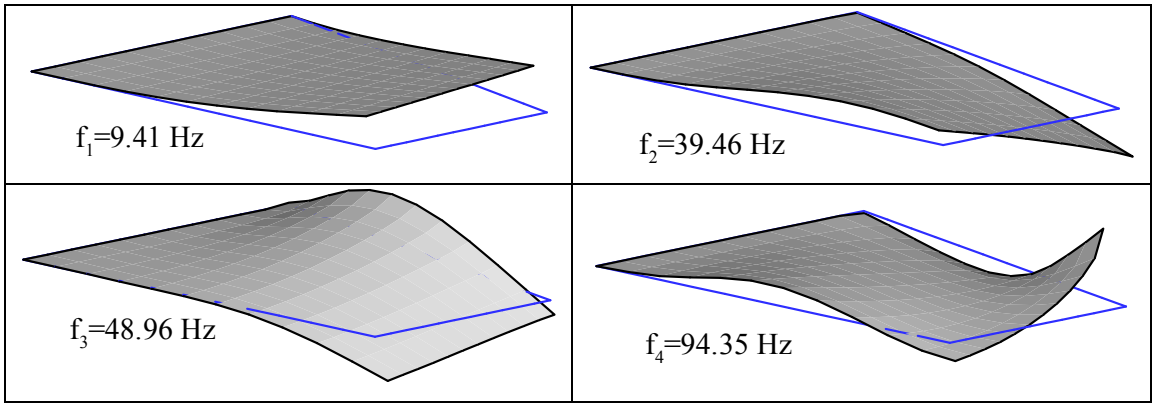


Figure 3.24 Mode Shapes of Medium Grid Structural Finite Element Model

Mode shapes obtained from finite element analysis of the weakened wing are scaled up so that maximum and minimum values are same that of experiments. Out of plane deflection contours are compared in Figure 3.25. It can be concluded that results obtained from finite element model with medium grid appear to agree well with experimental results and hence medium grid can be used for the further static and dynamic aeroelastic analyses.

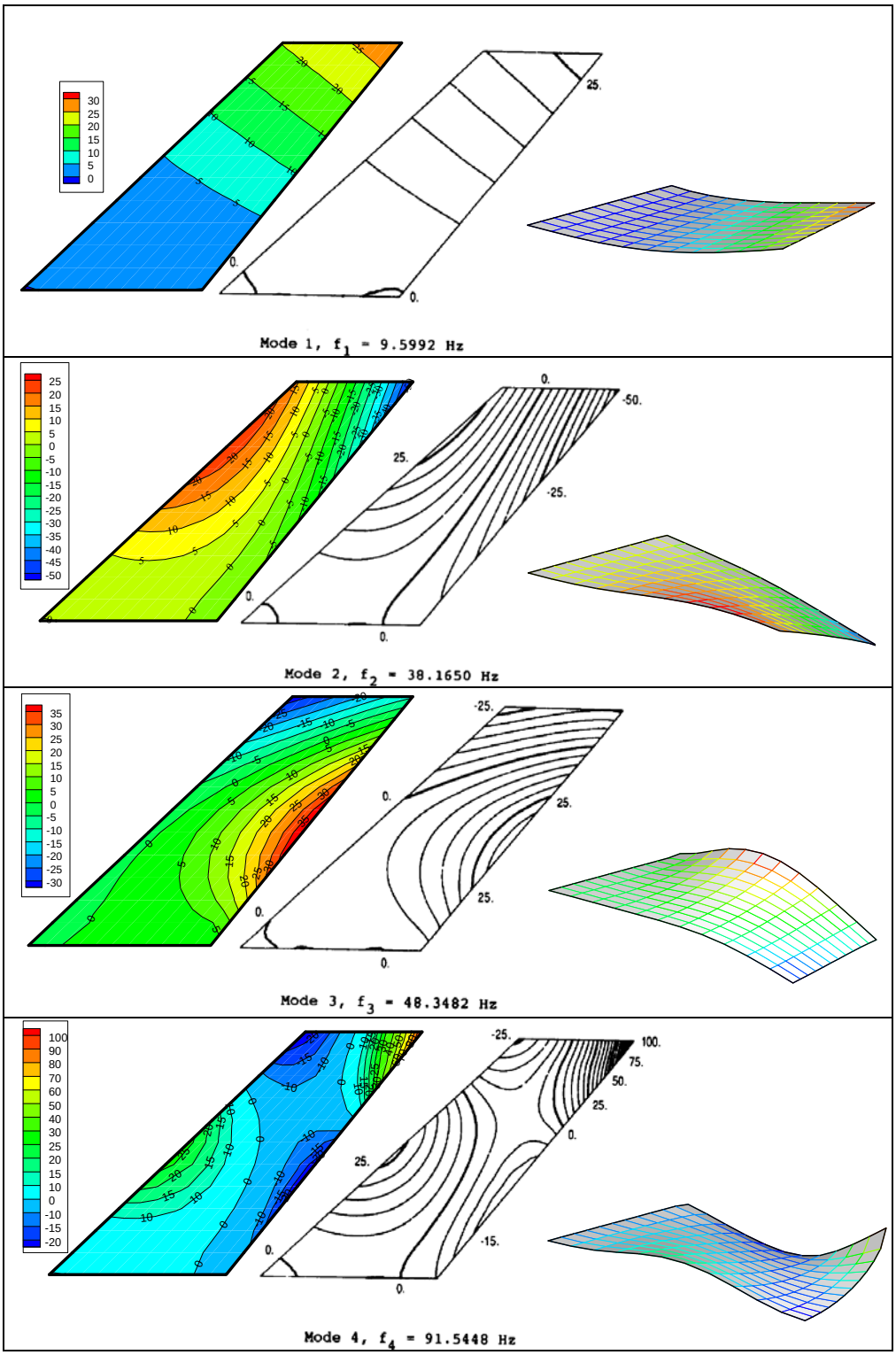


Figure 3.25 Comparison of Calculated Mode Shapes of AGARD Wing 445.6 (left) with Experiments (right)

### *3.1.4 STATIC AEROELASTIC ANALYSIS of the AGARD WING 445.6*

In this part, details of static aeroelastic analysis of AGARD Wing 445.6 are given and results are compared with numerical values [4].

Static aeroelastic analyses are initiated by computing an initial steady-state solution for the rigid AGARD Wing 445.6. This converged flow solution is used as a starting point for static aeroelastic iterations. Aeroelastic iterations continue until the difference of the root mean square values of structural displacements between two consecutive iterations is less than the prescribed tolerance ($10^{-6}$). The change of the root mean square of out-of-plane deformation and lift coefficient during the aeroelastic simulation are shown in Figures 3.26 and 3.27, respectively.

In this study, pressure-velocity coupling algorithm of PISO is applied with the second order upwinding scheme for density, momentum and energy equations. Since FLUENT calculates pressures at the cell centers, for every time step, surface loads, P, should be mapped from the face centroids of the aerodynamic grid onto structural grid. MSC/NASTRAN, finite element commercial software is used for static structural analysis in order to solve the displacements associated with the aerodynamic pressure loads calculated by FLUENT. These displacements also need to be interpolated onto CFD grid in order to obtain new CFD surface grid. For static aeroelastic analyses, linear interpolation method using ADT, which was explained in Chapter 2.3.1, is performed to transfer displacements and pressure loads between the structural and aerodynamic grid points. The aerodynamic mesh must be modified in order to adapt the new shape of the aerodynamic surface, representing the structural deformation at each aeroelastic time step. In this study, FLUENT moving mesh algorithm is used for deforming process without generating a new grid at each time step. To achieve this, a user defined function is created and implemented in a code which deforms the mesh according to structural finite element analysis. FLUENT mesh deforming parameters, which are used in this study, are shown in Table 3.7.

Table 3.7 FLUENT Mesh Deformation Algorithm Parameters

| **Smoothing** | |
|---|---|
| Spring Constant Factor | 1e-4 |
| Convergence Tolerance | 1e-5 |
| Number of Iteration | 100 |
| **Remeshing** | |
| Maximum Cell Skewness | 0.78 |
| Size Remesh Interval | 10 |

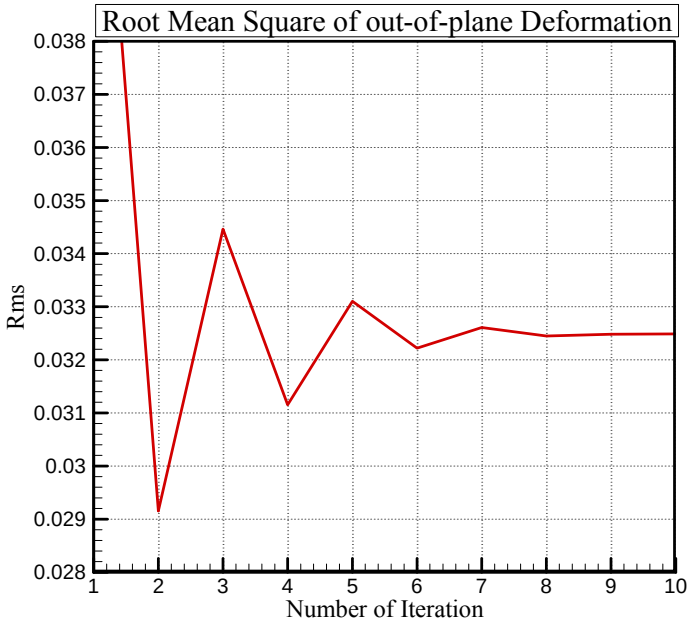


Figure 3.26 The Root Mean Square of out-of- plane Deformation at Each Aeroelastic Time-step

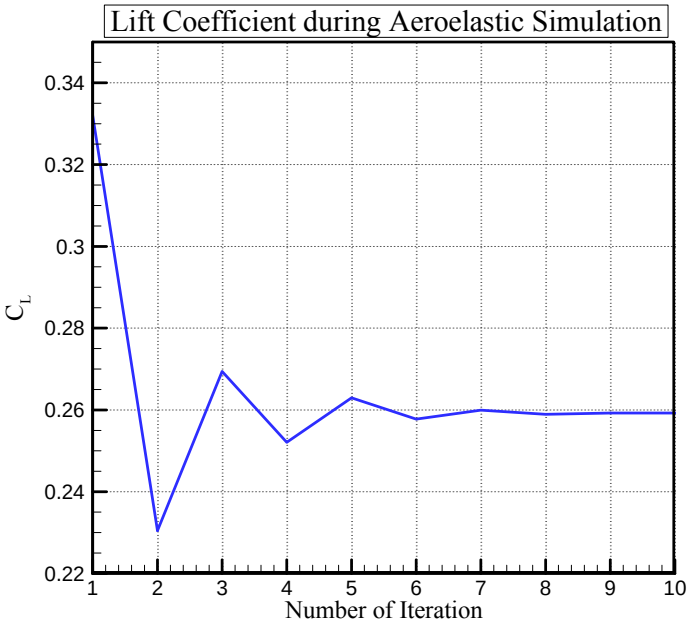


Figure 3.27 Lift Coefficient Value at Each Aeroelastic Time-step

The convergence history of lift coefficient for rigid and elastic wings during aeroelastic simulation is shown in Figure 3.28. Each iteration step continues until constant lift and drag coefficient values are obtained and nodal grid point locations in the flow domain are updated based on the results of static structural finite element analyses.

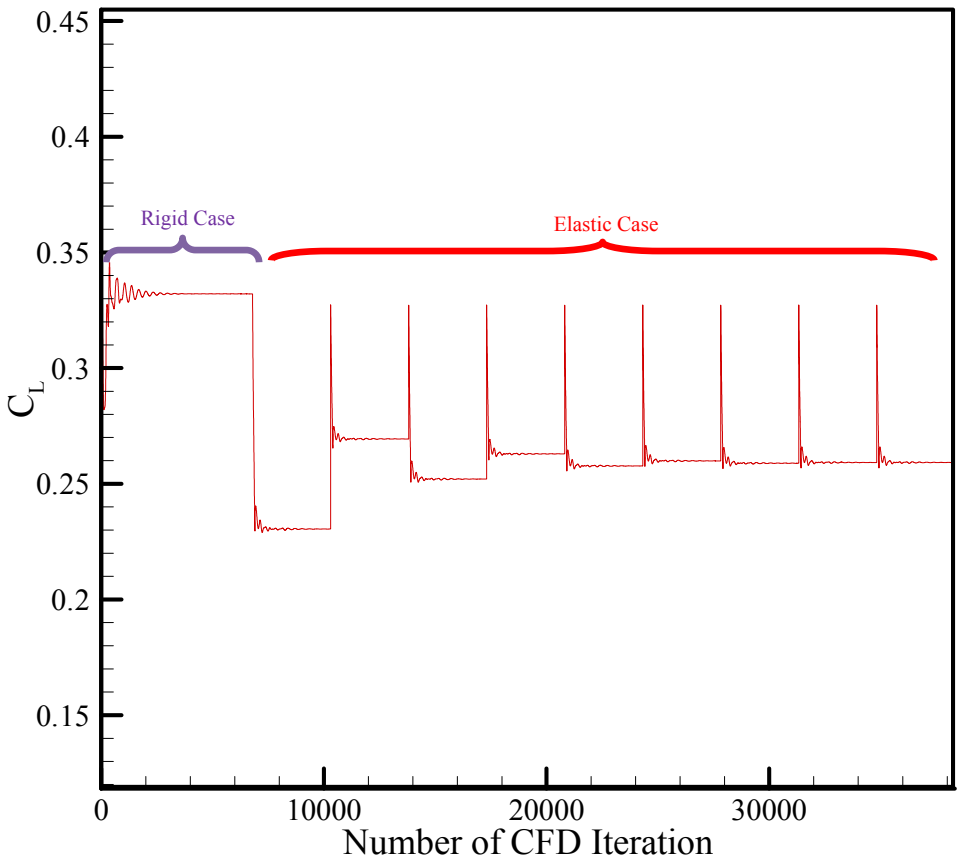


Figure 3.28 Lift Coefficient Convergency during Aeroelastic Simulation

Rigid and elastic wing pressure coefficient distributions calculated in the present study are given in Figures 3.29 and 3.30 at two different spanwise locations. $C_p$ values on the surface decreases in elastic wing due to decreased pressure values. The lift coefficient of the elastic wing is reduced by 22 % as compared to rigid wing case.

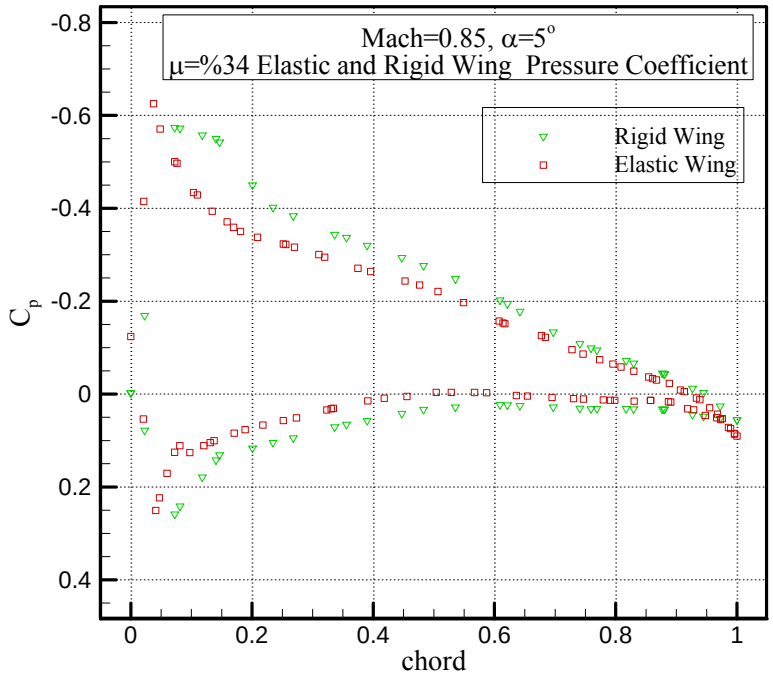


Figure 3.29 Elastic and Rigid Wing Cp Distribution at 34 % Semispan (M=0.85 α=5°)

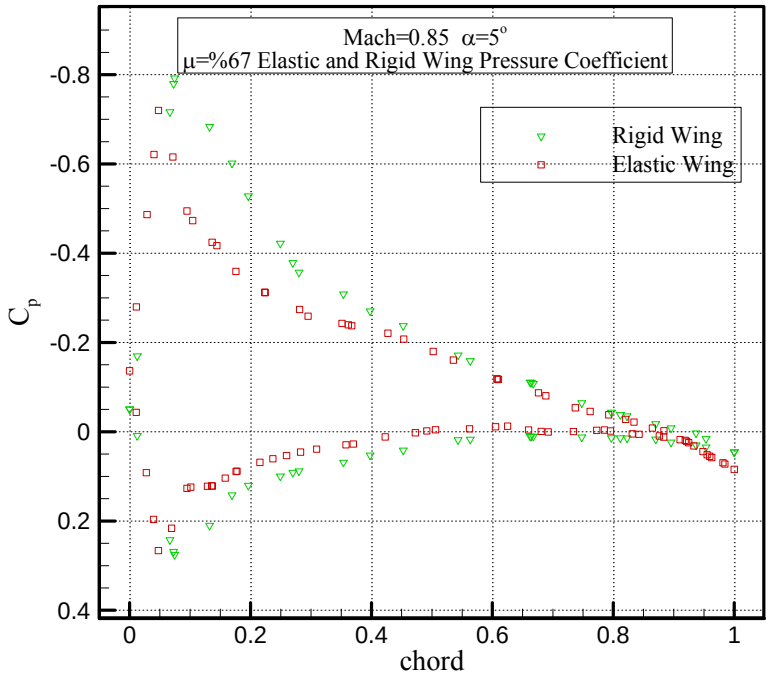


Figure 3.30 Elastic and Rigid Wing Cp Distribution at 67 % Semispan (M=0.85 α=5°)

Out-of-plane deformations of AGARD Wing 445.6 at leading and trailing edges are compared with the results of Cai [4] in Figures 3.31 and 3.32. It can be concluded that, results of present study appear to agree well with the results of Cai [4]. Maximum difference occurs at the wing tip. At the leading edge of the wing tip, Cai calculates 2.181 inch deflection whereas it is calculated as 2.176 inch in the present study. At the trailing edge, Cai calculates 2.418 whereas it is calculated as 2.591 inch in the present study. This difference diminishes towards the root of the wing.

It should be considered that in the present study, finite element model of the AGARD Wing 445.6 consists of plate elements. Structural analyses are performed with MSC/NASTRAN by allowing only out-of-plane deformation of the structural grid nodes in order to simplify the calculations. In the present static aeroelastic calculations, closely coupled approach is used, whereas Cai [4] uses monolithic approach which fluid and structure equations are combined in one single system in order to calculate the deformation of the wing under the aerodynamic loading.

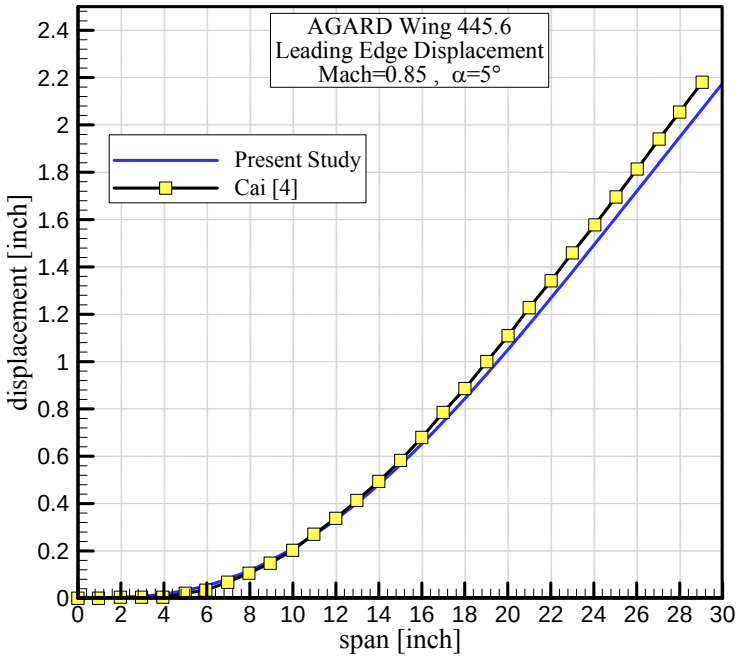


Figure 3.31 Leading Edge Out-of-Plane Deformation

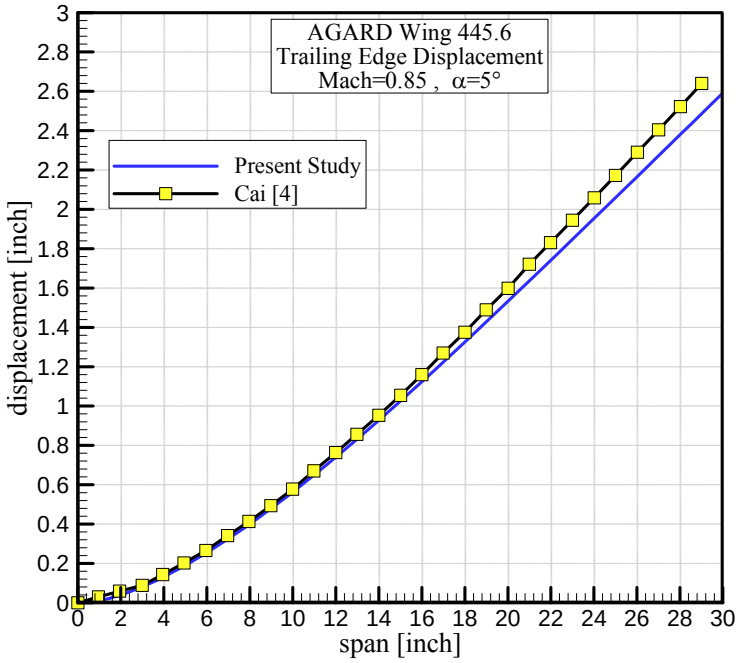


Figure 3.32 Trailing Edge Out-of-Plane Deformation

Elastic wing pressure coefficient distributions at 34 % and 67 % spanwise locations are compared with the results of Cai [4] in Figures 3.33 and 3.34.

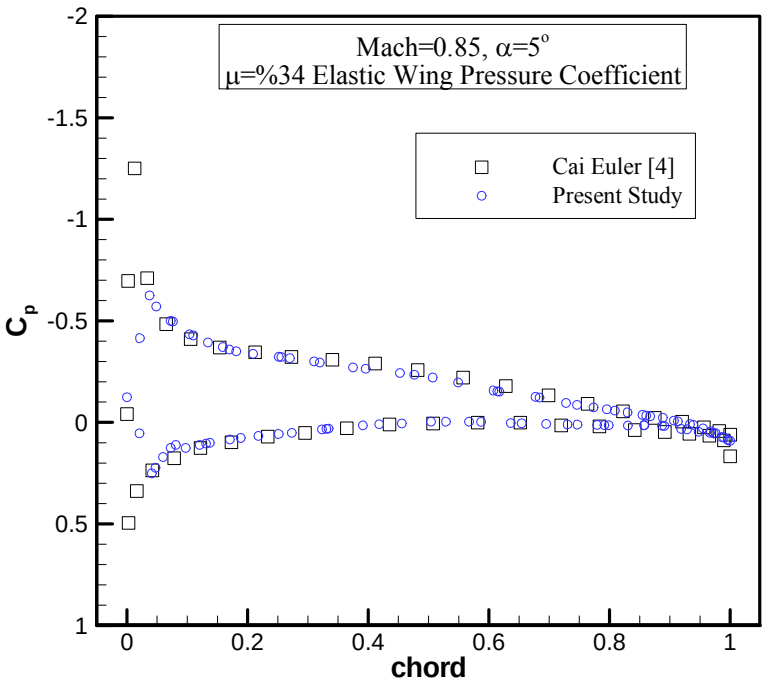


Figure 3.33 Comparison of Elastic Wing Cp Distribution at 34 % Semispan

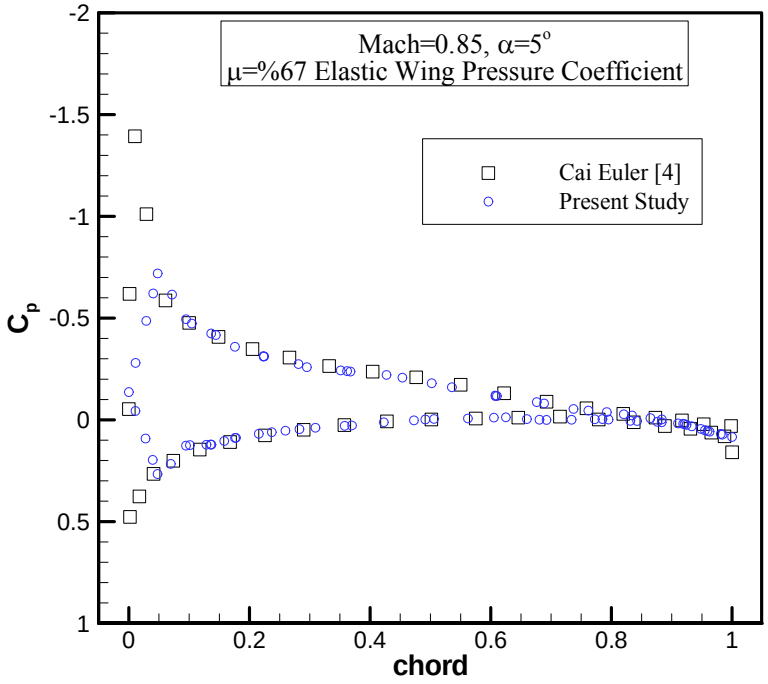


Figure 3.34 Comparison of Elastic Wing Cp Distribution at 67 % Semispan

Equilibrium position for elastic wing is compared with rigid wing is given in Figure 3.35.

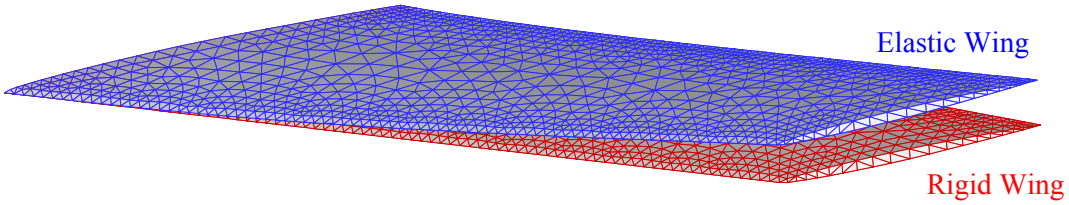


Figure 3.35 Rigid (red) and Elastic (blue) Position of AGARD Wing 445.6

### *3.1.5 DYNAMIC AEROELASTIC ANALYSIS of the AGARD WING 445.6*

In this part, details of dynamic aeroelastic analysis of AGARD Wing 445.6 and developed coupling scheme are given, and results are compared with experimental [1] and numerical values [3] [35]. The purpose of the dynamic analyses is to determine the Flutter Speed Index (FSI) at different Mach numbers.

In the present dynamic aeroelastic study, a coupling scheme is developed around a commercial CFD code, namely FLUENT, and a linear modal structural model of which details are given in Chapter 2.6. Dynamic analyses are performed in time domain by closely coupled manner.

FLUENT has the capability to interact with user written programs, which allows a structural model to be coupled with it. FLUENT also has deforming mesh capabilities that can be controlled though a user written subroutine referred to as a user-defined-function (UDF) in order to simulate the flow around a moving structure. In order to deform the CFD mesh using the results of the modal structural solution, UDF code is developed.

For the unsteady flow calculations, pressure-velocity coupling algorithm, PISO is used with the second order upwinding scheme for density, momentum and energy equations. MSC/NASTRAN finite element program is used to get the modal matrix and the corresponding natural frequencies, which are the main inputs of the coupling scheme.

FSI represents the condition where the magnitudes of the oscillations neither decrease nor increase, and is given by Equation 3.1:

$$V_f = \left( \frac{U_\infty}{b.\omega_\alpha.\sqrt{\upsilon}} \right) \tag{3.1}$$

where b is half chord length at wing root, $\omega_\alpha$ is the first torsion frequency and $\upsilon$ is mass ratio described as Equation 3.2.

$$\upsilon = \left( \frac{\rho_{wing}.V_{wing}}{\rho_{air}.V_{cone}} \right) \tag{3.2}$$

where $V_{wing}$=0.0043584 $m^3$ and $V_{cone}$=0.13054 $m^3$, which is the volume of truncated right cone enclosing wing.

From the measured $\rho_\infty$ and $V_\infty$ values from experiment [1], taking gas constant of R = 287.05 $Ks^2/m^2$ and specific heat constant of $\gamma$ = 1.4 from gas dynamics and ideal gas assumption, one may obtain temperature value of $T_\infty$ and $P_\infty$. Experimental flutter data is shown in Table 3.8 for the AGARD Wing 445.6 at several points between Mach 0.499 and Mach 1.141.

Table 3.8 Experimental Flutter Data for Weakened AGARD Wing 445.6

| Mach | $\rho_f$ [kg/m$^3$] | $V_f$ [m/s] | FSI | $\omega / \omega_\alpha$ |
|---|---|---|---|---|
| 0.499 | 0.42770 | 172.5 | 0.4459 | 0.5353 |
| 0.678 | 0.20818 | 231.4 | 0.4174 | 0.4722 |
| 0.960 | 0.06338 | 309.0 | 0.3076 | 0.3648 |
| 1.072 | 0.05512 | 344.7 | 0.3201 | 0.3617 |
| 1.141 | 0.07883 | 364.3 | 0.4031 | 0.4593 |

In the developed coupling scheme, the dynamic aeroelastic simulation is started by computing an initial, steady-state solution for the undeformed wing which is used as the starting point of the unsteady dynamic aeroelastic computations. At the start of the unsteady run, the pressure forces which are calculated at the wall-face centroids are splined to the structural grid nodes using infinite spline method. Pressures that are calculated at cell centers using FLUENT, are used with the cell wall-face area vectors in order to calculate the pressure forces. Since the forces are at the cell centroids and not at the aerodynamic grid points, a spline matrix [$S_1$] is created to spline forces between the wall-face centroids on the aerodynamic grid and the structural grid points using the transpose of the created spline matrix.

New deformed structural grid coordinates are then calculated in modal coordinates using the linear modal structural model which is time marched using the Newmark method. In order to obtain the new coordinates of the aerodynamic grid, structural displacements are transformed to the physical coordinates and splined using a second spline matrix [$S_2$] between the structural grid points and the aerodynamic grid points. Then computational fluid dynamic mesh is deformed by using FLUENT moving mesh algorithm. FLUENT mesh deforming parameters used in dynamic analysis are given in Table 3.7. Finally, new flow variables are calculated for the next time-step. This process is repeated until a specified flow time is reached.

In the dynamic analyses, fine CFD grid and medium CSD grid, which are discussed in grid sensitivity analyses, are chosen. Then, flutter point is calculated using the aeroelastic model. At a selected dynamic pressure, the solution is computed for four cycles of response. If the oscillations in the cycles are growing, a lower dynamic pressure is chosen and the solution is recomputed. If the oscillations are convergent, a higher dynamic pressure is chosen. This procedure is continued until the oscillations are neither decaying nor growing. Then, a dynamic pressure is determined which leads to neutral oscillations. This point of neutral oscillations is defined as the flutter point.

It may be possible to estimate the damping ratio, ζ, which yields positive value for a stable solution, and negative value for an unstable solution from a single response. For the dynamic aeroelastic calculations performed in this study, the structural damping was set to be zero, so calculated damping ratio is purely of aerodynamic origin. For a free-decaying, damped oscillation, the aerodynamic damping can be derived from the logarithmic decrement which is shown in Equations 3.3 and 3.4.

$$\delta_n = \frac{1}{n}\ln\left(\frac{x_i}{x_{i+1}}\right) \tag{3.3}$$

$$\frac{2\pi\xi}{\sqrt{1-\xi^2}} = \frac{1}{n}\ln\left(\frac{x_i}{x_{i+1}}\right) \tag{3.4}$$

where $x_i$ and $x_{i+n}$ are the peak amplitudes at a certain instant of time and taken after $n$ cycles of vibration, respectively.

Damping values are estimated for large set of test points at constant Mach numbers for varying dynamic pressure values. The flutter boundary can then be determined using linear interpolation in order to determine the dynamic pressure which yields zero damping ratio. Accuracy of this method is dependent of the test points near to ζ=0, thus flutter boundary estimation is improved by refining the study with more test points.

In order to determine the optimum time interval size, it is reduced until the aeroelastic simulation does not change by further decrease in the interval size. To achieve this, four different time interval sizes are examined. As can be seen in Figure 3.36, solution is affected by decreasing the time interval size up to the value of 0.001. Further decrease in time interval size does not change the solution significantly. In this test case, wing motion is mostly dominated by the first bending and first torsion modes, which have natural frequencies of 9.6 Hz and 38.10 Hz, respectively [1]. Total time of a single period for these modes shall be 0.104 s and 0.025 s. These frequencies may change due to the unsteady aerodynamic forces. As a first estimate, choosing a time interval size of $\Delta t = 0.001$ will resolve these modes at 104 and 25 time steps, respectively. Time increment in the present study is same on both aerodynamic and structural analyses.

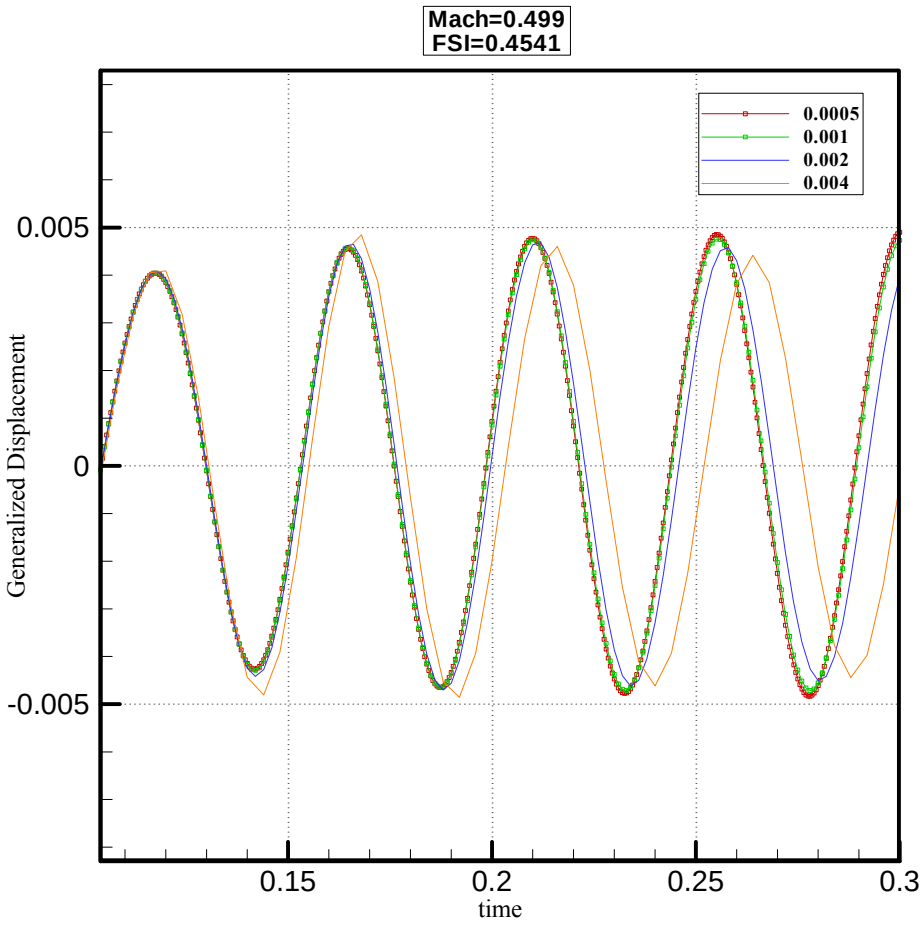


Figure 3.36 Time History of the first Four Generalized Coordinates (M=0.499, FSI=0.4527)

Since the AGARD Wing 445.6 has a symmetric NACA 65A004 airfoil, and the angle of attack is zero degree, an initial perturbation must be given in order to start the oscillations. One can use an initial force applied at some area of the wing, or can use an initial condition in the form of a velocity distribution. In the present study, the first mode shape of the structural model is used to create a sinusoidal velocity variation for one cycle with amplitude of 0.5 m/s for the first mode frequency of the wing. Afterwards, unsteady coupled calculations are continued by removing the excitation and the wing is allowed to respond to the unsteady aeroelastic loads.

The time histories of the first four generalized coordinates at FSI=0.4527, 0.4541, and 0.4557, M=0.499 are shown in Figures 3.37-3.39. The amplitude of the motion reduces at FSI=0.4527, when the flutter speed index is less than the flutter critical speed. The amplitude of the motion is constant at FSI=0.4541, when the flutter speed index is equal to the flutter critical speed. The amplitude of the motion is growing at FSI=0.4557. It can be concluded that at M=0.499, the AGARD wing 445.6 has flutter conditions with FSI=0.4541.

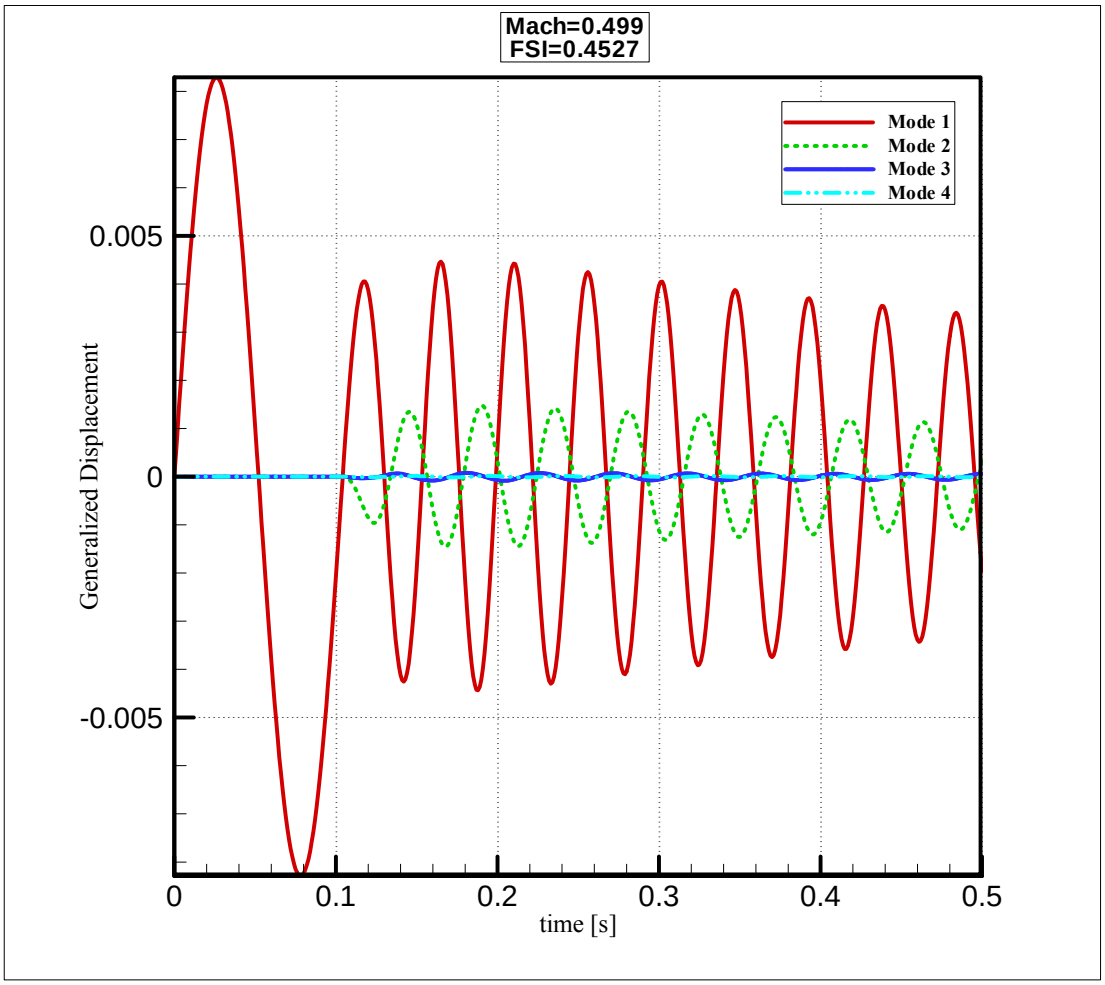


Figure 3.37 Time History of the first Four Generalized Coordinates (M=0.499, FSI=0.4527)

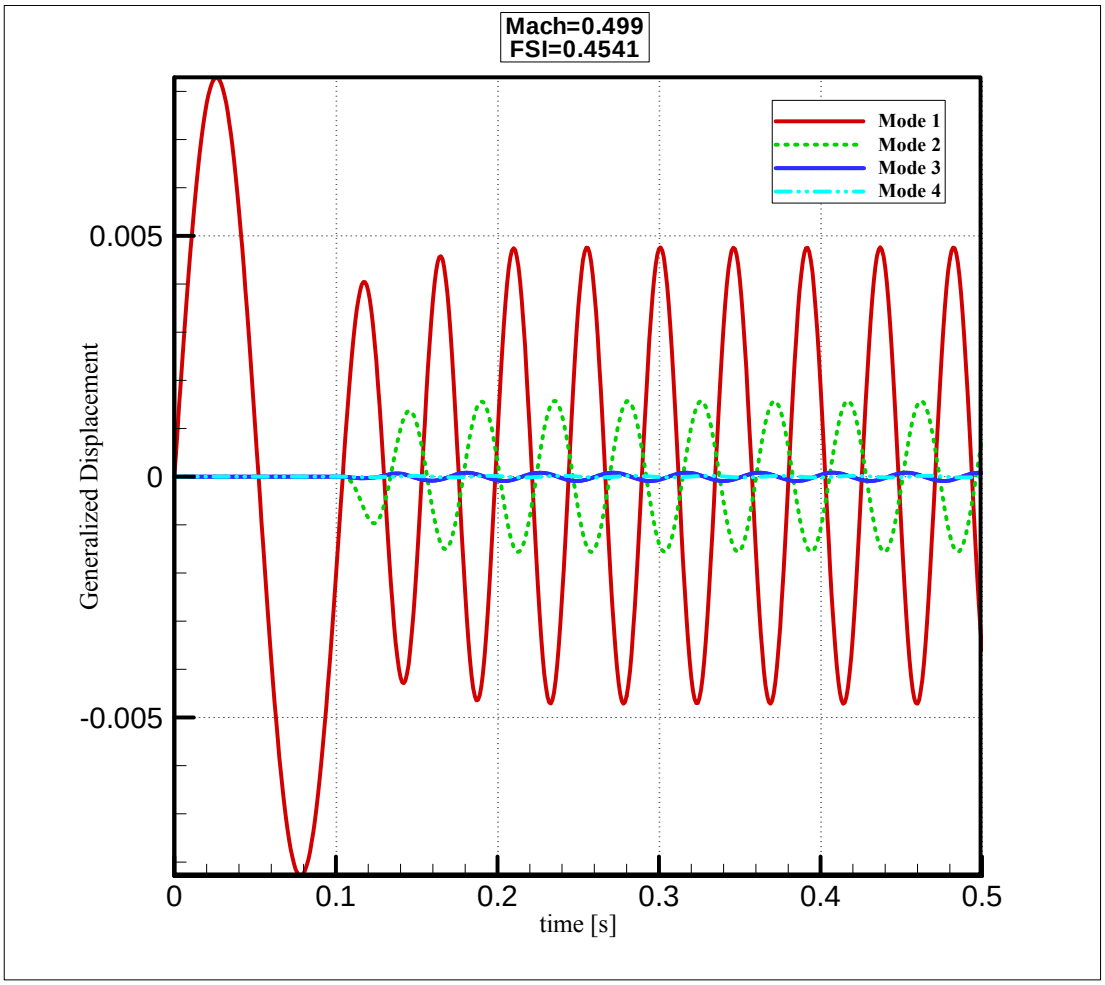


Figure 3.38 Time History of the first Four Generalized Coordinates (M=0.499, FSI=0.4541)

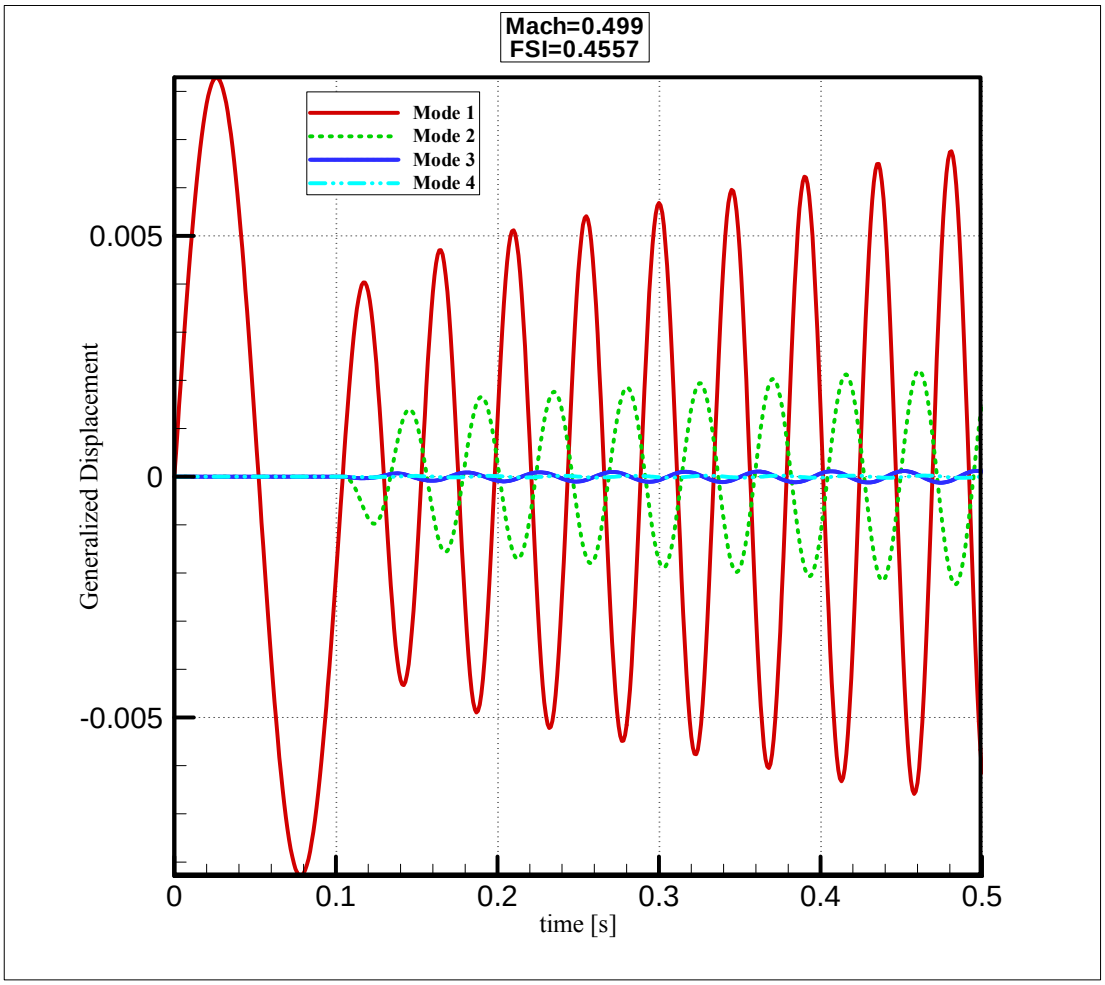


Figure 3.39 Time History of the first Four Generalized Coordinates (M=0.499, FSI=0.4557)

In order to determine the flutter boundary, damping estimations are collected for large set of test points at M=0.499 for varying dynamic pressure values. For these test points, estimated damping coefficients and time histories of the first four generalized coordinates are given in Figure 3.40. Critical flutter speed can be determined from the flight conditions at where damping coefficient is zero. At this Mach number, static pressure is 36230.5 Pa, and the corresponding flutter speed is calculated as 171.84 m/s, which is very close to the experimental value of 172.46 m/s.

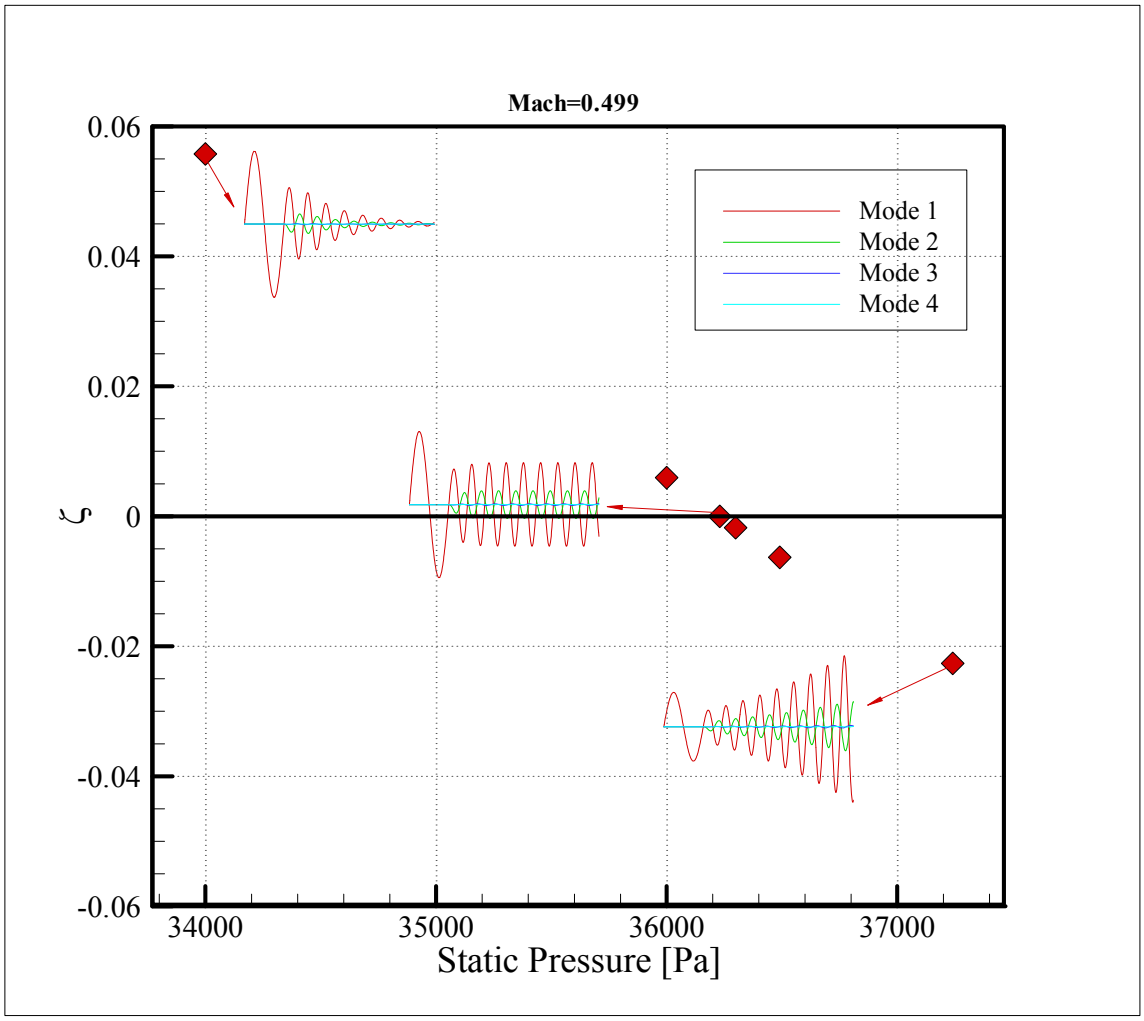


Figure 3.40 Flutter Boundary Test Points Estimated Damping Coefficients and Generalized Displacements (M=0.499)

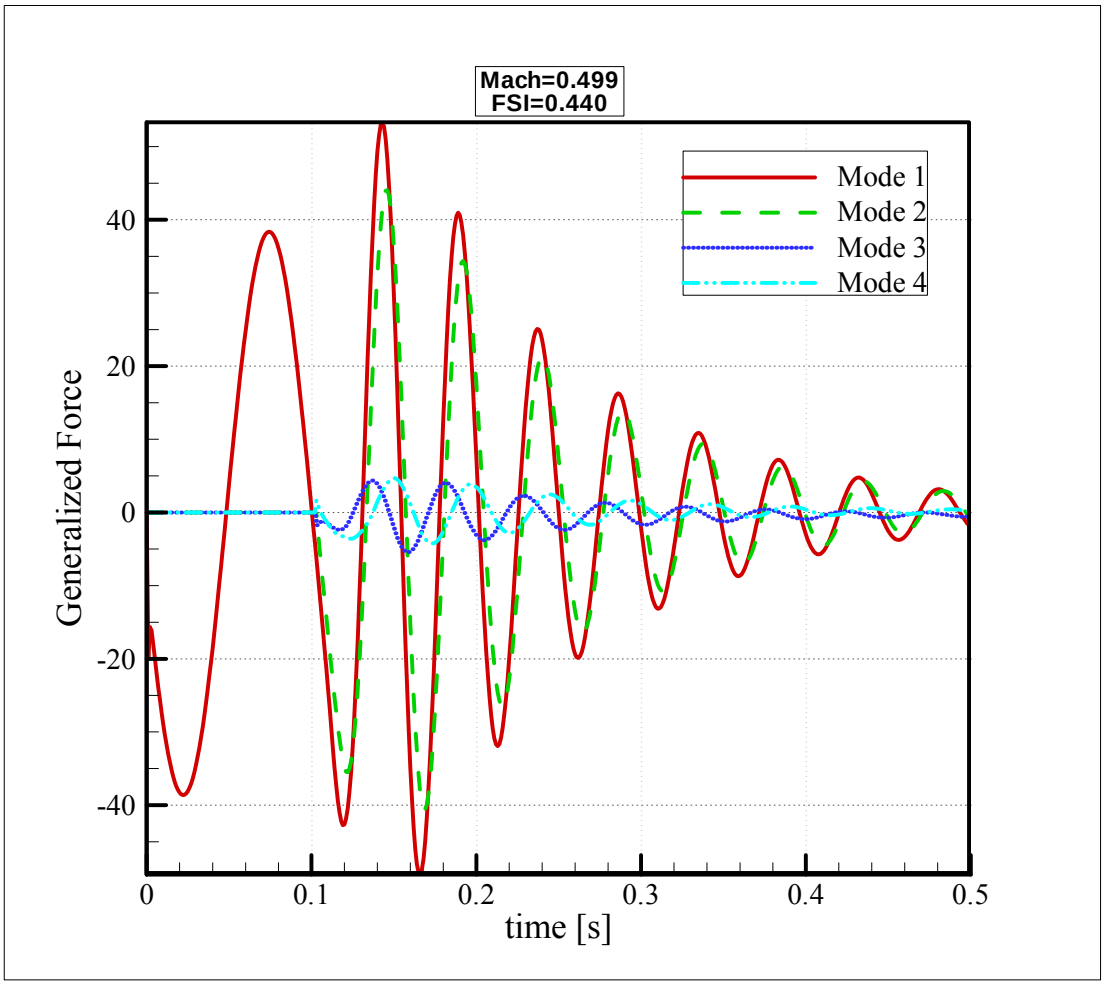


Figure 3.41 Time History of the first Four Generalized Forces (M=0.499, FSI=0.440)

Time history of the generalized forces for the first four modes at FSI=0.440, M=0.499 are shown in Figure 3.41.

Work is calculated by taking the dot product of the displacement and force of each node. Then, results are summed to calculate a total work. Work is compared at each time step for both aerodynamic and structural grids in Figure 3.42. It can be concluded that work done on each system is almost equal at any instantaneous time step. The difference between the total works calculated on the each grid varied from 1E-7 to 5E-6 N.m.

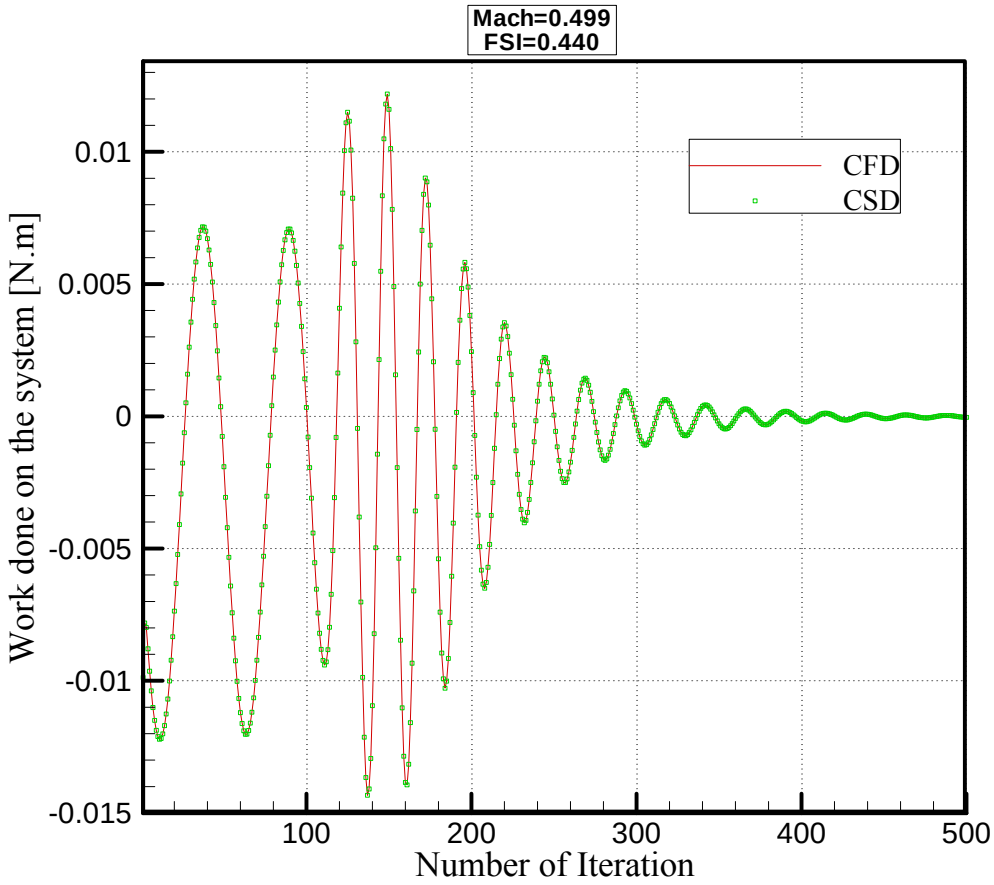


Figure 3.42 Time History of Work Done on Each System (M=0.499, FSI=0.440)

The time histories of the first four generalized coordinates at FSI=0.4205, 0.426, and 0.4337, M=0.678 are shown in Figures 3.43-3.45. It can be concluded that at M=0.678, the AGARD Wing 445.6 has flutter conditions with FSI=0.426. Test points and corresponding estimated damping coefficients are given in Figure 3.46. Flutter speed is calculated as 231.08 m/s, which is very close to the experimental value of 231.37 m/s. Similarly, flutter speed indexes, which lead to neutral oscillations, are determined for Mach numbers 0.960, 1.072 and 1.141. Figures 3.47-3.58 show the test points and estimated damping coefficients.

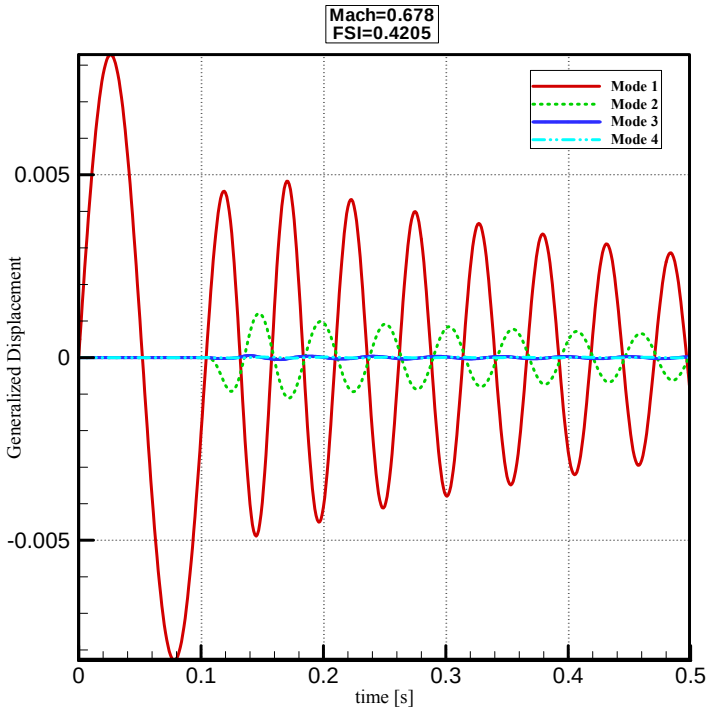


Figure 3.43 Time History of the first Four Generalized Coordinates (M=0.678, FSI=0.4205)

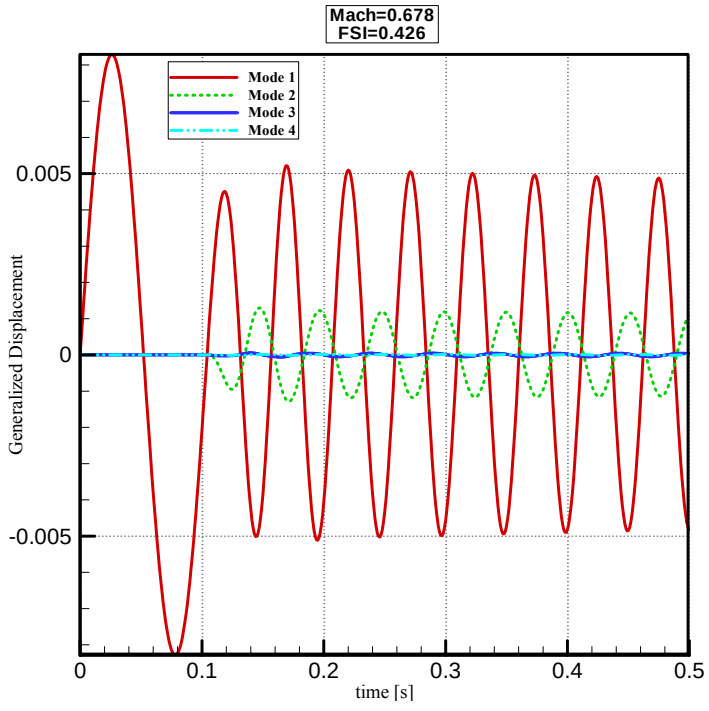


Figure 3.44 Time History of the first Four Generalized Coordinates (M=0.678, FSI=0.426)

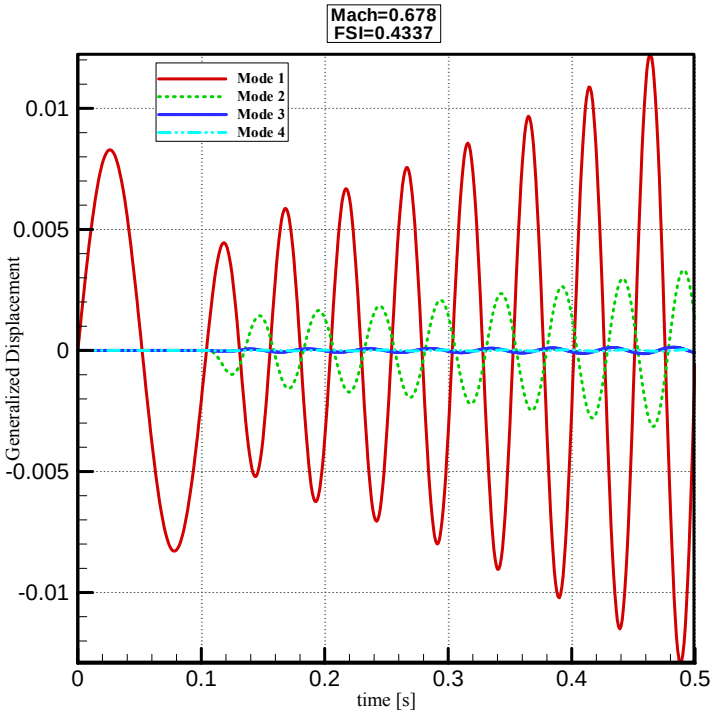


Figure 3.45 Time History of the first Four Generalized Coordinates ( M=0.678, FSI=0.4337)

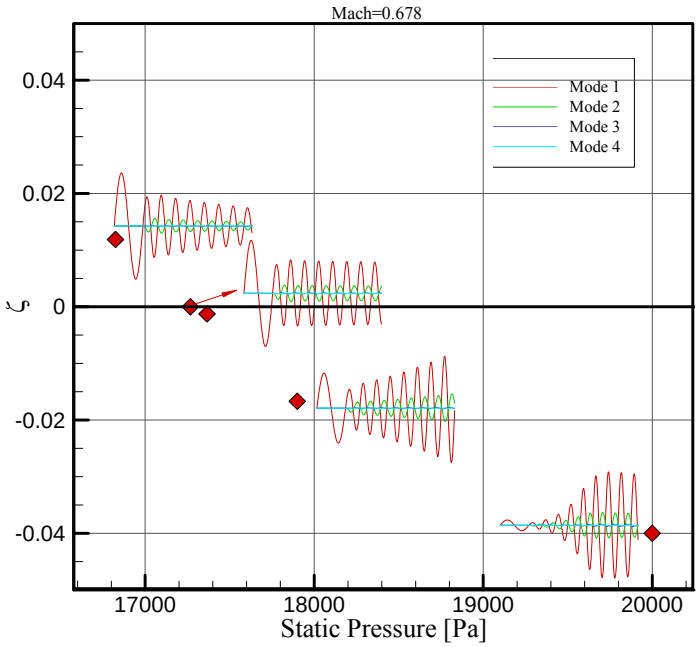


Figure 3.46 Flutter Boundary Test Points Estimated Damping Coefficients and Generalized Displacements (M=0.678)

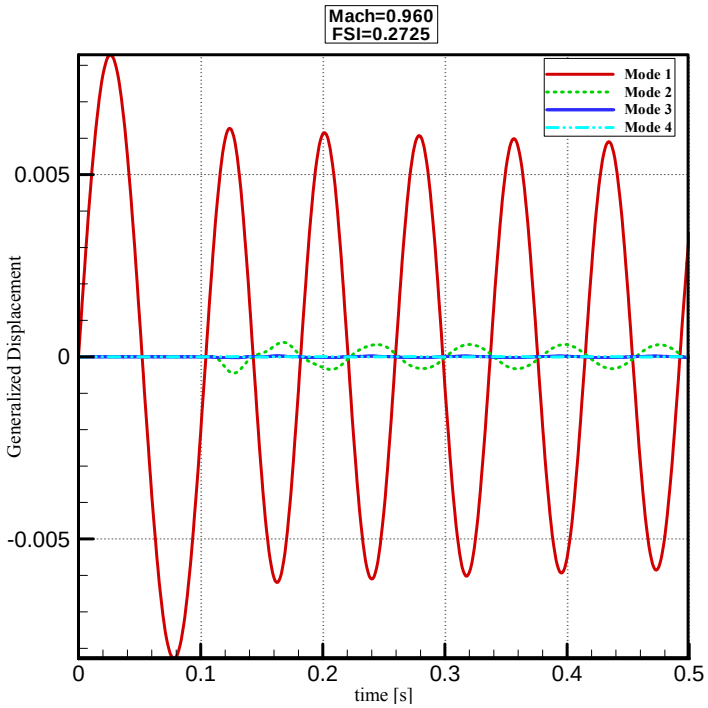


Figure 3.47 Time History of the first Four Generalized Coordinates (M=0.960, FSI=0.2725)

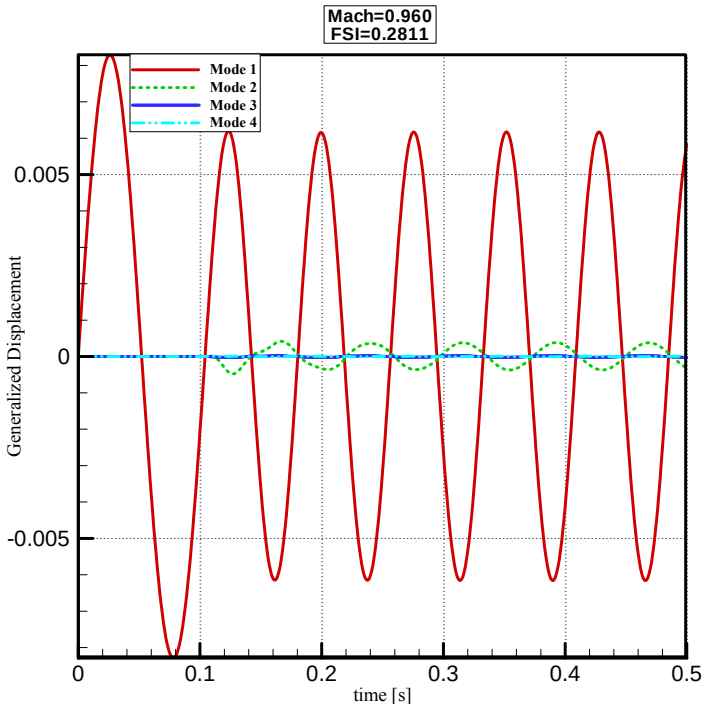


Figure 3.48 Time History of the first Four Generalized Coordinates (M=0.960, FSI=0.2811)

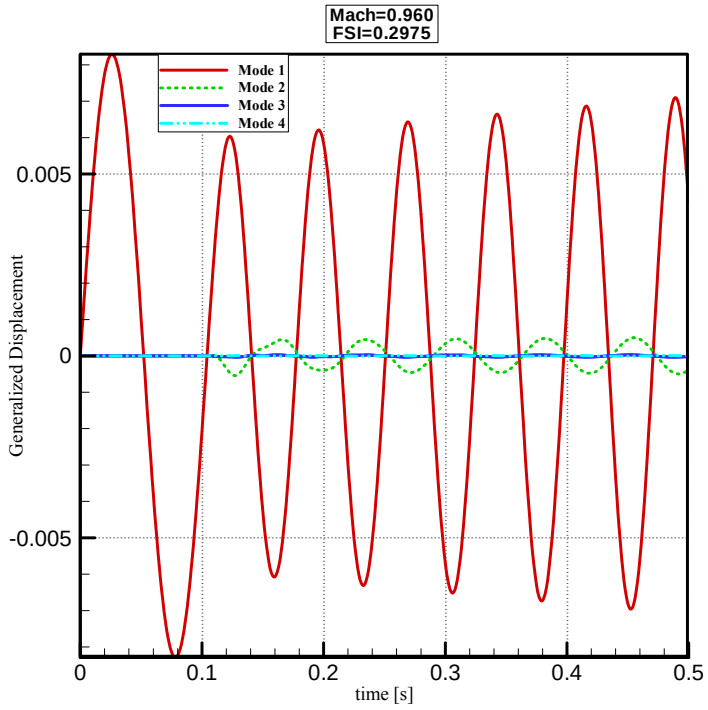


Figure 3.49 Time History of the first Four Generalized Coordinates (M=0.960, FSI=0.2975)

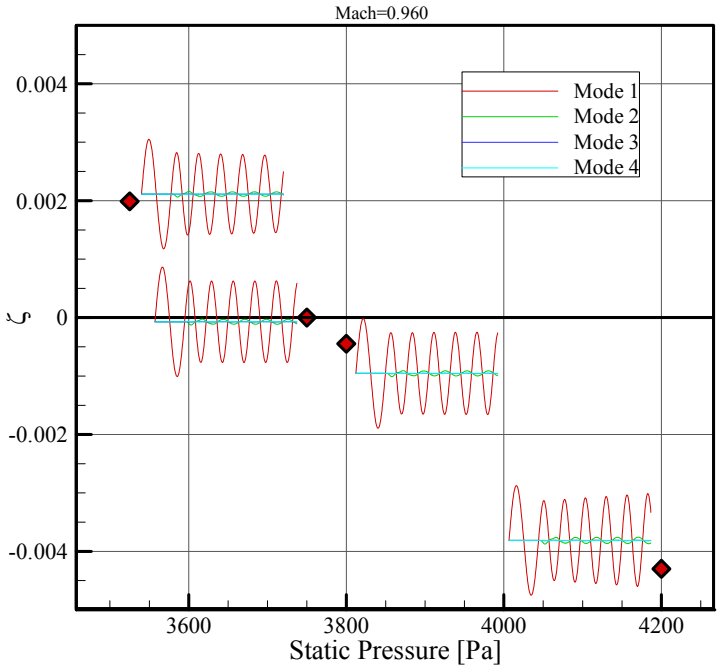


Figure 3.50 Flutter Boundary Test Points Estimated Damping Coefficients and Generalized Displacements (M=0.960)

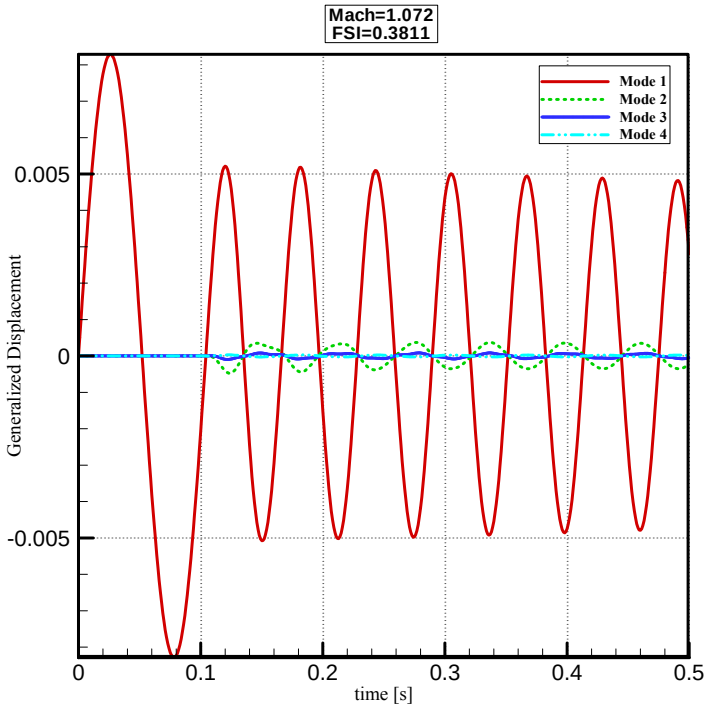


Figure 3.51 Time History of the first Four Generalized Coordinates (M=1.072, FSI=0.3811)

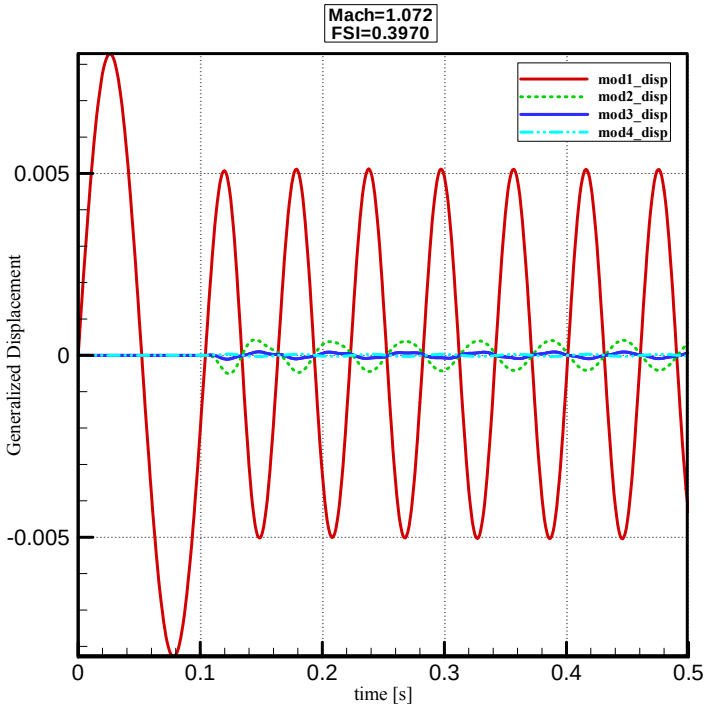


Figure 3.52 Time History of the first Four Generalized Coordinates (M=1.072, FSI=0.3970)

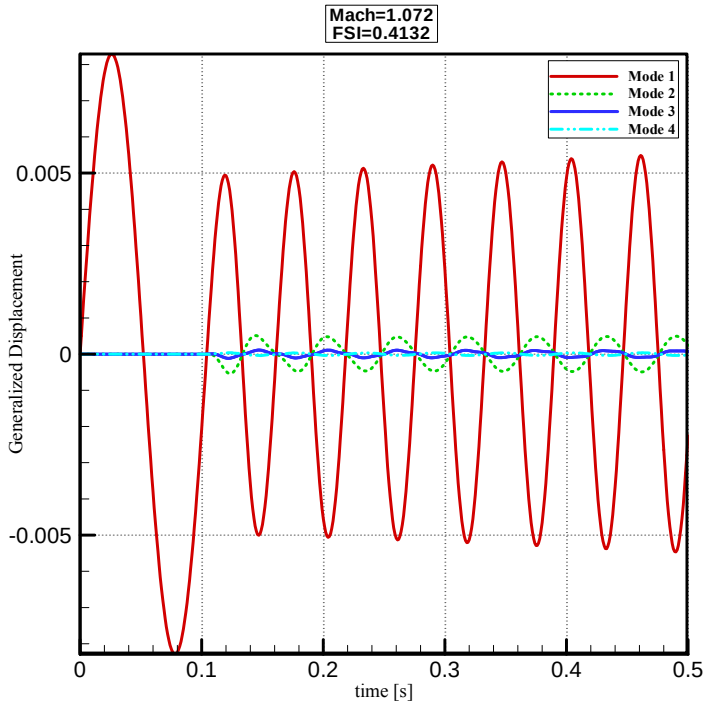


Figure 3.53 Time History of the first Four Generalized Coordinates (M=1.072, FSI=0.4132)

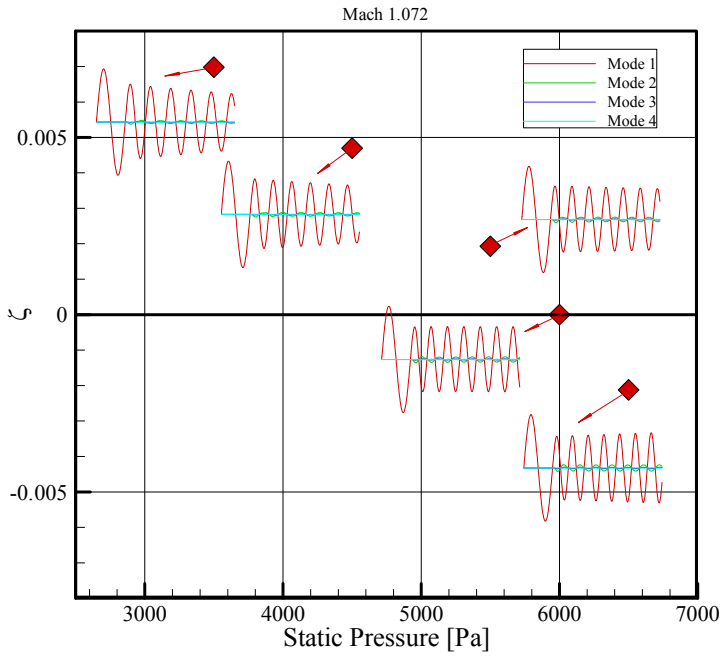


Figure 3.54 Flutter Boundary Test Points Estimated Damping Coefficients and Generalized Displacements (M=1.072)

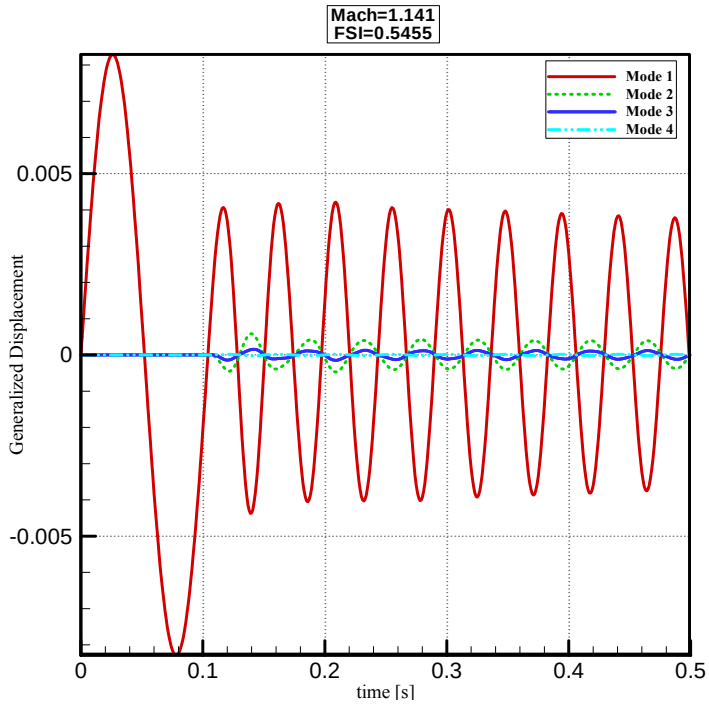


Figure 3.55 Time History of the first Four Generalized Coordinates (M=1.141, FSI=0.5455)

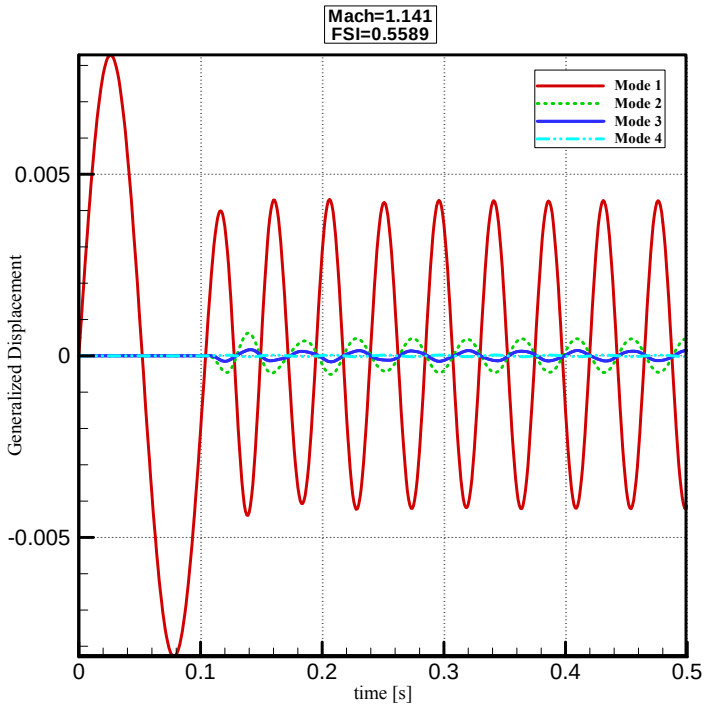


Figure 3.56 Time History of the first Four Generalized Coordinates (M=1.141, FSI=0.5589)

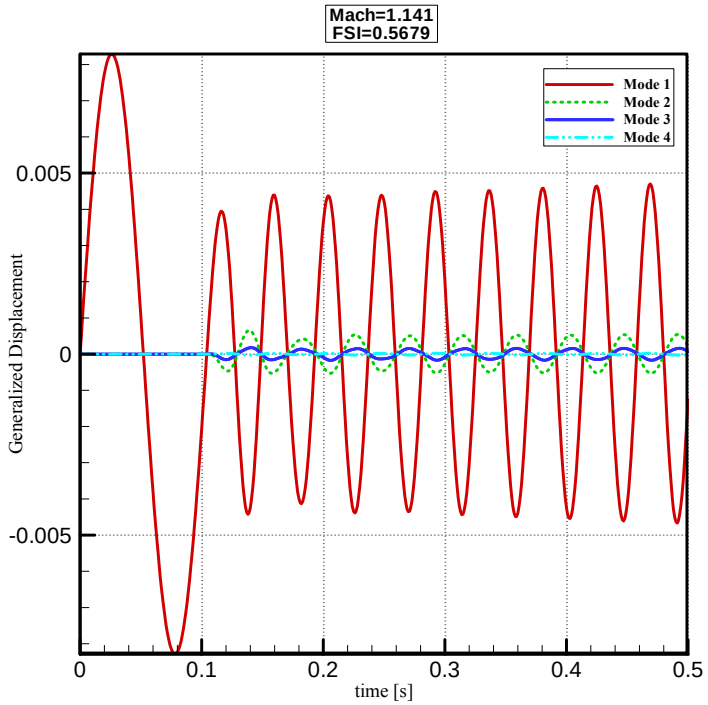


Figure 3.57 Time History of the first Four Generalized Coordinates (M=1.141, FSI=0.5679)

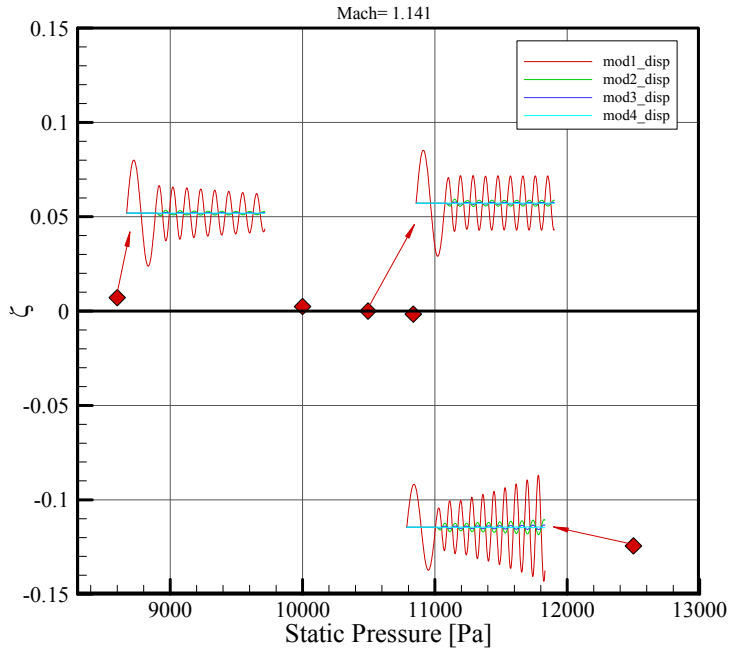


Figure 3.58 Flutter Boundary Test Points Estimated Damping Coefficients and Generalized Displacements (M=1.141)

The results of the flutter analysis of AGARD Wing 445.6 are compared with the experimental data and results of the previous studies in Figures 3.59-3.60 and 3.61 respectively. It can be concluded that the results of the flutter boundary and flutter frequency of AGARD Wing 445.6 for Mach numbers ranging from 0.499 to 1.141 are good agreement with the experimental results except the region of transonic dip where lower flutter speed is predicted. This can be attributed to the inviscid flow assumption. Including the viscous effects may improve the prediction of FSI at this regime.

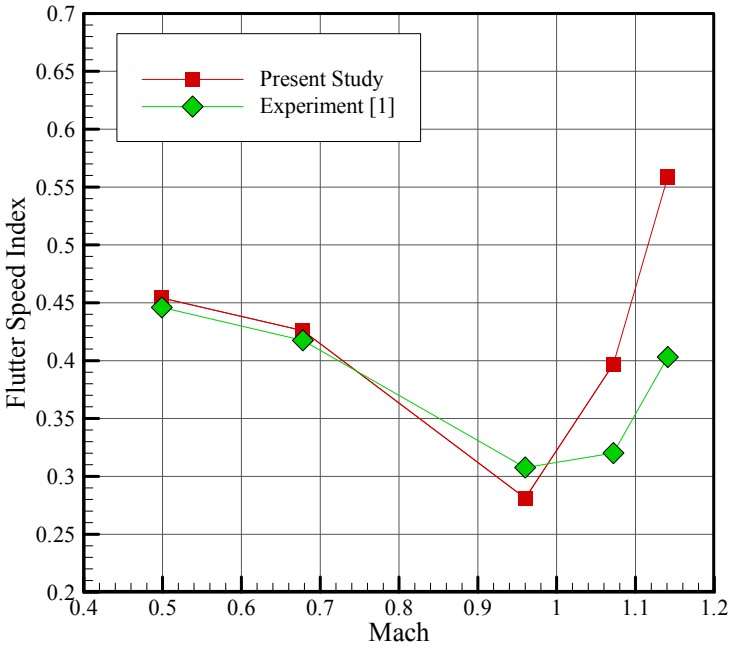


Figure 3.59 Comparison of Computed Flutter Speed Index Values and Experimental Data of AGARD Wing 445.6

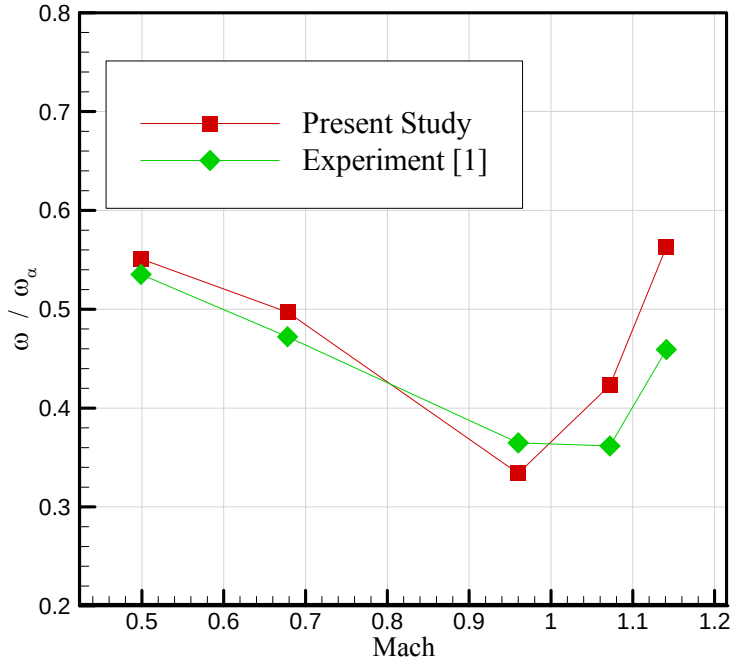


Figure 3.60 Comparison of Computed Flutter Frequency Ratio with Experimental Data of AGARD Wing 445.6

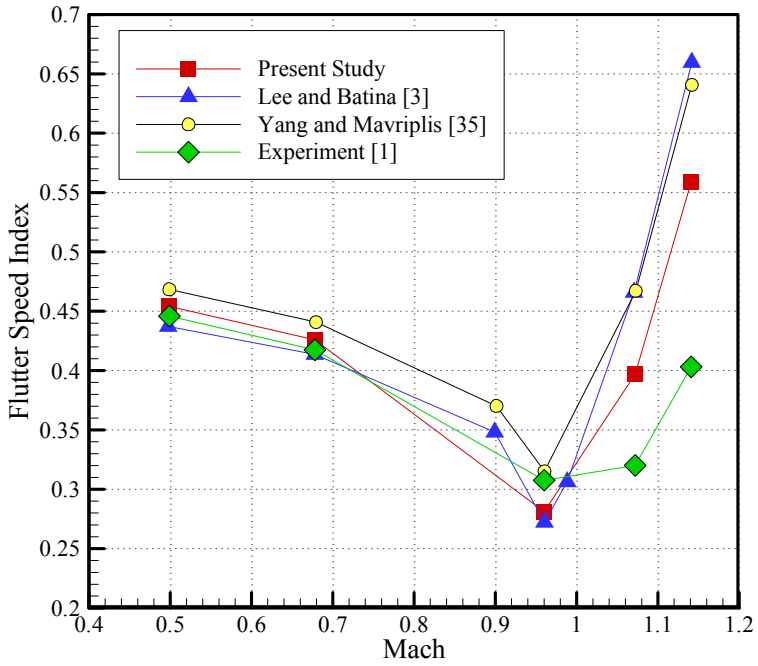


Figure 3.61 Comparison of Computed Flutter Speed Index Values, Numerical Data, and Experimental Data of AGARD Wing 445.6

Deflected wing positions at some time instances during the aeroelastic simulation are shown in Figure 3.62.

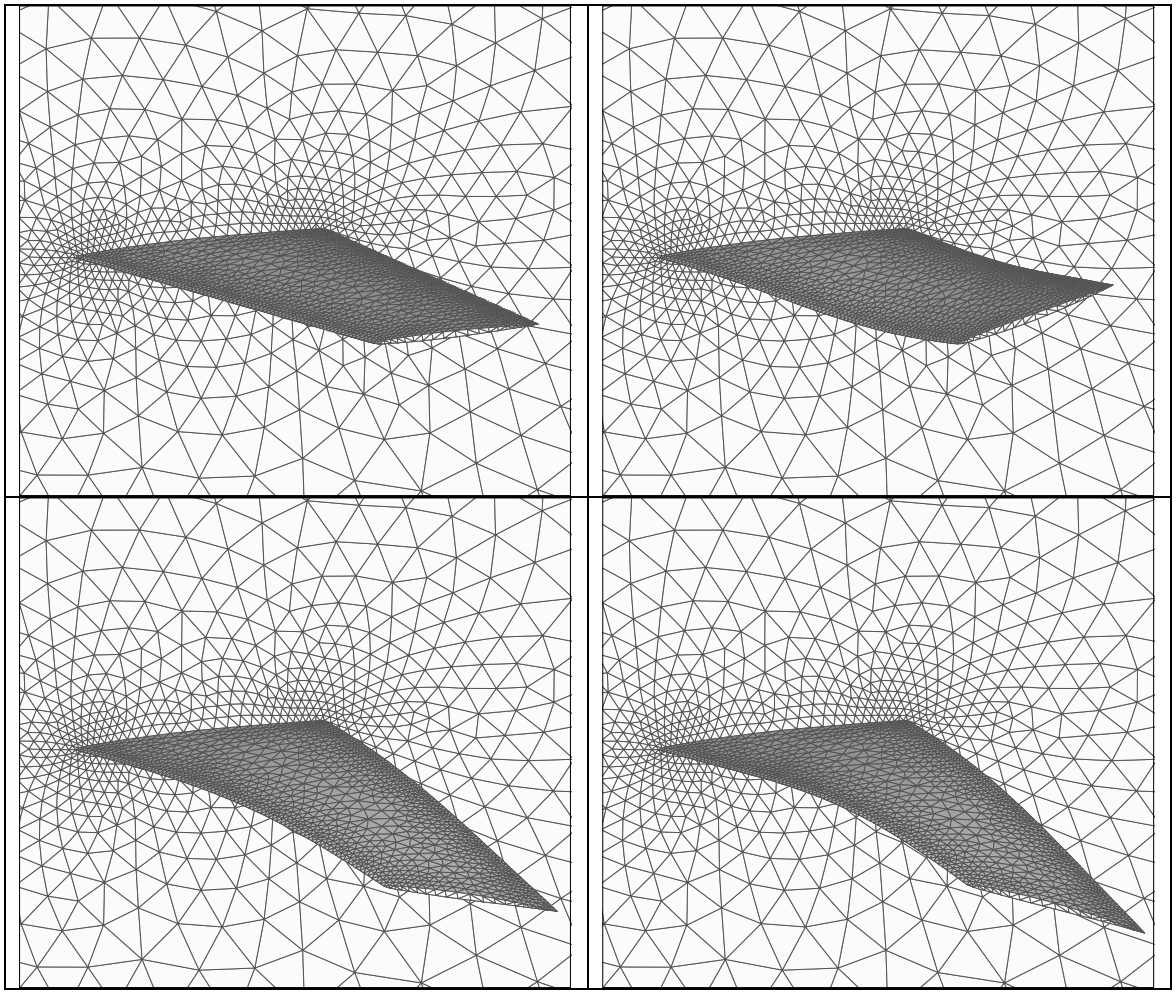

Figure 3.62 Deflected Wing Positions at Different Time Instances

## *3.2 TEST CASE 2 - GENERIC SLENDER MISSILE*

### *3.2.1 INTRODUCTION*

Missile body is a slender, elastic structure. Thus, aerodynamic and dynamic forces acting on the missile at high speeds lead to deformation of the body. The elastic deformation on the missile body also results in a variation of the aerodynamic loads. This affects the missile aerodynamic performance in terms of stability and control effectiveness. The objective of the present work is to determine static aeroelastic properties for a canard controlled supersonic slender missile shown in Figure 3.63. The missile has blunted ogive nose with fineness ratio 1. Total length of the missile is 28 calibers. Control surfaces are deflected as 10° in both pitch and yaw plane to determine aeroelastic characteristics of the missile at drastic flight conditions during maneuver of the missile at Mach number 1.85.

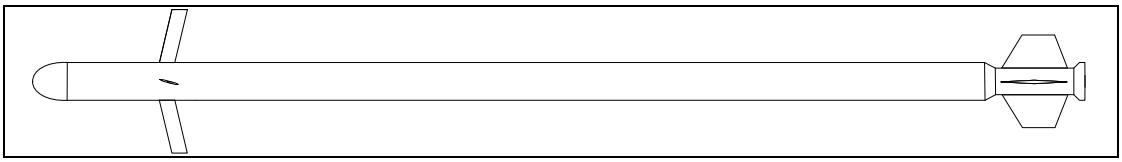

Figure 3.63 Generic Canard Controlled Slender Missile

Material of the missile body is chosen as aluminum whereas canards and tails are modeled as steel. Mechanical properties are shown in Table 3.9.

Table 3.9 Mechanical Properties for the Generic Canard Controlled Slender Missile

| | **Missile Body (aluminum)** | **Canards and Tails (steel)** |
|---|---|---|
| **Material Property** | **Value [GPa]** | **Value [GPa]** |
| E | 70 | 200 |
| **Material Property** | **Value [kg/m$^3$]** | **Value [kg/m$^3$]** |
| ρ | 2700 | 7750 |
| **Material Property** | **Value** | **Value** |
| ν | 0.35 | 0.3 |

Where, E is the modulus of elasticity, ν is Poisson's ratio, and ρ is the density of the material.

#### *3.2.1.1 Static Aeroelastic Analysis of the Slender Missile*

In this part, details of static aeroelastic analysis of the slender missile are given. The objective of the static aeroelastic analysis is to determine the aeroelastic effects on stability and control effectiveness of the missile.

Static aeroelastic analyses are initiated by computing an initial steady-state solution. This converged flow solution is used as a starting point for static aeroelastic iterations and aeroelastic iterations continue until the difference of the root mean square values of structural displacements between two consecutive iterations is less than the prescribed tolerance ($10^{-7}$).

The CFD analysis in this study is carried out using density based with second order upwinding discretization flow solver, FLUENT. In the CFD model, missile is meshed using unstructured tetrahedral meshes. The model's grid size is about 2,291,346 cells (Figure 3.67). For structural analysis, MSC/NASTRAN finite element commercial software is used. The model consists of shell (CQUAD4) type of element for the finite element discretization. Wings are attached to the missile body with rigid RBE2 elements. This connection may be modified to search for aeroservoelastic effects in the future. Finite element model of the missile is shown in Figure 3.66. In order to calculate the deformations of the missile in flight, Inertia Relief module of MSC/NASTRAN is used. Support point is chosen as the center of gravity location and relative displacements are calculated with respect to this point.

Linear interpolation using Alternating Digital Tree data structure is performed to transfer displacements and pressure loads between the structural and aerodynamic grid points. An example of building up ADT for the slender missile and application of linear interpolation of pressure distribution from CFD surface mesh to CSD surface mesh are shown in Figures 3.64 and 3.65, respectively. FLUENT moving mesh algorithm is used to deform the CFD grid and FLUENT mesh deforming parameters used in this study are shown in Table 3.7.

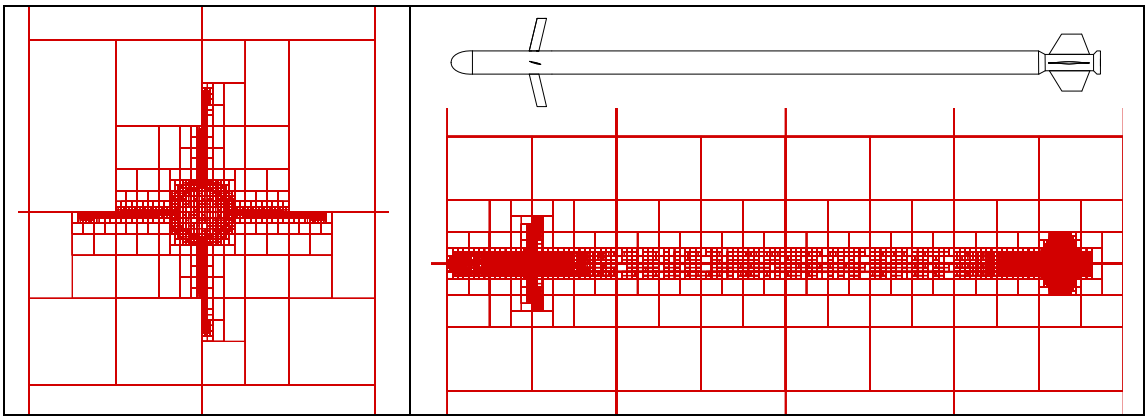

Figure 3.64 ADT Built with the Points of the Grid Boundaries of the Generic Slender Missile

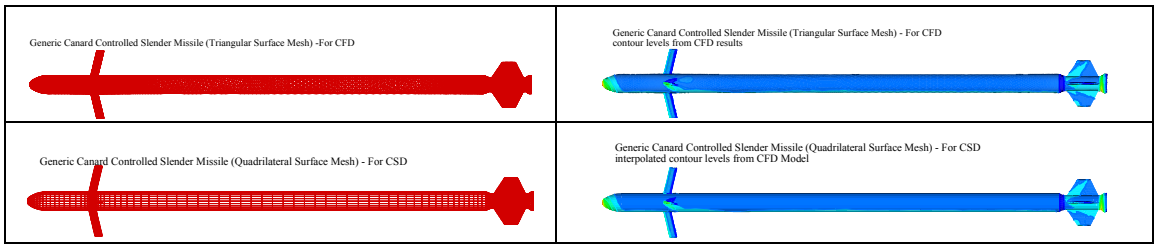


Figure 3.65 Application of AdtSearchIn to Non-matching Discrete Interfaces between Fluid and Structure Mesh of the Generic Slender Missile

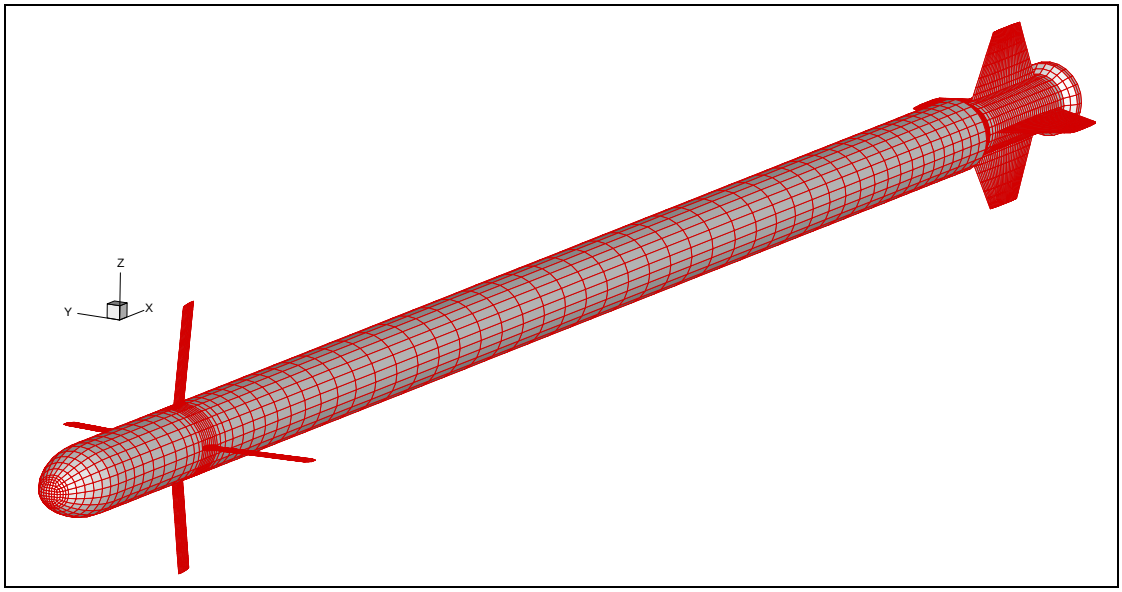


Figure 3.66 Finite Element Model of the Missile for Structural Analysis

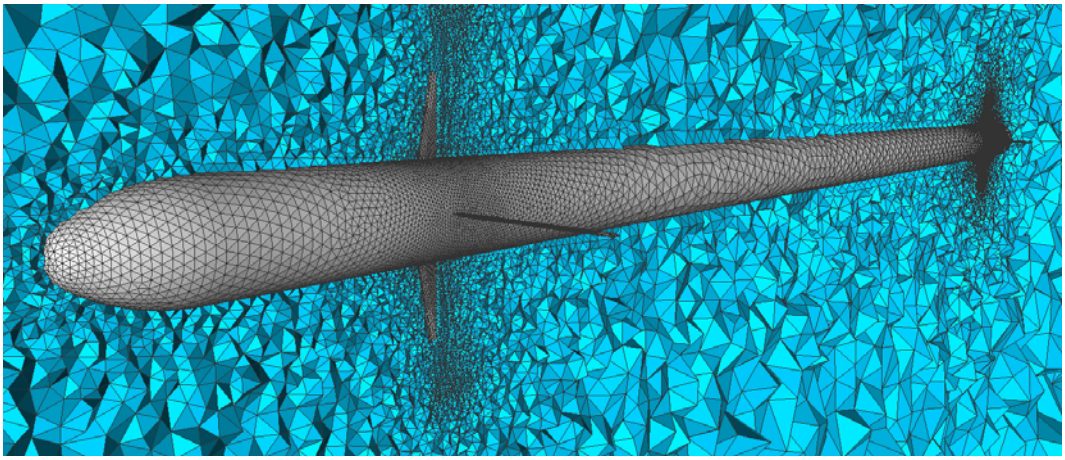

Figure 3.67 Unstructured CFD Grid for the Canard Controlled Generic Slender Missile

The root mean square of the z-direction displacement is shown in Figure 3.68. Each iteration step continues until constant lift and drag coefficient values are obtained and CFD grid point locations are updated based on the structural finite element analyses.

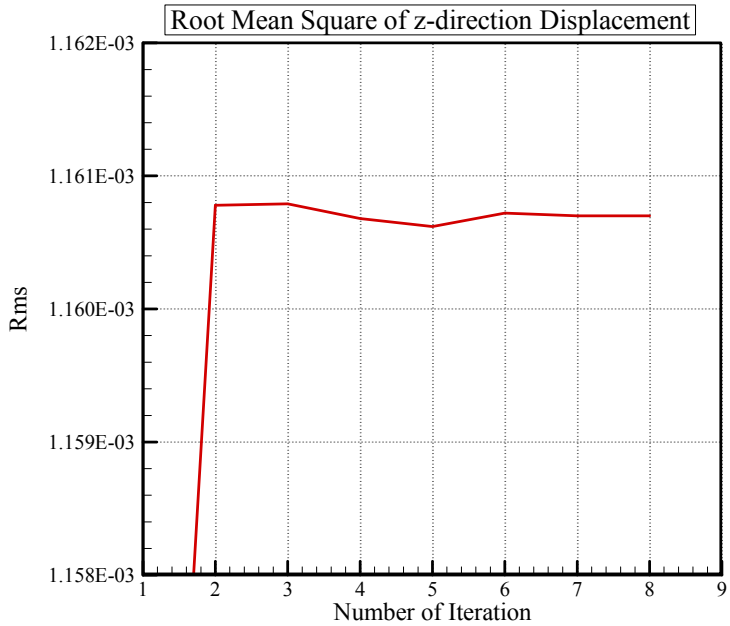


Figure 3.68 The Root Mean Square of z-direction Displacement at Each Aeroelastic Time-step

Equilibrium position for elastic missile is compared with rigid missile is given in Figure 3.69.

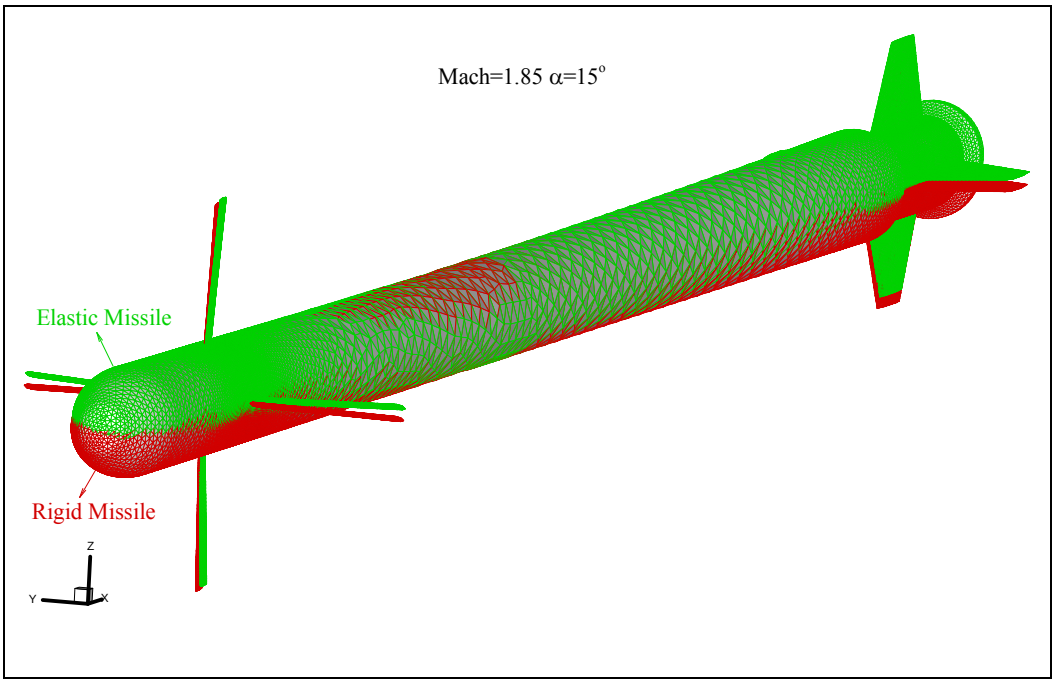


Figure 3.69 Rigid (red) and Elastic (green) Position of Slender Missile

The deformations due to elasticity of the structure have an influence on the aerodynamic loads on the missile. In Figures 3.70 and 3.71, normal force and pitching moment coefficients are given for elastic and rigid missiles. As can be seen, at 10° angle of attack, the normal force coefficient of the elastic missile is reduced by 2 %. As body bends about the center of gravity, the equivalent angle of attack of the canards increases and that of tails decreases. On the other hand, the pitching moment coefficient about the missile nose tip changes about 6 % as compared to the rigid missile.

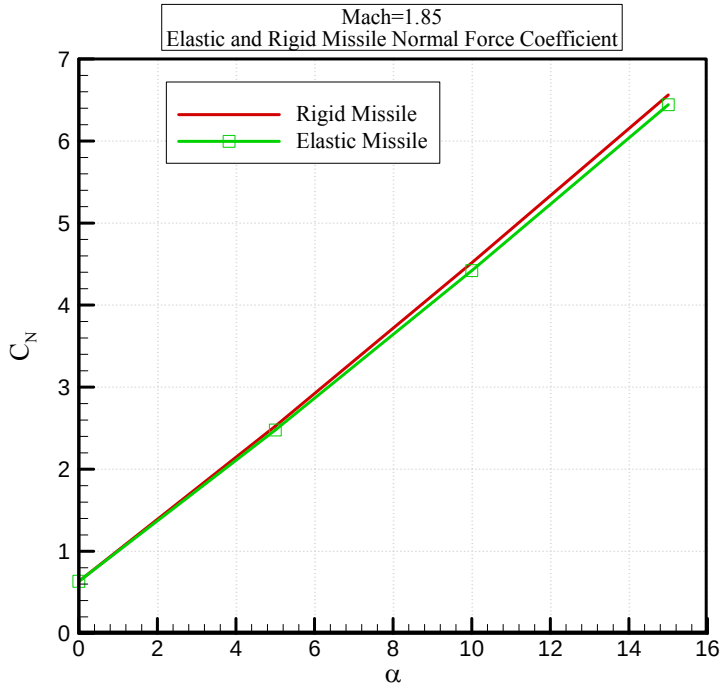


Figure 3.70 Elastic and Rigid Missile Normal Force Coefficient

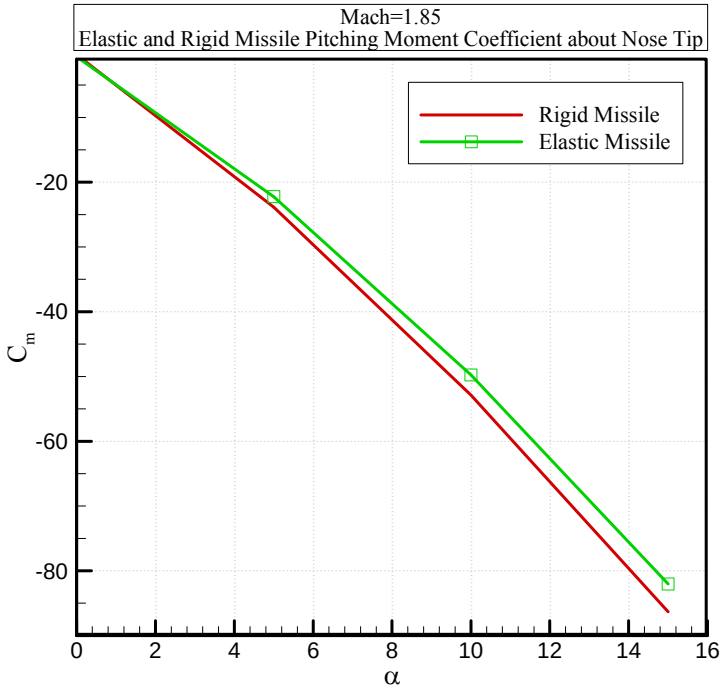


Figure 3.71 Elastic and Rigid Missile Pitching Moment Coefficient about the Nose Tip

The center of pressure of the missile changes by amount of 0.45 caliber of the missile at 10° angle of attack. Since stability of the missile changes, control effectiveness of the missile also changes by amount of 15 % as can be seen from Figure 3.72. For the rigid case, 10° elevator deflection angle gets the missile in trim condition at 12.1° angle of attack, whereas it gets the missile in trim condition at 14.2° angle of attack for the elastic case.

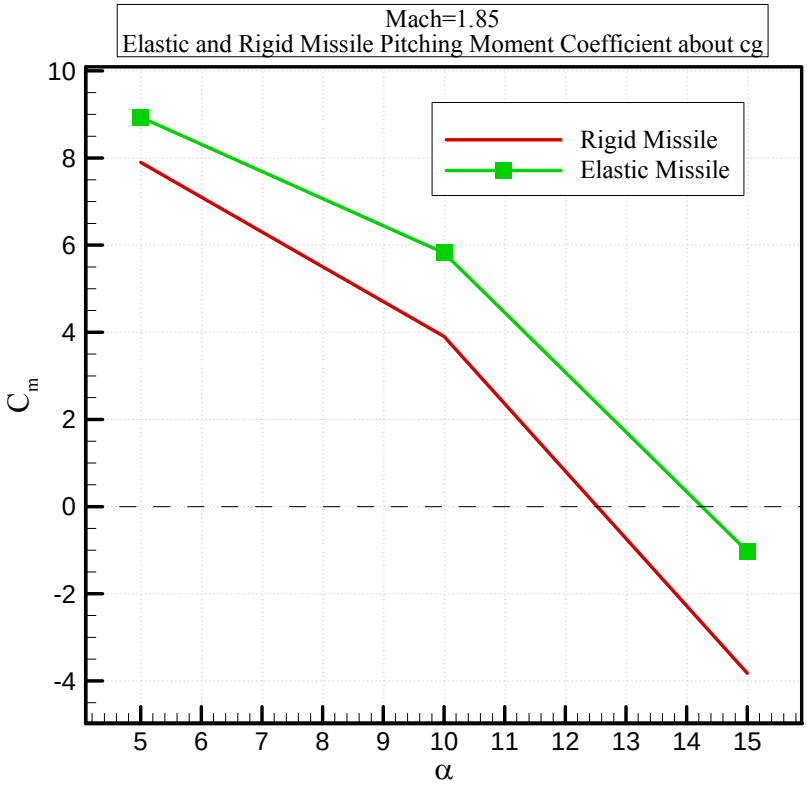


Figure 3.72 Elastic and Rigid Missile Pitching Moment Coefficient about cg

# CHAPTER 4

# CONCLUSIONS AND RECOMMENDATIONS

In this thesis, a closely coupled approach is developed in order to solve the static and dynamic aeroelastic problems. Since this approach gives the variability in choosing different solvers depending on the complexity of the applications, it is an efficient way to couple CFD and CSD solvers.

To conduct static aeroelastic analysis, three dimensional, inviscid CFD solver, FLUENT is coupled with finite element structural solver, MSC/NASTRAN, that is used to solve the displacements associated with the aerodynamic pressure loading. Likewise for dynamic aeroelastic analysis, a numerical method is developed to predict the aeroelastic response and flutter boundary. Modal approach is used for structural response and Newmark algorithm is used for time-marching. Mode shapes and corresponding natural frequencies are obtained by using MSC/NASTRAN and used as input for this approach. Unsteady flow field is solved using commercial CFD solver, FLUENT, in a parallel computing environment.

Mesh deformation techniques, which have been investigated as a part of this research, are presented. In this study, details of mesh deformation methods based on FLUENT mesh deformation algorithm and linear elastic finite element based deformation method are given. It can be concluded that, artificial material stiffness property created in finite element based deformation method with varying elastic properties according to the cell volume can be implemented for mesh deformation problems. But, since cell skewness and cell size parameters cannot be controlled, mesh quality decreases especially for

large boundary deformations during the deformation process. Since FLUENT replaces the collapsed or deteriorated cells with new cells, quality of the mesh can be easily controlled and preserved during the deformation of the aerodynamic grid.

Interference techniques between CFD and CSD grid are also investigated in this study. Predictions of complex dynamic aeroelastic phenomena such as flutter are sensitive to the energy conservation at the fluid-structure interface. An imbalance in energy transfer between the CFD and the CSD systems cause instabilities and incorrect prediction of the aeroelastic behavior. Spline methods conserve the total force and moments on each system and applicable to the dynamic aeroelastic problems. For static aeroelastic problems, linear interpolation method using ADT is applied successfully to transfer displacements and pressure loads between the structural and aerodynamic grid points. ADT reduces the interpolation time by amount of the logarithm of the number of points.

Static and dynamic aeroelastic problems of the AGARD Wing 445.6 are solved with the developed procedure and obtained results are compared with numerical and experimental data available in literature.

For the static aeroelastic analyses, out-of-plane deformations of AGARD Wing 445.6 at leading and trailing edges are compared with the results of Cai [4]. The results of the present study appear to agree well with the results of Cai [4] except for the small differences at the leading and trailing edges of the wing tip. These differences may be attributed to the different flow solvers, meshing technique, and coupling approach. Rigid and elastic wing pressure coefficient distributions calculated in the present study are compared to each other. Cp values on the surface decreases in elastic wing due to decreased pressure values. The lift coefficient of the elastic wing is reduced by 22 % as compared to rigid wing.

For the dynamic aeroelastic analyses, FSI is determined for the AGARD Wing 445.6 at different Mach numbers ranging from 0.499 to 1.141. The flutter points are determined by running a solution for a significantly long period of time to arrive at a neutrally stable

solution. Damping estimations are collected for large set of test points at constant Mach numbers for varying dynamic pressure values. Then, the flutter boundary is determined which yields zero damping ratio, $\zeta=0$, where the amplitude of oscillations of the generalized displacement is neither decaying nor growing. The results of the present study are good agreement with the experimental results except the region of transonic dip. Coupling unsteady Euler equations to the linear modal structural model predicts a lower flutter speed at the transonic dip. Viscous effects are important factors in determining the transonic dip accurately. Thus, including the viscous effects may improve the prediction of FSI at this regime.

As another test case, static aeroelastic problem of the canard controlled slender missile is solved using the developed procedure. For structural analysis, MSC/NASTRAN inertia relief option, which is used to simulate unconstrained structures in flight, is used with linear elastic solver. The displacements of the structure under the aerodynamic loading are calculated with respect to the center of gravity of the missile. The normal force and pitching moment coefficients of the rigid and elastic missile are calculated in the present study and compared to each other. Normal force coefficient does not change significantly. The pitching moment coefficient about the nose tip of the missile changes by amount of 6 %, as center of pressure changes due to bending of the missile. This affects the aerodynamic performance of the missile in terms of stability and control effectiveness. Control effectiveness changes about 15 % as compared to the rigid missile. For the further studies, dynamic aeroelastic characteristics of the slender missile, which is more critical especially in the transonic region of the flight regime, will be investigated.

# REFERENCES

[1] Yates, E. C., "AGARD Standard Aeroelastic Configurations for Dynamic Response I-Wing 445.6", AGARD Report 765, North Atlantic Treaty Organization, Group for Aerospace Research and Development, 1988.

[2] Kolonay, R. M., "Unsteady Aeroelastic Optimization in the Transonic Regime", Ph. D. Thesis, Purdue University, 1996.

[3] Lee-Rausch M .E., Batina T.J., "Calculation of AGARD Wing 445.6 Flutter Using Navier-Stokes Aerodynamics", AIAA 93-3476.

[4] Cai J., Liu F., Tsai H.M., Wong A.S.F., "Static Aero-elastic Computation with a Coupled CFD and CSD Method", AIAA 2001-0717, Aerospace Sciences Meeting and Exhibit, 39th, Reno, NV, Jan. 8-11, 2001.

[5] E.M. Lee-Rausch and J.T. Batina, "Wing Flutter Boundary Prediction using Unsteady Euler Aerodynamic Method", Journal of Aircraft, March-April 1995.

[6] FLUENT 6.3 Documentation. FLUENT, Inc., 2006.

[7] J. T. Batina, "Unsteady Euler Airfoil Solutions using Unstructured Dynamic Meshes", AIAA Journal, 1381-1388, 1990.

[8] C. Farhat, C. Degand, B. Koobus, and M. Lesoinne, "Torsional Springs for Two-dimensional Dynamic Unstructured Fluid Meshes", Computational Methods Application Mechanical Engineering, 163:231-245, 1998.

[9] M. Murayama, K. Nakahashi, and K. Matsushima, “Unstructured Dynamic Mesh for Large Movement and Deformation”, AIAA 2002-0122, 2002.

[10] Robinson, A.B, Batina, T.J., Yang, Y.Y.H., “Aeroelastic Analysis of Wings Using the Euler Equations with a Deforming Mesh”, Journal of Aircraft, Vol.28, No.11, November 1991.

[11] Zhang, S. and Belegundu, A. D., “A Systematic Approach for Generating Velocity Fields in Shape Optimization”, Struct. Opt., Vol. 5, No. 1–2, pp. 84–94, 1993.

[12] Guruswamy, G. P. “A Review of Numerical Fluids/Structures Interface Methods for Computations using High-Fidelity Equations”, Computers and Structures, v. 80, pp. 31-41.

[13] Tezduyar, T. E. and Behr, M., “A New Strategy for Finite-Element Computations Involving Moving Boundaries and Interfaces- the Deforming-Spatial-Domain/Space-Time Procedure”, Comput. Methods Appl. Mech. Engrg.,Vol. 94, pp. 339–351, 1992.

[14] Cavallo, P. A., Hosangadi, A., Lee, T. A., and Dash, S. M., “Dynamic Unstructured Grid Methodology with Application to Aero/Propulsive Flowfields”, AIAA Paper 97-2310, 1997.

[15] Guruswamy G .P., Byun C., “Direct Coupling of Euler Flow Equations with Plate Finite Element Structures”, AIAA J., Vol.33, No.2.

[16] Stein, K., Tezduyar, T., and Benney, R., “Mesh Moving Techniques for Fluid-Structure Interactions with Large Displacements”, Journal of Applied Mechanics, 70:58{63, 2003.

[17] Duchon, J., “Splines Minimizing Rotation-Invariant Semi-Norms in Sobolev Spaces”, Constructive Theory of Functions of Several Variables, edited by W. Schempp and K. Zeller, Springer, Oberwolfach, Germany, 1976, pp. 85-100.

[18] M. J. Smith, Hodges, D. H., and Cesnik, C. E. S., “Evaluation of Computational Algorithms Suitable for Fluid-Structure Interactions”, J. Aircraft, 37(2):282–294, 2000.

[19] Lohner, R., and Yang, C., “Improved ALE Mesh Velocities for Moving Bodies”, Comm. Num. Methods Eng., 12(10):599–608, 1996.

[20] “ZAERO version 8.3 Theoretical Manual”. ZONA Technology, Inc., Scottsdale, AZ, 19 edition, 2008.

[21] Parker, G.H, “Dynamic Aeroelastic Analysis of Wing/Strore Configurations”, Air Force Institute of Technology Air University December 2005.

[22] Harder, R.L. and Desmarais, R.N., “Interpolation Using Surface Splines”, AIAA Journal, Vol. 9, No. 2, 1972, pp. 189-191.

[23] J Bonet and J Peraire. “An Alternating Digital Tree (ADT) Algorithm for 3D Geometric Searching and Intersection Problems”, International Journal for Numerical Methods in Engineering, 31:1–17, 1991.

[24] N.V. Taylor C.B. Allen “Investigation of Structural Modelling Methods for Aeroelastic Calculations” AIAA 2004-5370 22nd Applied Aerodynamics Conference and Exhibit, Rhode Island, 2004.

[25] A., Akgül, “ADTSearchIn: Search and Interpolaton on Triangular & Quadrilateral Elements by Data Structure” Roketsan Missile Inductries Inc., November 2001.

[26] Pahlavanloo P., “Dynamic Aeroelastic Simulation of the AGARD 445.6 Wing using Edge, FOI Defence Research Agency”, April 2007.

[27] Nielsen, E. J., and Anderson, W. K., “Recent Improvements in Aerodynamic Design Optimization on Unstructured Meshes”, AIAA Journal, 40(6):1155-1163-2002.

[28] Mathew F., B., Jeffrey L., P., Methods for Simulation-based Analysis of Fluid-Structure Interaction, Sandia National laboratories, 2005.

[29] Bendiksen, O. O., and Hwang, G., “Nonlinear Flutter Calculations for Transonic Wings”, Proceedings of the International Forum on Aeroelasticity and Structure Dynamics, 1997, Confederal of Europe Aerospace Societies Rome, pp. 105–114.

[30] Alonso, J. J., and Jameson, A., “Fully Implicit Time-marching Aeroelastic Solutions”, AIAA 94-0056, 1994.

[31] Bendiksen O. O., “A New Approach to Computational Aeroelasticity”, AIAA-91-0939, Structural Dynamics and Materials Conference, 32nd, Baltimore, MD, April 8-10, 1991.

[32] Luca C., Giuseppe Q., Gian L. G., Paolo M., “Efficient Application of CFD Aeroelastic Methods using Commercial Software”, Dipartimento di Ingegneria Aerospaziale, Milano, Italy

[33] Schuster M.D., Vadyak, J., Atta E., “Static Aeroelastic Analysis of Fighter Aircraft Using a Three Dimensional Navier-Stokes Algorithm”, AIAA-90-0435, Aerospace Sciences Meeting, 28th, Reno, NV, Jan. 8-11, 1990.

[34] Lee-Rausch, E. M. and Batina, J. T. “Calculation of AGARD Wing 445.6 Flutter using Navier-Stokes Aerodynamics”, AIAA-93-3476, AIAA 11th Applied Aerodynamics Conference Monterey, California, August 1993.

[35] Yang, Z., Mavriplis, D. J., “Higher-order Time Integration Schemes for Aeroelastic Applications on Unstructured Meshes”, American Institute of Aeronautics and Astronautics.

[36] Kamakoti, R., Shyy, W., “Fluid–Structure Interaction for Aeroelastic Applications”, Elsevier Ltd., 2005.

[37] A. S. Baddi, “Parallel Computing of Fluid Structure Interactions Problems”, Indiana University, November 2005.

[38] Lee-Rausch, E. M., Batina, J. T., “Wing Flutter Boundary Prediction Using Unsteady Euler Aerodynamic Method”, Journal of Aircraft, Vol. 32, No. 2, 1995.

[39] R. B. Melville, S. A. Morton, and D. P. Rizzetta, “Implementation of a Fully-Implicit Aeroelastic Navier-Stokes Solver", AIAA Paper-97-2039, 1997.

[40] Doi, H., “Fluid/Structure Coupled Aeroelastic Computations for Transonic Flows in Turbomachinery”, Standford University, August 2002.

[41] Wright, J. R., Cooper, J. E., “Introduction to Aircraft Aeroelasticity and Loads”, John Wiley & Sons Inc., 2007.

[42] Bisplinghoff, R.L., Ashley, H. and Halfman, R.L., "Aeroelasticity," Dover Publications, Inc., 1955.

[43] Schuster DM, Liu DD, Huttsell LJ., "Computational Aeroelasticity: success, progress, challenge", J Aircr 2003; 40(5):843–56.

[44] Lee-Rausch E. M., Batina J. T. "Wing Flutter Boundary Prediction using Unsteady Aerodynamic Method", Journal of Aircraft, 1995, 32(2):416-22.

[45] MSC.NASTRAN Linear Static Analysis User's Guide, 2003.

[46] MSC.NASTRAN Basic Dynamic Analysis User's Guide, 2002.

[47] Taylor N. V., Allen C. B., Gaitonde A. and Jones D. P., "A Structure-Coupled CFD Method for Time-Marching Flutter Analysis" The Aeronautical Journal, August 2004.

[48] Guruswamy G. P., and Byun C., "Fluid-Structural Interactions using Navier-Stokes Flow Equations with Shell Finite Element Structures", AIAA Paper 93-3087, 1993.